MEASURING THE HUBBLE CONSTANT FROM REVERBERATING ACCRETION DISCS IN ACTIVE GALAXIES

Stefan J. Collier

A Thesis Submitted for the Degree of PhD
at the
University of St Andrews

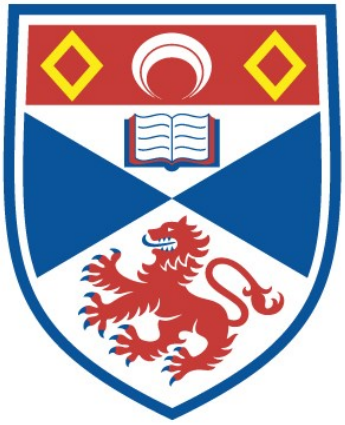

1999

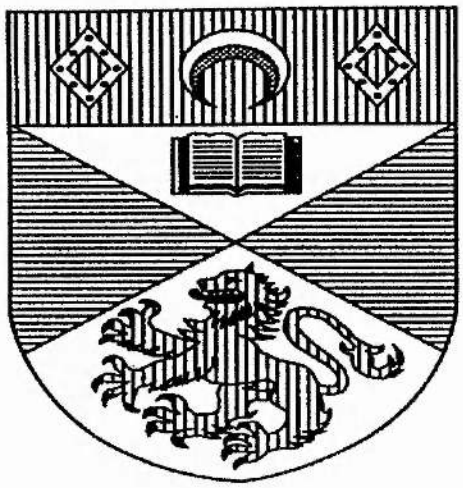

THE UNIVERSITY OF ST ANDREWS

Measuring the Hubble Constant from Reverberating Accretion Discs in Active Galaxies

Stefan J. Collier

Submitted for the degree of Ph.D.

September 1998

ProQuest LLC.
789 East Eisenhower Parkway
P.O. Box 1346
Ann Arbor, MI 48106 – 1346

DECLARATIONS

I, Stefan Collier, hereby certify that this thesis, which is approximately 40000 words in length, has been written by me, that it is the record of work carried out by me and that it has not been submitted in any previous application for a higher degree.

date signature of candidate

10/9/98

I was admitted as a research student in October, 1995 and as a candidate for the degree of Ph.D in October, 1996; the higher study for which this is a record was carried out in the University of St. Andrews between 1995 and 1998.

date signature of candidate

10/9/98

I hereby certify that the candidate has fulfilled the conditions of the Resolution and Regulations appropriate for the degree of Ph.D in the University of St. Andrews and that the candidate is qualified to submit this thesis in application for that degree.

date signature of supervisor

25 Jan 99

In submitting this thesis to the University of St. Andrews I understand that I am giving permission for it to be made available for use in accordance with the regulations of the University Library for the time being in force, subject to copyright vested in the work not being affected thereby. I also understand that the title and abstract will be published, and that a copy of the work may be made and supplied to any bona fide library or research worker.

date signature of candidate

10/9/98

ACKNOWLEDGMENTS

I sincerely thank my thesis supervisor Keith Horne for his constant enthusiasm, fascinating insight, support, and friendship over the past few years.

The love and support of my mum and dad, and wider family has been deeply appreciated and much needed. A special thanks to Elley for her support and friendship throughout.

Finally, I have enjoyed discussions with a number of people, including; Shai Kaspi and all the people at the Wise Observatory, Ignaz Wanders, Mike Goad (thanks for proof-reading the thesis), Brian Espey, and Dave James (thanks for the LaTeX advice).

PREFACE

This thesis is primarily based on papers [4] and [5], from the publication list detailed below. Chapter 5 will form the basis of a paper on "revealing accretion discs in active galaxies".

Publications

1. Wanders, I. et al. (*inc* Collier, S.), APJS, 113, 69, 1998.

2. Peterson, B. M., Wanders, I., Horne, K., Collier, S., Alexander, T., Kaspi, S., and Maoz, D., PASP, 110, 600, 1998.

3. Dietrich, M. et al. (*inc* Collier, S.), APJS, 115, 185, 1998.

4. Collier, S., Horne, K., Kaspi, S. et al., APJ, 500, 162, 1998.

5. Collier, S., Horne, K., Wanders, I., and Peterson, B., M., MNRAS, 302, L24, 1999.

Conference Proceedings

6. Peterson, B., M., Collier, S., Horne, K., and Wanders, I., in "Ultraviolet Astrophysics, Beyond the IUE Final Archive", ESA SP–413, 1998

7. Collier, S., Horne, K., Wanders, I, and Peterson, B., M., in "Accretion Processes in Astrophysical Systems: Some Like it HOT!", AIP Conference Proceedings 431, eds. Holt, S., S. & Kallman, T., R., 231, 1998

8. Wanders, I., Collier, S., Horne, K. and Peterson, B., M., in "Accretion Processes in Astrophysical Systems: Some Like it HOT!", AIP Conference Proceedings 431, eds. Holt, S., S. & Kallman, T., R., 227, 1998

9. Collier, S., Horne, K., Peterson, B., M., and Wanders, I., to appear in "Quasars as Standard Candles for Cosmology" Workshop proceedings, ed. Ferland, G., 1999

THE UNIVERSITY OF ST ANDREWS

Measuring the Hubble Constant from Reverberating Accretion Discs in Active Galaxies

Submitted for the degree of Ph.D.

September 1998

Stefan J. Collier

ABSTRACT

The standard paradigm of active galactic nuclei (AGN) postulates that their luminosity, $L \sim 10^{39-48}$ erg s^{-1}, derives from the accretion of gas onto a supermassive black hole, mass $M \sim 10^{6-9} M_{\odot}$, at the centre of a host galaxy. Echo or reverberation mapping affords a method of relating flux variations at different wavelengths to determine the nature of the flux emitting regions, with μ-arcsecond resolution.

The results of an intensive two-month campaign of ground based spectrophotometric monitoring of the Seyfert 1 galaxy NGC 7469, with a temporal resolution of ≤ 1 day, are presented. Application of echo mapping techniques reveal the virial mass of the central source to be $M_{\rm NGC\ 7469} \sim 10^{6-7} M_{\odot}$, and a compact broad Balmer line emitting region ~ 5 light days from the central source. Together, this evidence suggests the existence of a supermassive black hole in NGC 7469. Further, evidence for significant wavelength-dependent continuum time delays is presented, with optical continuum variations lagging those at UV wavelengths by about 1-2 days. The wavelength-dependent time delays, $\tau(\lambda)$, are consistent with the predicted $\tau \propto \lambda^{4/3}$ relationship for an irradiated blackbody accretion disc with temperature structure $T(R) \propto R^{-3/4}$, and hence may represent the indirect detection of an accretion disc structure in NGC 7469.

It is shown that wavelength-dependent time delays test the standard black-hole accretion disc paradigm of AGN, by measuring $T(R)$ of the gaseous material surrounding the purported black hole. Moreover, a new direct method is presented that combines observed time delays and the spectral energy distribution of an AGN to derive a redshift-independent luminosity distance; assuming the observed time delays are indeed due to a classical accretion disc structure. The luminosity distance permits an estimate of the Hubble constant, H_0–the expansion rate of the Universe. The first application of the method yields $H_0(\cos i/0.7)^{1/2} = 38 \pm 7\,\mathrm{km\ s^{-1}\ Mpc^{-1}}$. A more accurate determination of H_0 requires either an independent accurate determination of the disc inclination i or statistical average of a moderate sample of active galaxies. This method permits determination of redshift-independent luminosity distances to AGNs, thereby, giving a new route to H_0, and by extension to fainter objects at $z \sim 1$, q_0.

CONTENTS

LIST OF FIGURES

LIST OF TABLES

Chapter 1

Introduction

1.1 Basic Definition of Active Galactic Nuclei

An active galactic nucleus (AGN) is a compact source, in the centre of a galaxy, that emits large amounts of energy (not completely attributable to stellar processes) across the entire electromagnetic spectrum. Typical bolometric luminosities are $L \sim 10^{39-48}$ erg s^{-1}. There is considerable diversity in the morphology of active galaxies, §1.2, for example; Seyfert 1 galaxies with masses of $M \sim 10^{6-7} M_{\odot}$ and typical optical radial sizes $R \sim$ light days, emit optical luminosities comparable to that of the integrated starlight from the underlying host galaxy.

The relevance of AGN to astrophysics is manifold. Their enormous luminosities from compact regions immediately implies both theoretical and observational exotica. They afford the opportunity to investigate non-stellar energy generation mechanisms, and develop theoretical understanding of relativistic astrophysics by; for example, analysis of the relativistic jets of electrons that blast out from their central regions, and the formation of X-ray Fe Kα emission lines in strong gravitational fields, §1.4 and §1.5. Their extraordinary broad-band emission characteristics have fueled technological advances, e.g. the development of X-ray and IR astronomical instrumentation to enhance our understand-

ing of poorly understood wave-bands, affording insights into complex radiation emission processes.

Furthermore, their high luminosities allow them to be observed at large redshifts, e.g. we can look back in time to when the Universe was about 7% of its current age. Hence, AGN are a unique tool for probing the evolving chemical and spatial distribution of matter in the Universe. We can investigate the epoch for discrete matter formation in the early Universe. Concurrently, the belief that at least 40% of all nearby galaxies display AGN-type behaviour (§1.2) has important implications for their local space density and hence aids understanding of their cosmological evolution and contribution to the X-ray background. Finally, if indeed AGNs can be used as cosmological 'standard candles' to calibrate the extragalactic distance scale (§4), this allows determination of a size scale and age of the Universe, and constrains its geometrical configuration.

1.2 A Brief Historical Perspective and Taxonomy of AGN

A diverse classification scheme embodies the richness of the AGN phenomenon, and is based on their differing observational characteristics, e.g. the type of galaxy within which the AGN resides, emission-line characteristics, dominant emission of a particular energy, polarization, and variability characteristics. We briefly discuss the main types of AGN and their characteristics, in an historical context. For complete introductions to the world of AGN, the reader is referred to the excellent books of Robson (1995) and Peterson (1997).

The discovery of a class of similar galaxies (NGC 1068, NGC 1275, NGC 3516, NGC 4151, and NGC 7469) dates back to Seyfert (1943). Seyfert galaxies are typically barred spiral galaxies, of morphological type SbII or SbIII. Their nuclear optical luminosities, $L_{\rm opt} \approx 10^{37-40}$ erg s^{-1}, are comparable to the integrated optical emission of the underlying host galaxy, i.e. the emission from, typically, $\sim 10^{11}$ stars. There are two types of

Seyfert galaxies. Seyfert 1's emit strong, broad permitted and semi-forbidden emission lines, and narrow forbidden and permitted lines; where the use of 'broad' and 'narrow' denote typical full-width-half-maximum (FWHM) emission-line velocities of 5000 km s^{-1} and 500 km s^{-1} respectively. Furthermore, they are strong emitters of UV and X-ray radiation. Seyfert 2 galaxies display strong narrow forbidden lines and are weak emitters of UV and X-ray radiation. However, they emit strongly in the IR.

Technological improvements in the angular resolution of radio telescopes during the late 1950s, led to the discovery of strong radio emitting star-like objects, and permitted contemporaneous optical identifications of the sources. Schmidt (1963) showed that one of these star-like objects, 3C 273, was of extragalactic origin by noting the observed broad emission lines were actually the hydrogen Balmer series seen at a redshift $z \approx 0.158$; much larger than the small redshifts of the Seyfert galaxies, typically, found nearby. This study signalled the first steps in understanding these objects, referred to as 'quasi-stellar radio sources' or quasars. Quasars are the most luminous AGN with $L \sim 10^{46-48}$ erg s^{-1}, and are generally found in elliptical galaxies. Their large luminosities tend to obscure the fainter starlight from the surrounding host galaxy. They are mostly radio-quiet sources, i.e. comparatively weak emitters of radio emission, that emit broad permitted emission lines and are strong X-ray emitters. They are distinguishable from Seyfert galaxies by the weakness/absence of narrow permitted and forbidden lines in their spectra.

At about the same time (1960s) radio galaxies were identified as a class of AGN. Typically found in elliptical galaxies, they are radio-loud sources. The radio emission is associated with jet features that emanate from their central regions. Similarly, two main sub-classes are identified through optical observations. Broad Line Radio Galaxies (BLRGs) are characterized by the presence of strong broad emission lines, and are strong X-ray emitters. Narrow Line Radio Galaxies (NLRGs) emit narrow forbidden lines, and

emit weakly at X-ray energies.

The categorization of Blazars as a class of AGN occurred in the 1970s. The subsequent subdivision of the class reveals Optically Violent Variables (OVV) and BL Lacertae objects. They are characterised by strong emission over the entire electromagnetic spectrum, displaying extreme forms of variability, e.g. a change in magnitude of a tenth of a magnitude on time-scales of a day or less, and about 3% variable polarized emission, c.f. $\leq 1\%$ for most AGNs. BL Lacertae sources were, historically, distinguishable from their OVV cousins by the absence of strong emission or absorption lines in their spectra. However, Corbett et al. (1996) and references therein, present optical spectropolarimetry showing broad Hα emission in BL Lacertae, the archetypal object defining the Blazar phenomenon. Further, Blazar AGNs are thought to contain a relativistic jet pointing close to the observer's line-of-sight which leads to Doppler-beamed continuum emission.

Low-ionization nuclear emission-line galaxies (LINERs) were first identified by Heckman (1980), and are the least luminous class of AGN, with $L \sim 10^{37-9}$ erg s^{-1}. LINER galaxies are very common, with at least 40% of all galaxies brighter than $B = 12.5$ mag emitting AGN-like spectra (Ho (1998) and references therein). Ho (1998) suggests a similar sub-division of LINERs to that of Seyfert galaxies, based on the detection of broad emission-lines and detection of broad emission in the polarized flux of NGC 1052, Barth et al. (1998) and §1.3, however, the evidence remains ambigious. Their spectra display strong low-ionization emission-lines, e.g [O I].

Narrow-Line X-ray galaxies (NLXGs) were identified in the late 1970s, Ward et al. (1978). Their characteristics, again, resemble those of Seyfert galaxies, i.e. strong narrow lines and strong X-ray emitters, but tend to have lower luminosities than typical Seyfert galaxies. Their UV and optical spectra appear to be heavily reddened by dust within the galaxy.

1.3 The Unification of AGN

§1.2 discussed the bewildering variety of AGN observed. A fundamental issue concerns the inter-relationship of the above AGN phenomenology, and whether the observed differences reflect real differences in the underlying physical processes at work. It is widely believed that a large fraction of the observed differences arise solely due to the orientation of the observed AGN, Antonucci (1993) and references therein.

About 90% of all AGN are radio-quiet, with the remaining 10% or so primarily radio galaxies and Blazars, i.e radio-loud. Early radio-quiet unification scenarios of Antonucci (1982), Antonucci (1984), and Antonucci (1985) proposed that the distinction between type 1 and 2 Seyfert galaxies arises due to differences in the observer's line of sight. Spectropolarimetric observations of the Seyfert 2 galaxy NGC 1068 (Antonucci (1985)) and NLRG 3C 234 (Young et al. (1998)) show polarized broad emission-line flux profiles, suggestive that the line of sight is intercepted by some obscuring medium, possibly the molecular torus of gas and dust surrounding the central regions, §1.4. For Seyfert 1 galaxies the observer's line of sight is not obscured by this medium, and the broad-line emitting region can be viewed directly. This evidence is strengthed by the comparative weakness of the X-ray emission in Seyfert 2 galaxies. Alternative scenarios suggest the fading, disappearance and re-appearance of the broad line-emitting region, as observed, for example, in NGC 4151 (Penston & Pérez (1984)). However, the 'trigger' for this behaviour is not understood.

The contrasts observed in radio-loud AGN are thought to be characterised by differences between the observer's line-of-sight and the orientation of the relativisitic radio jets that power the giant radio lobes, Barthel et al. (1989) and Hes et al. (1993). The relativistic beaming of the radiation emitted by the jets explains the rapid variations and high luminosities seen in radio-loud AGN, Urry & Padovani (1995).

The primary difference between radio-loud and radio-quiet AGN is thought to be due to different spin rates of the black hole powering the activity (Blandford (1990) and Wilson & Colbert (1995) and references therein). These authors suggest that radio-loud AGN contain rapidly spinning black holes, acquired via the merging of two similarly large-sized black hole masses, and radio-quiet AGN contain slowly rotating black holes since the conventional accretion process does not spin-up the black hole efficiently. Their model explains the dichotomy between the host galaxies of radio-loud and radio-quiet AGN, i.e. elliptical and spiral galaxies respectively, the existence of powerful radio galaxies, and the rarity of radio-loud AGN.

1.4 The Standard Paradigm of AGN

The standard paradigm of an AGN postulates that their luminosity derives from the accretion of gas onto a supermassive black hole, residing at the centre of the galaxy (Zel'dovich & Novikov (1964), Salpeter (1964), and Lynden-Bell et al. (1969)). The gas spirals inwards and forms an accretion disc, providing a mechanism by which angular momentum can be transported outwards and a sink for the conversion of gravitational energy into continuum radiation via viscous torques.

The linear extent of the disc is of the order of light hours-days, with the black hole 'size' governed by the Schwarzschild radius, i.e. light seconds-hours. The hot inner regions of the accretion disc are inflated by high radiation pressures, and emit most of the high energy radiation, e.g. X-rays, $\gamma-$ rays. The outer regions of the disc may merge with an optically thick molecular torus of gas and/or dust that surrounds the black hole-disc system, and emits strongly in the IR. The location of the torus relative to the central source is of the order of light months-years. The torus material will obscure the central regions if the observer's line-of-sight is close to the plane of the disc.

Optically thick clouds of gas emit the broad emission lines and are distributed $\sim$ light days from the central source–the Broad emission Line Region (BLR). Their geometrical configuration and kinematics remain essentially unknown. Further from the central source $\sim$ light years-centuries, are narrow-line emitting clouds. The Narrow emission Line Region (NLR) is spatially resolvable from the ground, unlike the BLR, and reveals that the ionizing continuum is not isotropic on kiloparsec scales, Wilson (1996) and Unger et al. (1987).

Elliptical active galaxies, e.g quasars and radio galaxies (§1.2), often possess collimated bi-polar relativistic radio jets. The collimation of the jets is thought to be related to the inner inflated regions of the accretion disc. The jets blast out into the interstellar medium to form giant radio lobes.

The main competitor to the standard model is the starburst model of Terlevich et al. (1994). The AGN activity is that of young stars and compact supernova remnants from a nuclear burst of star formation. This model has some success in explaining the observed broad emission line variability, line ratios and luminosities, but has difficulties in explaining the observed rapid X-ray variability on timescales of light seconds (Lawrence & Papadakis (1993)). We do not discuss this model further.

1.5 Evidence for the Standard Paradigm

The standard paradigm, in which the existence of black holes and accretion discs is postulated, remains unproven. Black holes, by definition, tend to be hard to observe! However, there are a number of indirect independent lines of evidence that lend credence to the standard paradigm.

Rapid X-ray variability on timescales of a few light hours coupled with coherence arguments strongly suggest a compact high-energy continuum source, Terrell (1967).

A lower limit to the mass M of the compact object can be determined from the Ed-

dington limit (Zel'dovich & Novikov (1964)), $M > 10^6 L_{44} M_\odot$ where L_{44} is the bolometric luminosity of the AGN in units of 10^{44} erg s^{-1}. Hence, the Eddington limit implies $M > 10^6 M_\odot$ for a typical Seyfert 1 galaxy with $L = 10^{44}$ erg s^{-1}.

Together the above two arguments, i.e. compact massive sources, imply a deep gravitational potential. Rees (1984) argues that if the potential well is sufficiently deep then the end product will be a massive black hole regardless of the initial configuration of the gaseous material. Moreover, the ease with which accretion processes generate large luminosities from small volumes is itself a compelling argument.

Other emission-line and dynamical evidence that supports the standard paradigm includes the following: Water vapour maser emission line velocities in NGC 4258 show Keplerian motion about a massive compact object, mass $M > 10^7 M_\odot$ within a radial distance $r < 0.13$ pc, and support the black-hole accretion disc hypothesis (Miyoshi et al. (1995)). HST observations of M87 show evidence of rapidly rotating Hα emission, and suggest a $10^9 M_\odot$ concentration of material within 18 parsecs (Ford et al. (1994)). Gravitationally redshifted, relativistic X-ray Fe Kα emission in MCG-6-30-15 can be sucessfully interpreted as emission from the innermost regions of the accretion disc, where relativistic effects are important, and support the notion of a black hole-accretion disc system in this object (Tanaka et al. (1995)). Finally, the successful interpretation of the 'Big Blue Bump' spectral feature in AGN, §1.6, as thermal emission from an accretion disc is good circumstantial evidence of accretion disc structures, albeit non-unique (Shields (1978), Malkan & Sargent (1982), and §5.1).

1.6 The Continuum Energy Distribution

As mentioned in §1.1 one of the characteristics of AGN activity is the emission of energy across the entire electromagnetic spectrum, suggestive of a nonstellar origin, Peterson

(1997). The AGN spectral energy distribution (SED) can be approximated as a power law over a limited range in frequency,

$$f_\nu = C\nu^{-\alpha}, \tag{1.1}$$

with f_ν the observed flux of ionizing photons (erg cm^{-2} s^{-1} Hz), C a constant and α the spectral index, usually between zero and unity. Figure 1.1 presents the mean SED for a sample of radio loud and radio quiet quasars, after Elvis et al. (1994).

The gaps in the mean SEDs of Fig. 1.1 occur for a variety of reasons; For example, high energy radiation, i.e. X-rays/γ-rays, do not penetrate the Earth's atmosphere and require satellite based observations. The lack of coverage in the EUV is a result of absorption by neutral hydrogen in the galactic disc, and prohibits detection of extragalactic sources between about 100-912Å (It is frustrating that this unobservable spectral range is fundamental to our understanding of AGN, since it is likely to play an important role in the ionization of the line-emitting regions), and water vapour absorption in the Earth's atmosphere between about 1μm and 300μm severely restricts observations at IR and longer wavelengths. Fig. 1.1 includes data taken through approximately transparent atmospheric 'windows' in the near IR, up to about 20μm, and IRAS (Infrared Astronomical Satellite) measurements from above the earth's atmosphere.

The deviations of the mean SEDs of Fig. 1.1 from a simple power law over a large range in frequency suggests that the continua have a multi-component structure. Continuum studies aim to understand the nature of the various spectral components and the underlying physical mechanisms, e.g the predominance of thermal emission over non-thermal emission processes has implications for the isotropy of the continuum radiation and the importance of reprocessed emission components, §1.9.7.

Table 1.1 summarizes the continuum distribution described by Fig. 1.1. Column 1 details the continuum region considered, column 2 gives the approximate power law expo-

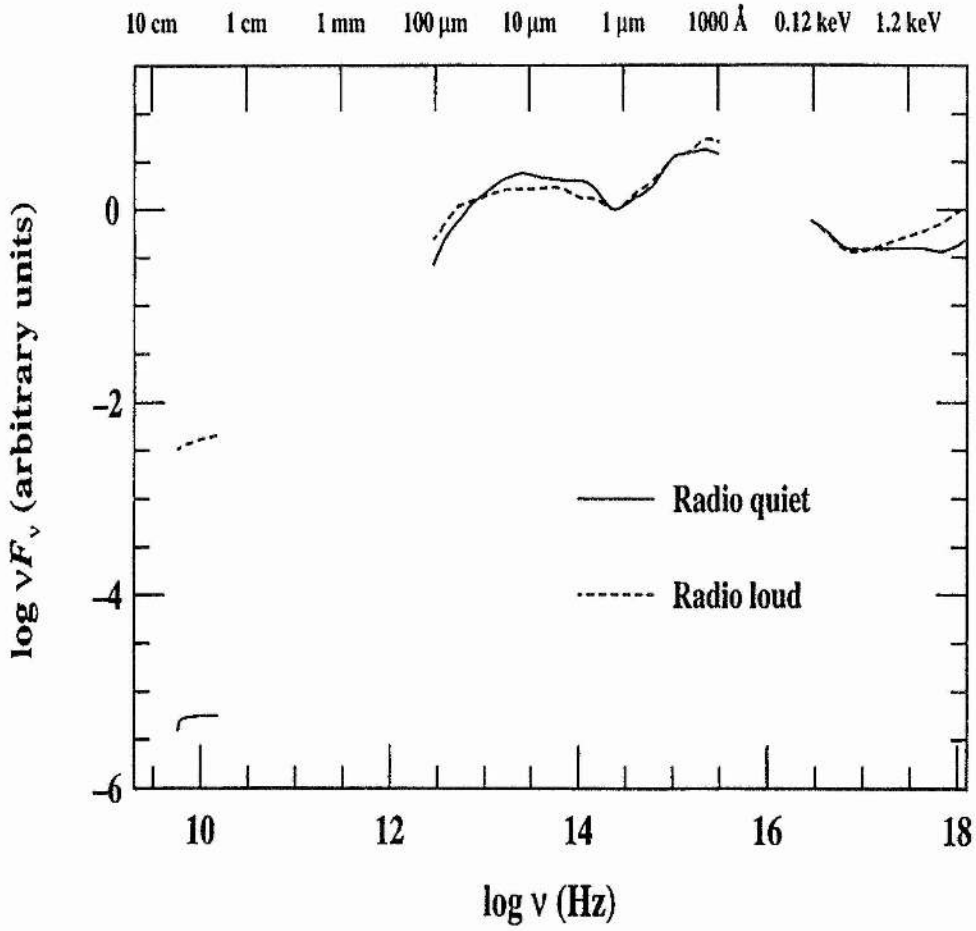

Figure 1.1: The solid and dashed lines represent mean spectral energy distributions (SEDs) for a sample of radio-quiet and radio-loud quasars (after Elvis et al. (1994), and as detailed by Peterson (1997)). The SEDs have been normalized at a wavelength of 1μm.

nent for the given spectral range, column 3 details any special features of the continuum in this regime, and column 4 lists a selection of relevant references.

Differences are evident between the SEDs of radio-loud and radio-quiet AGN, and/or between the distinct radio-loud and radio-quiet AGN themselves. These include; the rapid decrease in emission for radio-quiet AGN at low energies–the sub-millimeter break, and the weaker strength of the BBB for lower luminosity Seyfert 1 galaxies and quasars (Malkan & Sargent (1982)). The differences are likely to reflect the relative dominance of different continuum emission processes, e.g. thermal or non-thermal emission.

The exact/intrinsic form of a given SED, e.g Fig. 1.1, can be drastically affected by the reddening and extinction of continuum (and emission-line) fluxes, non-simultaneity of multi-wavelength observations, contamination by a constant wavelength-dependent stellar component, and/or variable contamination by line emission and additional continuum components, e.g. Balmer continuum emission. The SEDs detailed in Table 1.0, suffer from at least one and typically more of the above deficiencies, and therefore must be viewed with some caution. In Chapter 5 we investigate the shape of the UV/optical continuum for a sample of, primarily, radio-quiet Seyfert 1 galaxies, and explore the aforementioned continuum-altering effects.

1.7 The Basics of Echo Mapping

Echo or reverberation mapping is a tool for indirectly imaging astronomical sources, e.g. binary star systems and AGN, with μ−arcsecond resolution, far superior to ground based resolutions or milli-arcsecond resolution of the Hubble Space Telescope (HST). The method is based on the Physics of light travel time, and studies the time-delayed and Doppler-shifted response of one emission component relative to another related component to infer information about the geometry and kinematics of the emission regions, Bahcall et al.

Table 1.1: The Mean Continuum Spectrum of AGN

Spectral Range	α	Features	References
$\sim 1 - 4\mu$m (near IR)	1.0-2.0	small bump $\sim 3.5\,\mu$m[1]	Neugerbauer et al. (1979), Edelson & Malkan (1986) Carleton et al. (1987), Puetter (1987)
$\sim$ 0.5-0.08 μm (optical/UV)	0.3-0.7	Strong bump $\sim$1000-4000Å[2]	Shields (1978), Malkan & Sargent (1982) Malkan & Filippenko (1983), Netzer & Ferland (1984)
$\sim$ 100-1000Å (EUV/Far UV)	1.4	one power-law[3] From IR-soft X-ray	Kinney et al. (1985), Wilkes et al. (1987) Lawrence & Elvis (1982), Glass (1979)
$\sim 0.1 - 3.5$ keV (Soft/Medium X-rays)	0.5-1.0	Soft X-ray excess[4]	Arnaud et al. (1985), Branduardi-Raymont et al. (1985) Wilkes et al. (1987), Turner & Pounds (1989), Gondhalekar et al. (1994) Mushotzky et al. (1980)
$\geq$ 10 keV (Hard X-rays)	–	Compton Reflection[5]	Pounds (1990), Guilbert & Rees (1988) Lightman & White (1988)

Notes:

1 - Thermal emission from dust near BLR, and/or free-free emission from dense clouds near BLR or optically thin emission from accretion disc. Observed in both radio-quiet and radio-loud AGN.

2 - The strong feature is the 'Big Blue Bump' (BBB), containing most of energy for radio-quiet AGN. Optically thick emission from accretion disc, and/or free-free emission from optically thin plasma. A weaker bump at about 3000Å is attributable to Fe II line + Balmer continuum emission.

3 - The single suggested power-law component underlies the UV/optical BBB emission, perhaps of synchrotron origin.

4 - Variable soft X-ray excess, probable high energy tail of the BBB produced in electron scattering atmosphere of accretion disc.

5 - High energy tail/reflection component due to reflection of X-rays from cold matter, possibly the accretion disc.

(1972) and Blandford & McKee (1982).

There are a number of good review articles that elucidate the method, Blandford & McKee (1982), Blandford (1990), Osterbrock (1991), Peterson (1993), Netzer & Peterson (1997), and Ulrich et al. (1997). The discussion that follows is largely based on the cited review articles and references therein.

The development of the field has concentrated on the variable response of the broad emission lines to prior changes in the observable continuum flux (note the observable and ionizing continuum are not necessarily identical, see later), e.g. Ulrich et al. (1984). Fig. 1.2 presents a schematic picture of a thin spherical shell broad line region, surrounding a variable central source. Consider the scenario of an isotropic continuum outburst that propagates outwards towards the spherical thin shell. The observer sees different parts of the BLR respond at different times because all points of the BLR are not equidistant from the observer. A light travel time delay is observed between detection of the emission line response and continuum outburst on account of the longer light travel time path taken from the continuum source–emission region–observer than the direct path of the continuum radiation , i.e. continuum source–observer. Common sense (i.e the finite speed of light) dictates that in this simple scenario the observer will see the front side of the emission shell respond before the back side, given its closer proximity to the observer. The response of the emission region at a given time delay τ is described by an ellipsoidal surface, with the central source and observer defining the two foci. The series of nested ellipsoids, describing the range of time delays present in the system, may be approximated by a series of paraboloidal surfaces for the case where the observer is situated at a distance $\rightarrow \infty$ from the central source.

Obviously, the detailed response of the broad emission lines to continuum variations is very much dependent on the geometry and kinematics of the emission region, and variable

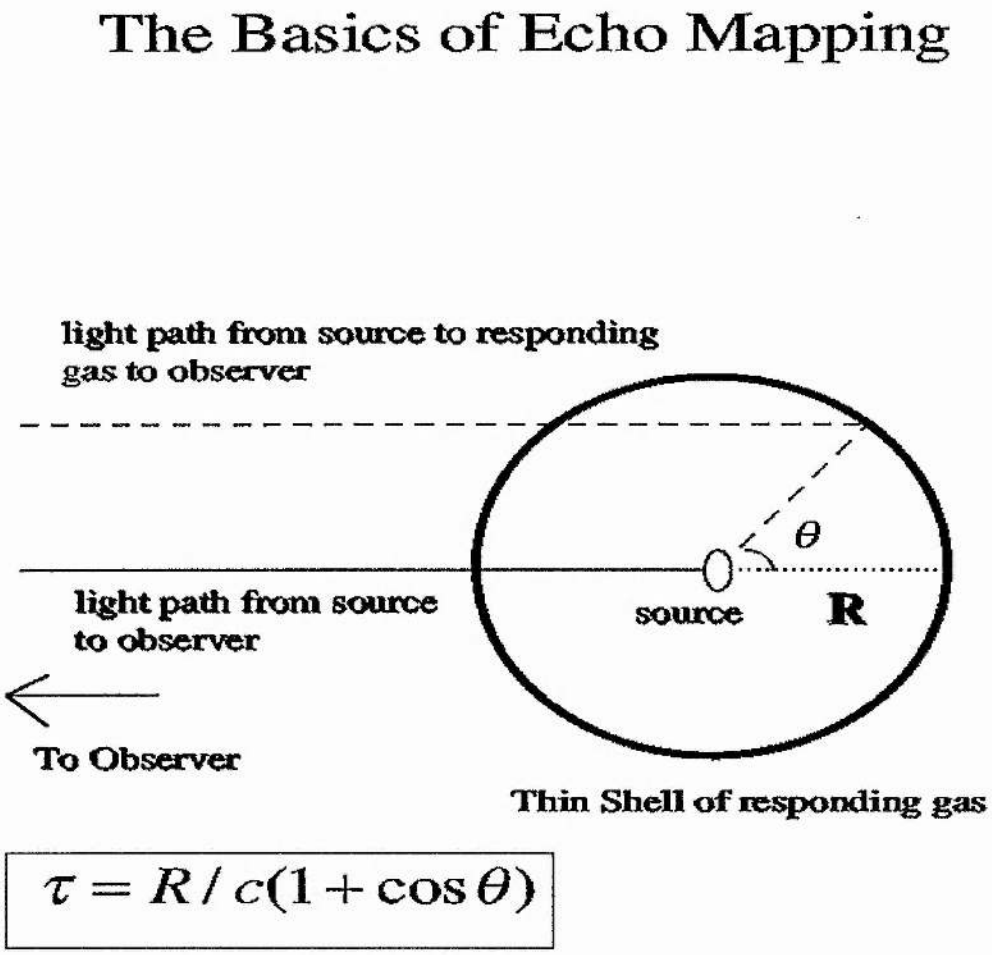

Figure 1.2: A schematic thin shell BLR demonstrates the origin of light travel time delays between detection of the emission-line response and prior continuum outburst.

emissivity or responsivity of the gas permeating the emission region. A transfer function is defined that characterizes the response of an emission line to a δ function continuum outburst, handily encompassing the unknown geometrical and kinematic dependencies of the emission–line response and the detailed physics of the gas responsivity. Transfer functions for a number of different geometries, including thick and thin spherical shells and discs are derived by, for example, Blandford & McKee (1982), Robinson & Pérez (1990), Welsh & Horne (1991), Pérez et al. (1992), and Goad & Wanders (1996).

The constructs of echo mapping rely on a number of assumptions. Firstly, that there is a singular continuum source that is much smaller than the emission region considered. Secondly, that the filling factor of the emission region is a small fraction of the total emission volume, and the photons can propagate un-impeded at the speed of light. Thirdly, that there is a simple, not necessarily, linear relationship between the observable continuum and the ionizing continuum flux that drives the emission-line response, and finally that the light travel time-scale, $t_{\rm LT} \approx r/c$, is the dominant time-scale present.

The latter assumption is justified by considering, primarily, the recombination time-scale, $t_{\rm rec}$, for emission line variations resulting from changes in the continuum level, and the time-scale for dynamical changes within the broad emission line region, $t_{\rm dyn}$. The recombination time-scale is given by $t_{\rm rec} = 1/n_e\alpha_B \approx 40 n_{11}^{-1}$ sec with n_e the electron density ($n_{11} = n_e/10^{11}$ cm^{-3}) and α_B the case B hydrogen recombination coefficient. For a typical BLR density of $n_e = 10^{11}$ cm^{-3} (see §1.9.3), $t_{\rm rec} \approx 40$ seconds which is much smaller than typical emission-line variation time-scales of a few light days-months. The dynamical time-scale governs the time-scale for geometrical changes in the BLR configuration, and is approximated by the time it would take a line emitting cloud to cross the BLR, i.e. $t_{\rm dyn} \approx r/\Delta v_{\rm FWHM}$ with $\Delta v_{\rm FWHM}$ the full-width-half maximum of an emission-line. Hence, $t_{\rm dyn} \approx 60 t_{\rm LT}$ for a typical broad emission line $\Delta v_{\rm FWHM} = 5000\,{\rm km\ s^{-1}}$. Other notable

time-scales include the sound crossing time, the photon diffusion time-scale and the cloud formation time-scale (see Taylor (1996) and Goad (1995)), all of which can be estimated to be either much larger or smaller than the light travel time-scale. Hence, it is likely that this assumption is justified.

The former assumptions, e.g a singular continuum source, small filling factors, and a simple relationship between the observable and ionizing continuum, are not as clearly justified, but in most cases are a good first-order approximation given the standard paradigm of AGN, the existence of closely correlated emission-line and continuum variability (For example, Ulrich et al. (1984)) and from estimates of the filling factor of the BLR, Peterson (1994).

The mathematical formalism of echo mapping defines,

$$L(v,t) = \int_{-\infty}^{\infty} \Psi(v,\tau) C(t-\tau) d\tau, \tag{1.2}$$

where $C(t)$ is the continuum light curve, $L(v,t)$ is the emission line light curve as a function of line-of-sight velocity, and $\Psi(v,\tau)$ is the transfer function–a projection of the BLR's six–dimensional phase–space distribution into two–dimensions. The goal of echo mapping is to use the observables $L(v,t)$ and $C(t)$ to provide an unambiguous solution to the transfer function, and hence determine the geometry and kinematics of the emission line region.

The quality of the data, typically, precludes the accurate determination of the 2-D transfer function. For the past $\sim$ 10 years, since the inception of large scale co-ordinated multi-wavelength monitoring campaigns (e.g the International AGN Watch and LAG collaboration, see §1.9), efforts have primarily focussed on the recovery of the first moment of the 1-D transfer function. The 1-D transfer function is defined by,

$$L(t) = \int_{-\infty}^{\infty} \Psi(\tau) C(t-\tau) d\tau. \tag{1.3}$$

$\Psi(\tau)$ is the response of the complete emission-line integrated over the line-of-sight velocity.

The first moment of the transfer function defines a 'lag' or 'time-delay' between the continuum and emission-line light curves, and gives a 'size' scale for the emitting region. The most common method used to measure the 'lag' is based on the cross-correlation methodologies soon to be discussed, where the 'lag' is the temporal shift between the continuum and emission-line light curves that maximizes the correlation coefficient. We defer a full discussion of recent results to §1.9

1.8 The Precepts of Cross-Correlation Analysis

In this context, a cross-correlation analysis is a regression analysis of two observed light curves or time series; a continuum light curve $C(t)$ and an emission line light curve $L(t)$ that is delayed relative to the former by some temporal lag τ. The 'lag' is defined to be the value of τ that maximizes the correlation coefficient between the two time series. A cross-correlation coefficient (CCF), is defined by

$$CCF(\tau) \equiv \int_{-\infty}^{\infty} L(t)C(t-\tau)dt, \tag{1.4}$$

where $C(t-\tau)$ is the continuum light-curve measurement at an epoch $t-\tau$.

The continuum auto-correlation function (ACF) is defined to be

$$ACF(\tau) \equiv \int_{-\infty}^{\infty} C(t)C(t-\tau)dt, \tag{1.5}$$

and characterizes the continuum variability time-scale.

Adopting the standard assumption of reverberation mapping that relates the emission line light curve $L(t)$ to a delayed continuum light curve $C(t-\tau)$, as discussed in §1.7 and detailed in equation 1.3, one can substitute for $L(t)$ in equation 1.4 and reverse the order of integration to express the CCF as

$$CCF(\tau) = \int_{-\infty}^{\infty} \Psi(\tau^{'})ACF(\tau-\tau^{'})d\tau^{'}, \tag{1.6}$$

where $\Psi(\tau')$ is the transfer function.

Equation 1.6 shows that the CCF is the convolution of the transfer function, that describes the geometry and kinematics of the emission region, and the continuum auto-correlation function. The lag is usually measured from the peak or centroid of the CCF distribution, and clearly depends on the nature of the continuum variations as well as the transfer function pertinent to the emitting region. Furthermore, the cross-correlation analysis discussed here assumes the time series' are stationary, that is their means and variances are independent of time. This is not always a good assumption, since some CCFs appear to change with time, perhaps reflecting changes in the continuum auto-correlation function, and/or real changes in the distribution of responding gas (Wanders (1995)).

For a thin shell BLR model the peak of the CCF accurately determines the size of the emission region, however, for more complex and extended BLR geometries it is not clear how the peak and centroid measurements relate to the properties of the emission region. Maoz & Netzer (1989) calculated 'cross-correlation peak distributions' that determined the significance of measured 'lags' for given BLR geometries, and showed that the results depended strongly on the specified BLR geometry and the assumed continuum variability time-scale. Robinson & Pérez (1990) presented analytical calculations for the response of an ensemble of broad line emitting clouds non-uniformly distributed within a thick spherical shell. These authors demonstrate that the peak of the CCF is a function of the shell thickness, the exact form of the volume emissivity law adopted, the continuum pulse duration, and (sampling) windowing effects. In particular, the peak lag is biased towards the inner shell radius for thick geometries, because of the less coherent response of material further out from the continuum source (noted earlier by Gaskell & Sparke (1986) and Edelson & Krolik (1988)).

Increasingly, the centroid of the CCF is the preferred measurement in variability stud-

ies, since Koratkar (1991) and Penston (1990) showed that the centroid of the CCF, $\tau_{\rm cen}$, is a measure of the luminosity-weighted radius R of the reprocessing emission region. However, numerical simulations by Pérez et al. (1992) show that the correspondence between $\tau_{\rm cen}$ and R of given BLR models is not exact, with discrepancies as large as a factor of 2 in the sense that $\tau_{\rm cen}$, determined from the CCF, is smaller than the actual model value of R. This most likely relates to the width of the sampling window and/or the precise nature of the continuum variations. The aforementioned discussion highlights the care one must exhibit in interpretation of the size-scale measurements determined by a cross-correlation analysis, and the necessity of evaluating the uncertainties inherent in the determination of the 'lags'.

Aside from the aforesaid fundamental problems, there are numerous practical problems in the cross-correlation analysis of astronomical time series. These are due to the inevitable irregular sampling of the light curves. Attempts to solve the problems posed have led to the development of a number of numerical techniques that aim to recover the correct CCF; these include the Interpolation Cross-Correlation Function method (ICCF) of Gaskell & Sparke (1986), Discrete Correlation Function method (DCF) of Edelson & Krolik (1988), and the Z–transformed Discrete Correlation Function algorithm of Alexander (1997).

The ICCF method interpolates, say, the continuum light curve $C(t)$, and pairs each emission line light curve $L(t)$ point with the interpolated continuum value at $C(t-\tau)$ in order to compute the CCF. The procedure is then repeated with the pairing of continuum values $C(t)$ with interpolated emission line values $L(t+\tau)$ to compute a second CCF. The results are then averaged to produce the final CCF. The ICCF generally outperforms other methods on poorer quality data. However, it approximates the true light curve behaviour which may be very different, and is biased towards a zero lag by correlated errors between continuum and emission-line measurements made from the same spectrum.

The DCF method avoids the problems of irregular sampling by only considering pairs of data-points in $L(t)$ and $C(t)$ that are separated by a given lag τ. To increase the cross-correlation amplitude at a given τ the CCF is binned to include all pairs of data-points with separations in the range $d\tau - \delta$ to $d\tau + \delta$. This enhances the accuracy of the CCF while degrading the resolution. The DCF has the advantages of not pre–supposing any behaviour about the light curves, and allows one to exclude pairs of continuum and emission-line fluxes that have been measured from the same spectra, thus eliminating the bias inherent in the ICCF method.

The ZDCF method uses Fisher's Z transformation and bins the CCF into equal population bins as opposed to equal time bins, c.f the DCF method. The peak position of the 'lag' and its associated error are estimated via a maximum likelihood method that accounts for the uncertainty in the ZDCF points.

White & Peterson (1994) present a general discussion of the ICCF and DCF, compare and contrast their relative strengths and weaknesses, and road-test the two methods using Monte Carlo simulations. They find that for well sampled data the results of the two methods are in good agreement, with the ICCF performance being superior for poorer quality data.

1.9 Variability Studies of AGN

1.9.1 Overview

Optical continuum variability studies of quasars dates back to at least the 1960s (Matthew & Sandage (1963)). In contrast, emission-line variability was only widely recognized in the early 1980s, see Peterson et al. (1988) and references therein.

The apparent simplicity of the reverberation mapping method, and the promise of an unambiguous determination of the geometry and kinematic structure of the broad line

region mobilized the International community to undertake a number of labour-intensive multi-wavelength monitoring campaigns.

The largest collaboration of this type is the "International AGN Watch" consortium (http://www.astronomy.ohio-state.edu/ agnwatch/) of over 100 astronomers that was born circa. $\sim$ 1987. Their aim, simply, was to obtain high quality multi-wavelength observations for continuum and emission-line variability studies of AGN. To date the AGN Watch has obtained suitable monitoring datasets on seven active galaxies, NGC 5548 (Clavel et al. (1991); Peterson et al. (1991); Peterson et al. (1992); Dietrich et al. (1993); Maoz et al. (1993); Peterson et al. (1994); Romanishin et al. (1995); Korista et al. (1995); Marshall et al. (1997)), NGC 3783 (Reichert et al. (1994); Stirpe et al. (1994); Alloin et al. (1995)), NGC 4151 (Crenshaw et al. (1996); Warwick et al. (1996); Kaspi et al. (1996a); Edelson et al. (1996)), Fairall 9 (Rodriguez-Pascual et al. (1997), Santos-Lleó et al. (1997)), 3C 390.3 (Leighly et al. (1997); Dietrich et al. (1998); O'Brien et al. (1998)), Mrk 279 (call for data issued), and NGC 7469 (Wanders et al. (1997); Collier et al. (1998); Welsh et al. (1998); Kriss et al. (1998); Nandra et al. (1998)). The main results of these datasets will be discussed in §1.9.4. The optical section of the latter monitoring campaign on NGC 7469 will be discussed in this thesis.

Other collaborations and institution–based monitoring campaigns include: The European 'LAG' collaboration, aka ' Lovers of Active Galaxies', that carried out optical spectroscopy of a comparable sample size of AGNs during , primarily, the first 6 months of 1990, see Robinson (1994) and references therein. The 'EEC' consortium, aka ' European Extragalactic Consortium', that monitored the UV spectrum of NGC 4151 with IUE for about 10 years, Ulrich et al. (1984) and Ulrich et al. (1991). The Wise Observatory based in Israel acquired substantial datasets on a number of objects, including NGC 4151, NGC 5548, and Mrk 279 (Maoz et al. (1990); Maoz et al. (1991)). Furthermore, Kaspi

et al. (1996b) is currently concluding a 5 year monitoring programme on a sample of high-luminosity AGN from the PG quasar survey. Finally, Ohio State University have completed long-term monitoring campaigns of a sample of AGN over a period of many years, Peterson et al. (1985).

1.9.2 The Aims of the International AGN Watch Monitoring Campaigns

The primary aim of the AGN Watch campaigns concerned the nature of the BLR gas distribution. More specifically, and subjectively, these initial aims can be broken down in the following way (in no particular order);

i) Measurements of the BLR radius, i.e. a 'lag' determination between the correlated continuum and delayed emission line variations.

ii) The accurate re–construction of the 1 and 2-D transfer functions, §1.7, that describe the BLR gas distribution.

iii) Determination of the black hole mass and whether the fundamental energy source powering AGN is the accretion of gas onto a supermassive black hole. Hence, acquire evidence supporting the standard AGN paradigm, §1.4.

After the first AGN Watch monitoring campaign (1989) on NGC 5548, attention was drawn to the nature of the AGN continuum. Contrary to behaviour of the emission lines, the continuum (of NGC 5548) from 1350Å to 5200Å varies synchronously to within 2 ± 2 days. This result has profound implications for the origin of the continuum emission and associated variability mechanisms, §1.9.7, and was quickly incorporated as an important question that future reverberation mapping experiments should attempt to resolve. Hence,

iv) Is there a phase difference between the UV and optical continuum variations? What is the inter-relationship between the UV/optical and X-ray variations?

All of the above monitoring campaigns have enhanced and evolved our understanding

of the central regions of active galaxies (not to mention provide us with additional exciting questions), in particular low–medium luminosity Seyfert 1 galaxies. Before focusing on the International AGN Watch monitoring campaigns, discussing the main results and their implications, (prior to the NGC 7469 campaign), we briefly digress to describe the broad-line region of AGN, since understanding its nature was a primary goal of reverberation mapping experiments.

1.9.3 The Broad Line Region (BLR) of AGN

The broad-line region (BLR) of AGN was envisaged as a collection of optically thick broad line-emitting clouds distributed with uncertain geometry and kinematics $\sim$ light days from the central source, i.e. supposed black hole. Here we discuss briefly some basic parameters of the BLR. A more complete discussion may be found in, for example, the nebular physics textbook of Osterbrock (1989).

Typical early BLR parameters, as discussed by Peterson (1997), include: Electron densities $n_e \sim 10^7 - 10^9$ cm^{-3} as evidenced by the absence or weakness of broad forbidden [O III] emission and presence of strong semi-forbidden CIII] emission, but see below and Ferland et al. (1992). Temperatures $T \sim 10^4$ K as deduced from the similarity of line intensity ratios to other ionized gas regions, e.g HII regions. A covering factor of $\sim 10\%$ that describes the fraction of the sky covered by the BLR gas. Mass of the BLR gas of about $1M_{\odot}$, and small filling factors ε of $<< 1$ that describe the amount of BLR volume that contains broad line-emitting material.

Historically, the BLR was first modelled with photoionization codes (Ferland (1985) and references therein, Ferland (1991), Ferland (1993), and Davidson & Netzer (1979)). Early models based on single clouds as infinitely plane parallel slabs of gas required the specification of the ionizing continuum, the hydrogen density at the front face of the cloud,

and the ionization parameter U, defined as

$$U = \frac{Q(H)}{4\pi r^2 n_{\rm H} c}, \tag{1.7}$$

with $Q(H)$ the total number of ionizing photons produced by the central source, r the distance between the central source and the gas cloud (i.e the BLR radius), and $n_{\rm H}$ the particle density in the cloud. Typical values for these parameters were $U = 0.01$, $n_{\rm H} = 10^9$ cm^{-3}, $Q(H) = 10^{54}$ photons s^{-1}, and yield an estimate of the BLR radius $r \approx 100$ light days.

The photoionization models of the 1980s, Kwan & Krolik (1981) and Ferland & Mushotzky (1982), were fairly successful in reproducing the observed relative intensities of the UV emission lines, but difficulties persisted. For example, the observed Balmer decrement (i.e. Hα / Hβ) remained too steep and there was an apparent deficit of emission in, for example, the Balmer continuum and Fe II lines. This so-called 'energy-budget problem' describes the need for additional ionizing photons to explain the observed continuum and emission-line strengths (Netzer (1980)).

The shortcomings of the photoionization models were compounded by the early reverberation mapping results, §1.9.4, that suggested the BLR radius was an order of magnitude smaller than that predicted by photoionization models, i.e. ~ 10 days, c.f ~ 100 days. The era of single zone photoionization modelling was thus laid to rest, which paved the way forward for a multiple component BLR structure (e.g., Collin-Souffrin et al. (1982) and Rees (1989)). We note the discrepancy in BLR radius is now resolved by the recognition that the C III] emission component is distinct to that of the other broad UV emission-lines, e.g C IV, with the C III] emission further from the central source. An upper limit to the density, appropriate for the UV broad emission lines is $\sim 10^{11}$ cm^{-3}, Ferland et al. (1992).

Collin-Souffrin et al. (1988) presented a 2-component model for the BLR that consisted of separate emission regions for the high-ionization lines (HILs), e.g Lyα, C IV, and He II,

and low-ionization lines (LILs), e.g the Balmer lines and Fe II lines. The HILs were emitted by low pressure optically thin clouds illuminated by a soft continuum, and the LILs were formed in a high pressure optically thick medium, possibly that of an accretion disc, illuminated by a harder X-ray continuum; see also, for example, Cassidy & Raine (1997).

Increasingly sophisticated photoionization models of the BLR have indicated a number of potential problems that plague all continuum and emission-line variability studies. Specifically, anisotropic continuum emission, non-linear emission-line responses and the unknown shape and variability amplitude of the ionizing continuum that can introduce uncertainties into the re-constructed transfer functions.

The importance of anisotropic line emission was highlighted by Ferland et al. (1979) and Ferland et al. (1992). The recognition that BLR densities were higher than previously supposed, i.e. $\sim 10^{11}$ cm^{-3}, c.f. $\sim 10^{9}$ cm^{-3}, because of the distinctly separate semi-forbidden C III] emission region from other broad UV emission line regions, indicated the existence of very optically thick line-emitting clouds for most of the important emission lines. One of the consequences of this was line emission, e.g Lyα, being emitted from the irradiated face of the cloud, back towards the central source, thus appearing to explain the broad similarity of the UV emission-line profiles, given the anisotropic nature of most of the prominent emission lines. In principle the effects of anisotropic continuum emission can be accounted for during the re-construction of the BLR gas distribution, however, this obviously relies on *a priori* knowledge of the nature of the anisotropy, Goad et al. (1993), Goad et al. (1994), and Goad & Wanders (1996).

A non-linear emission-line response can also significantly alter the shape of the transfer function, Goad et al. (1995). For an ensemble of clouds of varying density and column density the emission lines are optimally emitted (Baldwin (1995)) at a given radial distance

from the central source, dependent on the line emissivity and therefore the incident ionizing continuum (or ionization parameter U, eqn. 1.7). Following the example of Netzer & Peterson (1997), the C IV emission-line response to continuum variations is only linear if most of the carbon is C III or C IV. If CV becomes the dominant species, on account of an increase in the ionization level of the gas, the C IV line emissivity decreases markedly– the line thermalizes. Other metal lines exhibit a similar behaviour, except the 'photon counting' ' Lyα line. The changing response of Lyα directly reflects the variation in number of ionizing photons, except for low-column density regions that become optically thin, and high-column density regions where subtle radiative transfer effects, e.g line trapping or collisional suppression, can alter the line optical depth (Ferland et al. (1992)). Hence, any attempts at re-constructing transfer functions should also consider the effects of non-linear emission line responses, via the use of detailed photoionization calculations.

1.9.4 Measurement of the BLR radius

Typically, the BLR radius is measured via a cross-correlation analysis of the continuum and emission-line light curves, §1.8. The AGN Watch datasets generally show UV and optical emission-line variations correlated and delayed with respect to continuum variations. The fractional amplitude of variations, corrected for the measurement errors, relative to the mean flux is typically $\sim$ 30-50% in the UV and $\sim$ 10-30% in the optical on time-scales of months for Seyfert 1 galaxies. The time delays for different emission lines reveal radially stratified ionization structures on scales of $\sim 2-20$ light days, e.g. N V and He II have lags of 1-2 days, Lyα and C IV lags are 7-12 days, and Hβ has a lag of about 11-20 days (lags quoted are for NGC 5548, Korista et al. (1995)). Hence, the HILs respond to continuum variations with shorter time delays than the LILs.

Furthermore, the measured time delays of emission lines is a function of the continuum

event duration and/or the sampling characteristics of the dataset (Netzer & Maoz (1990) and Peterson et al. (1994)), e.g. the Hβ lag for NGC 5548 was measured to be $\sim$ 11 days for the 1993 campaign, c.f. $\sim$ 18-19 days for the 1989-92 campaigns. This implies the BLR is geometrically thick, i.e. the inner radius is about 10% or less of the outer radius.

The direct measurement of the BLR radius was an order of magnitude smaller than that predicted by early photoionization studies, i.e. $\sim$ 10 days as opposed to $\sim$ 100 days. However, this discrepancy appears to be resolved by the observed BLR radial ionization stratification.

1.9.5 The one and two-dimensional transfer functions

A unique and stable solution to the integral equation (eqn. 1.2 or 1.3) requires large quantities of high quality data, e.g $\sim$ 1-2% errors on flux measurements with temporal resolutions of $\leq$ 1 day sustained over a baseline of several weeks to months. This is complicated by the inherent irregular sampling and mixed quality of astronomical observations, and has led to the development of a number of techniques (superior to that of Fourier deconvolution for this problem) aimed at recovering the transfer function in a reliable fashion. These include the maximum entropy method (MEM) of Horne (1994), regularized linear inversion method of Krolik (1994), and the SOLA algorithm of Pijpers (1994).

Attempts at re-constructing the one-dimensional transfer function, defined by eqn. 1.3, have been made for a number of sources, including NGC 5548 (Horne et al. (1991), Krolik et al. (1991), Peterson (1994), and Wanders & Horne (1994)), NGC 4151 (Maoz et al. (1991)), and NGC 3227 (Winge et al. (1995)). Typically, no clear structure is evident in $\Psi(\tau)$. However, there is evidence for a deficit of line response at zero time delays. Ferland et al. (1992) and O'Brien et al. (1994) attribute this to anisotropic line emission, with the emission–line flux directed back towards the central source through the illuminated face

of the optically thick cloud. Sparke (1993) argues for negative emission-line responses (i.e. the line responsivity decreases with increasing continuum level), based on the narrowness of the line ACF compared to the continuum ACF and the steepness of the CCFs close to zero lag (which in principle can account for a deficit of line response at zero time delays) and finally, it is possible the lack of line response at zero delays is a numerical artifact, since, for example, MEM solutions exist that do not show such a line response deficit (Peterson et al. (1993) and Horne (1994)).

The full recovery of $\Psi(v, \tau)$ has been attempted for NGC 4151 by Ulrich & Horne (1996) and NGC 5548 by Wanders et al. (1995) and Done & Krolik (1996). These authors used the C IV emission line response to continuum variations to show that the kinematic structure of the C IV emission region is not dominated by radial gas motions, as evidenced by the similarity of the blue-shifted and red-shifted response of the emission line. There may be weak evidence for a possible in-falling kinematic component, given the slightly different response times between the blue and red side of the line profile, but the results are ambiguous.

The difficulties that persist in comparing the 'observed' transfer functions with the model predictions is exacerbated by the broad similarity of the predictions of different models. A similar but distinct problem is highlighted by Goad & Wanders (1996). These authors point out, emission from an accretion disc surface, biconical outflow, and a spherical distribution of clouds moving along randomly inclined Keplerian orbits and illuminated by a variable anisotropic continuum source all produce characteristic double-peaked profile signatures observed in small sample of AGN (Eracleous & Halpern (1994)).

1.9.6 Black Hole Masses

A crude determination of the black hole mass can be made under the assumption of virial motions, see chapter 3. The simple method proceeds to balance the gravitational force with the centrifugal force, and yields $M \propto V^2\tau$; where M is the mass of the putative black hole, V is the velocity of the line emitting material, and τ is the 'lag' measurement of the line, §3.4.2. The time delay of the emission line is typically given by the centroid of the CCF, and the velocity of the gaseous material by the FWHM of the velocity profile of the line. We note in §3.4.2 that, for NGC 7469, the velocity of the BLR gas is about 30-40% larger, as measured from the FWHM of the mean line profiles, than that determined from the FWHM of the rms line profiles. We strongly advocate the measurement of the velocity of the BLR gas from the rms profiles, since the 'lag' (τ) determines the radial location of the variable component of the emission-lines.

The assumption of virial motions of the BLR gas is not experimentally proven, and the large systematic uncertainty introduced by assuming a given geometry and velocity field for the gas prohibits a mass determination, via this simple method, to better than an order of magnitude. Koratkar & Gaskell (1991) derived the mass of the central object in 10 AGNs in a consistent manner. The central sources were found to have masses of about $10^{7-8}M_{\odot}$. However, their mass estimates were based on the FWHM as measured from a mean spectrum not an rms spectrum, §3.4.2. As far as we are aware a similar consistent study of a sample of AGN with mass estimates derived from the rms profile has not been done. We may expect the mass estimates to be systematically smaller, although this does not have to be the case.

A related avenue of research pertains to attempts at confirming the naive prediction of photoionization studies, namely that the ionization parameter is approximately independent of the luminosity of the AGN, given the remarkable similarity of AGN spectra over

many orders of magnitude in luminosity. It then follows from eqn. 1.7, that the radius of the BLR r scales with the source luminosity as, $r \propto L^{1/2}$. A relationship of this type would indicate that the underlying physical processes governing high and comparatively low-luminosity AGN are similar.

Peterson (1993) and references therein show that the above relationship agrees approximately with the observational data of a small biased sample of AGN, primarily low-medium luminosity Seyfert 1 galaxies. Kaspi et al. (1996a) confirms the trend of higher luminosity sources having larger broad line regions by measuring r for a number of PG quasars, and is likely to extend these results in the near future to include more objects. The next few years will see further progress in the confirmation of the $r \propto L^{1/2}$ relationship, and the further development of mass-luminosity relationships for AGNs and their implications, e.g Dibai (1981) and Laor (1998).

1.9.7 The Nature of AGN Continuum Variations

For all AGN Watch campaigns to-date, excluding NGC 7469 from the discussion (see §3), no significant phase difference has been detected between the variations at UV and optical wavelengths. The optical variations lagged those at UV wavelengths by 2 ± 2 days for NGC 5548, 1 ± 4 days for NGC 3783, < 0.15 day in NGC 4151, $<$ 1–2 days for Fairall 9, and 5 ± 5 days for 3C 390.3.

These results have profound implications for the nature of the continuum emission, and hence the central engine of AGN. Given the standard paradigm of AGN, §1.4, the UV and optical continuum radiation is thought to arise in distinct regions of a classical accretion disc, Shakura & Sunyaev (1973). The mechanisms thought responsible for the continuum variations, e.g. thermal and dynamical disc instabilities, are believed to propagate through the disc at speeds of $\sim 10 - 1000$ km s^{-1}, and predict time delays between the different

continuum regions of $\sim$ hundreds of days-years, which are not observed. The disc models may be rescued, however, by invoking the reprocessing of X-rays to co-ordinate continuum variations at different radii in the disc (Krolik et al. (1991), Collin-Souffrin (1991), and Rokaki et al. (1992)).

Compelling evidence for the disc reprocessing scenario is given by the equivalent width of Fe Kα at 6.4 keV and the strength of the Compton reflection observed at > 10 keV, that suggest the majority of X-rays generated by an isotropic source must be reprocessed by relatively cold $< 10^6$ K optically thick gas, possibly that of an accretion disc (Pounds et al. (1990), and George & Fabian (1991)). Disc reprocessing models of, for example, Collin-Souffrin (1991), Nandra et al. (1991), Haardt & Maraschi (1993), and Rokaki et al. (1993) provide attractive explanations for the approximate simultaneity between medium energy X-rays and UV/optical variations of NGC 4151 (Perola et al. (1986)) and NGC 5548 (Clavel et al. (1992)), on time-scales of weeks to months.

Moreover, Haardt & Maraschi (1993) propose a model with magnetic flaring taking place in a hot corona surrounding the accretion disc, and X-ray emission produced via inverse Compton scattering of emission within the corona. The flaring activity, variations in the optical depth of the corona and its patchiness determine the variability time-scales, explain the shape of the medium energy X-ray spectrum, the Compton reflection and Fe Kα emission components, the close correlation of variations at different wavelengths, and the fraction of reprocessed emission. An important test of all reprocessing models will concern the energy budget of the variable emission components, Ulrich et al. (1997) and Nandra et al. (1998). That is, simply, does the energy of the harder wave-bands exceed that of the lower energy wave-bands?

The exact nature of the relationship between the continuum variations at different wavelengths remains unclear, and is complicated by its likely dependence on variability

time-scale and/or monitoring duration. For the AGN Watch campaigns of the past decade the UV and X-ray variations are typically correlated on time-scales of days, however see the NGC 7469 results of Nandra et al. (1998). On time-scales of years this correlation appears to break down, e.g. NGC 4151 (Warwick et al. (1996)), NGC 5548, and Fairall 9, with larger amplitude UV variations than X-ray variations.

Clavel et al. (1989) shows that for Fairall 9 the IR 2.1 μm variations are correlated and delayed by about 400 days with respect to variations at UV/optical wavelengths. Similar IR delays are reported by Glass (1992) for NGC 3783, and Baribaud et al. (1992) for NGC 1566. It is widely believed, Barvainis (1987) and references therein, that the IR emission is reprocessed UV/optical emission from dust grains at close to their sublimation temperature of about 1500 K.

A very important caveat dictates that any relationship between the different continuum bands is considerably complicated by the possible differing degrees of anisotropic emission of different emission components. Ulrich et al. (1997) states that any anisotropy in the X-ray comptonized emission could only account for about a factor of 2-3 deficit in any UV/X-ray flux ratio.

1.10 Summary of Thesis

Chapters 2 and 3 present results of an intensive two-month campaign of ground-based spectrophotometric monitoring of the Seyfert 1 galaxy NGC 7469, with a temporal resolution ≤ 1 day (Collier et al. (1998)). This campaign was part of the co-ordinated International AGN Watch multi-wavelength monitoring campaign on NGC 7469, undertaken during June-July 1996.

Using the UV results from the same campaign (Wanders et al. (1997)) we investigate and confirm the radial ionization structure of the BLR, with the HILs responding with

smaller time delays than the LILs, by measuring the first moment of the one-dimensional transfer function via a cross-correlation analysis, §1.8 and §3.3.1. The Hβ line lags the 1315Å continuum variations by about 5 days, c.f. Lyα line lag of 2-3 days. We estimate the mass of the purported black hole to be $M_{\rm NGC\ 7469} \approx 10^{6-7} M_{\odot}$, and given the measured compact BLR size, suggest the existence of a deep gravitational potential similar to that of a black hole, §3.4.2. Moreover, following the reports of small wavelength-dependent time delays in the UV spectra, we investigate the reality of wavelength-dependent time delays in the UV/optical continuum. We find evidence for statistically significant wavelength-dependent continuum time delays, with the optical variations lagging those at UV wavelength by about 1-2 days, §3.3.3. We demonstrate that the wavelength-dependence of the continuum time delays is consistent with the prediction $\tau \propto \lambda^{4/3}$ of a classical accretion disc, §3.4.1. The evidence strongly supports the notion of an accretion disc structure in NGC 7469, and may represent the indirect detection of an accretion disc in this system.

Chapter 4 discusses how the observation of wavelength-dependent time delays in other AGN can be used to test the standard black-hole accretion disc paradigm of AGN, by tracing the radial temperature profile of the gaseous material surrounding the purported black hole, §4.3. The method affords the opportunity to provide, perhaps, the 'smoking gun' evidence of accretion disc structures in different types of active galaxies. Moreover, we show that by combining the wavelength-dependent time delay measurements with an estimate of the nuclear spectral energy distribution one can determine a redshift-independent luminosity distance to the AGN, and therefore estimate the Hubble constant. We apply our method to data from the NGC 7469 campaign and estimate the Hubble constant to be $H_0 = 38 \pm 7\ {\rm km\,s^{-1}\,Mpc^{-1}}$. Analysis of the observed variable spectrum and wavelength-dependent time delays, §4, constitutes a novel tool for using AGNs as 'standard candles' to measure cosmological parameters, e.g. the Hubble constant H_0 and deceleration parameter

q_0. A glimpse of the AGN cosmological perspective is thus presented in §4.2.

In chapter 5 we determine the shape of the UV/optical variable spectral component for a small sample of AGN. This study was motivated by the aforesaid evidence for an accretion disc in NGC 7469, and the possibility of similar disc-like structures in other AGN. By analyzing a subset of results from the majority of AGN Watch monitoring datasets we present suggestive evidence for an intrinsic UV/optical variable nuclear flux distribution that is consistent with the prediction of a classical thin accretion disc (§5.5), namely $f_\nu \propto \lambda^{-1/3}$. Given this intrinsic variable nuclear flux distribution we estimate the resulting range of temperature structures present in, primarily, Seyfert 1 galaxies, before estimating the expected wavelength-dependence of any UV/optical continuum time delays. This allows us to predict UV/optical continuum time delays for our sample of AGN, and has implications for the observability of wavelength–dependent time delays.

Finally, we end the thesis by summarizing its main conclusions. We also discuss, briefly, possible future directions for work related to this thesis.

Chapter 2

Observations, Data Reduction and Intercalibration Procedures

2.1 Summary

This chapter is based on the paper **Collier et al., "Steps Toward Determination of the Size and Structure of the Broad Line Region in Active Galactic Nuclei.XIV.Intensive Optical Spectrophotometric Observations of NGC 7469", ApJ, 500, 162, 1998.** The paper presents the results of an intensive 2-month campaign of ground-based monitoring of the Seyfert I galaxy NGC 7469, with a temporal resolution of ≤ 1 day. Here we describe the observations undertaken, the methods of data reduction employed, and the steps taken to homogenize datasets taken by different observatories.

2.2 Overview of Observations

A 2 month campaign of continuous multi-wavelength monitoring was undertaken during the final episode of observations with the IUE satellite (Wanders et al. inc *Collier, S.*, 1997), in parallel with observations by the Hubble Space Telescope (HST) (Welsh et al. (1998); Kriss et al. (1998)), Rossi X-ray Timing Explorer (RXTE) (Nandra et al. (1998)),

and ground based telescopes (Collier et al. (1998)). A gyro failure on the IUE satellite in March 1996, just 2 months before the start of the originally proposed campaign on Mrk 335, forced a last minute target change. NGC 7469 was selected as a reliable variable Seyfert I galaxy that satisfied the constraints the gyro failure imposed.

NGC 7469 is an SBa Seyfert I galaxy (z=0.0164) that is gravitationally interacting with an irregular companion galaxy, IC 523, approximately 80" away (Salamanca et al. 1995 and references therein). NGC 7469 is also a starburst galaxy with a number of bright circumnuclear rings of star forming activity surrounding the nucleus, notably at about 1".5 and 8-10" from the nucleus (Genzel et al. (1995), Wilson et al. (1991), Bonatto & Pastoriza (1990) and references therein).

From 1996 June 2 to July 30, 54 nights of spectrophotometric observations of NGC 7469 were completed. I observed for 50 nights during this 2 month period, securing spectra on 42 nights with the Wise Observatory's 1.0m telescope and Faint Object Spectroscopic Camera (Kaspi et al. (1995)). A more complete description of the observations follows in §2.2.1.

Four other spectroscopic datasets were obtained by AGN Watch teams. Of these, two were judged suitable for intercalibration with the Wise dataset. The Ohio State University (OSU) group observed NGC 7469 on 8 nights during the period 1996 May 9 to July 9 with the 1.8m Perkins telescope and Bollen and Chivens spectrograph. The 4540-5700Å wavelength range was covered with a spectral resolution of $\sim$ 9Å. A 5" $\times$ 7".4 slit (extraction window geometry EWG) was used throughout the observations. At the Crimean Astrophysical Observatory (CAO), 19 observations were made during 1996 June 11 to October 16 at the Nasmyth focus of the 2.6m Shajn telescope. The wavelength range was 4300-5594Å the spectral resolution $\sim$ 8Å. The 3" $\times$ 11" slit (EWG) was aligned at a PA of 90°.

2.2.1 Wise Observatory 1.0m Observations and Faint Object Spectroscopic Camera

The Florence and George Wise Observatory belongs to Tel Aviv University, Israel. It is situated on a plateau in the Negev desert (longitude 34° 45' 48" E, latitude 30° 35' 45" N, altitude 875m), about 5 km west of a small town Mitzpe Ramon.

The 1.0m telescope is a wide field Ritchey-Chretien reflector. I used the Faint Object Spectroscopic Camera (FOSC) with a Tektronics 1024 × 1024 pixel CCD to perform the observations. The FOSC allows multicolour imaging of a 17″ diameter field, and multi-mode spectroscopy.

A 600 line/mm grism (a grism is a prism with transmission gratings replicated onto its faces) gave a spectral resolution of $\sim$ 8Å over the wavelength range 4016-7841Å. The 10″× 16″.8 slit (EWG) was aligned at a PA of 26.7°, in order to observe the active nucleus simultaneously with the $V = 11$ magnitude comparison star $\sim 3'$ from NGC 7469 (star 2 of Penston et al. (1971)). This technique can achieve a relative spectrophotometric accuracy of about 1%, as discussed in §2.3.4 (see also Maoz et al. (1991)).

2.3 Data Reduction

The OSU and CAO datasets were reduced, by their owners, in a standard fashion, and internally flux calibrated using the [O III] emission lines as in previous AGN Watch optical projects (e.g. NGC 3783: Stirpe et al. (1994), NGC 4151: Kaspi et al. (1996a), and 3C 390.3: Dietrich et al. (1998)), discussed in §2.3.6. The method of intercalibrating the spectroscopic datasets was first used by Peterson et al. (1991). The physical justification for it is presented in detail in Peterson et al. (1995), and will be discussed in §2.3.6. We discuss below the reduction of the Wise dataset in more detail because this employed non-standard reduction procedures similar but not identical to those employed in previous Wise Observatory campaigns (Maoz et al. (1991), Maoz et al. (1991)). Maoz

and collaborators make use of the atypical Wise Observatory spectrograph slit length to observe a comparison star simultaneously with the program object. Excellent relative spectrophotometric accuracy, approaching 1%, is achieved by measuring the variations of the program object with respect to the supposed constant luminosity comparison star.

The CCD spectra were reduced with FIGARO, a general purpose data reduction package maintained by the STARLINK network. Additional software packages utilized in the reduction stages included PAMELA and MOLLY (Tom Marsh, Southampton). A plethora of data reduction 'cookbooks' detailing the procedures to reduce different types of observations are now available through the World Wide Web (WWW) (see http://star-www.rl.ac.uk/star/docs/sgp46.htx/node40.html). The primary steps we followed in reducing the spectroscopic observations were **de-biasing, flat-fielding, tracing, normal extraction, wavelength calibration, relative and absolute flux calibration.**

2.3.1 De-biasing and Flat Fielding the CCD Data Frames

The bias level is a constant offset applied to the CCD chip to ensure only positive numbers are attained during the analog-to-digital conversion processes (Mackay et al. (1986)). Typically, an average of 20 bias frames were used to subtract this bias level. Short 8 second exposures of the twilight sky were used to calibrate the spatial illumination pattern along the slit (that is the large scale sensitivity variation across the chip due to variations in the thickness of the CCD substrate, fringing patterns due to interference effects in the substrate (only a problem for thinned chips), and areas of reduced response due to dust or grease on the surface of the chip or on the chip window), while the incandescent lamp flats were used to calibrate the pixel-to-pixel sensitivity variations of the CCD detector. These latter two processes are collectively called *flat-fielding* the spectra and are arguably the most important steps in astronomical image processing. Noise models fitted to calibrated

data frames gave values for the rms readout noise (0.8 ADU) and gain (8.4 photons/ADU) of the CCD detector, and were used to establish error bars on each CCD pixel, and subsequently on the extracted spectra. A noise model is defined by

$$\sigma^2(X) = \sigma_0^2 + X/G, \tag{2.1}$$

where $\sigma^2(X)$ is the variance of the data numbers, σ_0 is the readout noise of the CCD measured in data numbers, X is the data number, and G is the gain of the CCD detector which is equal to the number of photons per data number or equivalently the number of counts per data number.

2.3.2 Tracing and Normal Extraction of Spectra

The active galaxy and comparison star spectra were 'traced' on the CCD frames with polynomial fits to compensate for optical distortions (e.g camera mis-alignment) and differential effects (Light is refracted as it passes through the earth's atmosphere. The degree of refraction is a function of the air mass traversed and the wavelength of light). Spectra were then *normally* extracted by summing the counts in $16''.8$ extraction windows, after subtracting a sky background fit. This optimum-sized extraction window was determined empirically by trial and error. Using a larger window degraded the quality of the spectra by including pixels with negligible signal, while a smaller window compromised the photometric accuracy of the spectra by excluding significant amounts of galaxy signal.

2.3.3 Wavelength Calibration

Arc-lamp (HeAr) exposures taken approximately every 20 minutes supplied an accurate wavelength scale, calibrating the small wavelength shifts caused by flexure in the spectrograph. The pixel centroids of the lines are measured using Gaussian correlation, then a polynomial function is fitted to the known wavelengths of the lines and their associ-

ated pixel position to determine the wavelength scale. Additional care to omit blended lines and identify enough arc lines through the entire wavelength range is required. This proved problematic due to the low resolution nature of the data and consequent blending of closely spaced arc lines, the probable leakage of light into the arc lamp casing (particularly noticeable in the red) and the lack of strong arc lines in the blue end of the HeAr spectra.

Indeed prior to publication of the paper Collier et al. (1998) Dr William Welsh kindly drew attention to a problem with the wavelength calibration. He noted the redshift of NGC 7469 ($z = 0.0164$) was a function of the emission line used to calculate it ($\Delta\lambda/\lambda = z$), e.g; Using the H$\gamma$ line gave $z = 0.0046$, whereas the [N II] line gave $z = 0.0178$. This was because the dispersion function, i.e the polynomial fit that calibrates the wavelength scale, was too smooth and did not account sufficiently for the higher-order non-linearity at the blue edge of the spectra. What went wrong? A combination of things, including; my inexperience, absence of suitable arc lines short-ward of 5000Å required to track the non-linearities of the wavelength scale in this region, and, possibly, a mis-identification of an arc line in the same region. Prior to this discovery we had fitted a 3rd order polynomial to the manually identified arc lines. The rms of the fit was 0.6Å over a wavelength range of 3900-7839Å with a mean dispersion of 3.8Å pixel^{-1}. The corrected dispersion function was a 6th-order polynomial, with an rms of 1.5Å over a wavelength range of 4016-7841Å and an identical mean dispersion of 3.8Å pixel^{-1}. In future experiments it would be desirable to use a more suitable arc lamp, e.g. Th-Ar, that has strong arc lines throughout the wavelength range to be calibrated or use multiple arc lamps for the calibration. Fig. 2.1 presents the corrected dispersion function, while Fig. 2.2 digresses to compare the mean spectrum of the campaign before and after correction of the wavelength calibration problem.

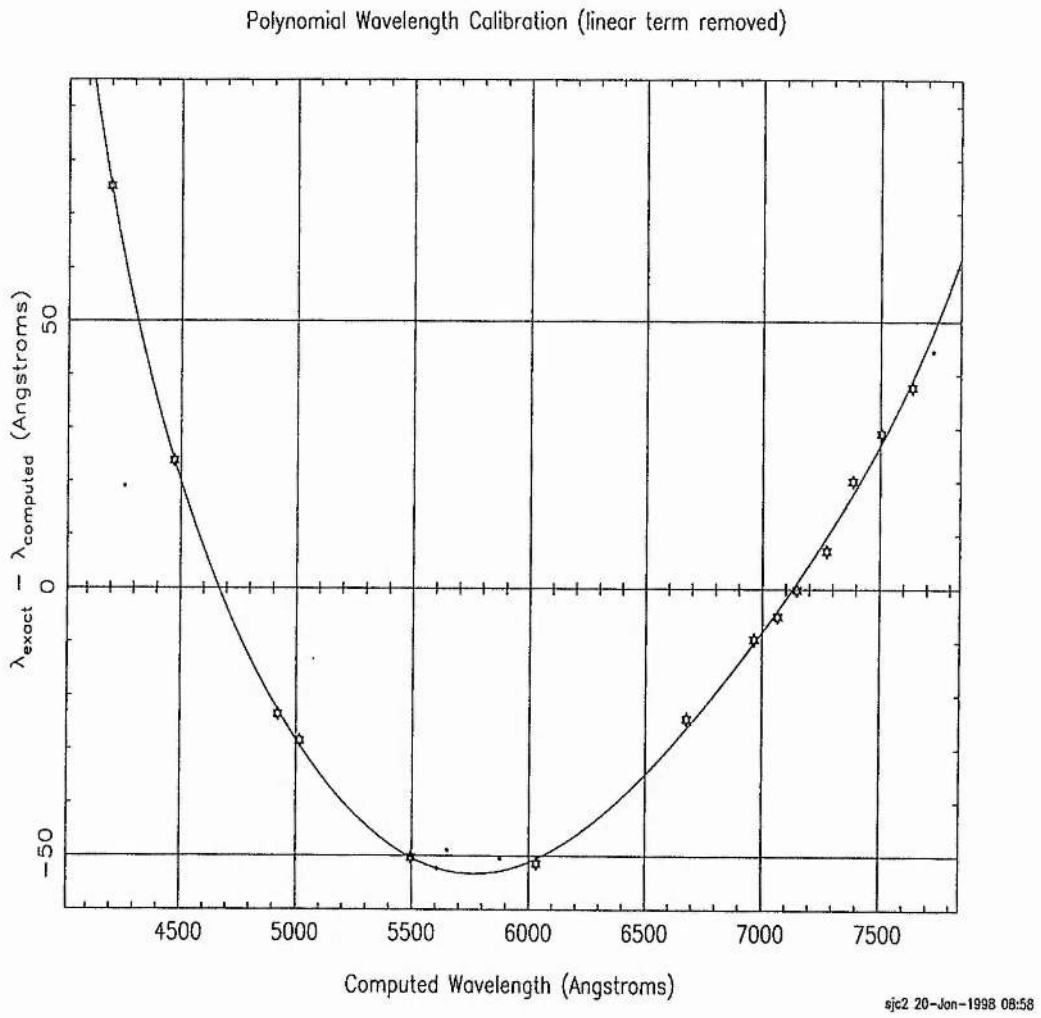

Figure 2.1: The fitted polynomial dispersion function used to apply wavelength calibration to the spectra (see text for details). The mean dispersion is 3.8 Å pixel^{-1}. Note the linear term has been removed, that is the polynomial term that indicates that the pixel number increases with increasing wavelength, to illustrate the non-linear distortions.

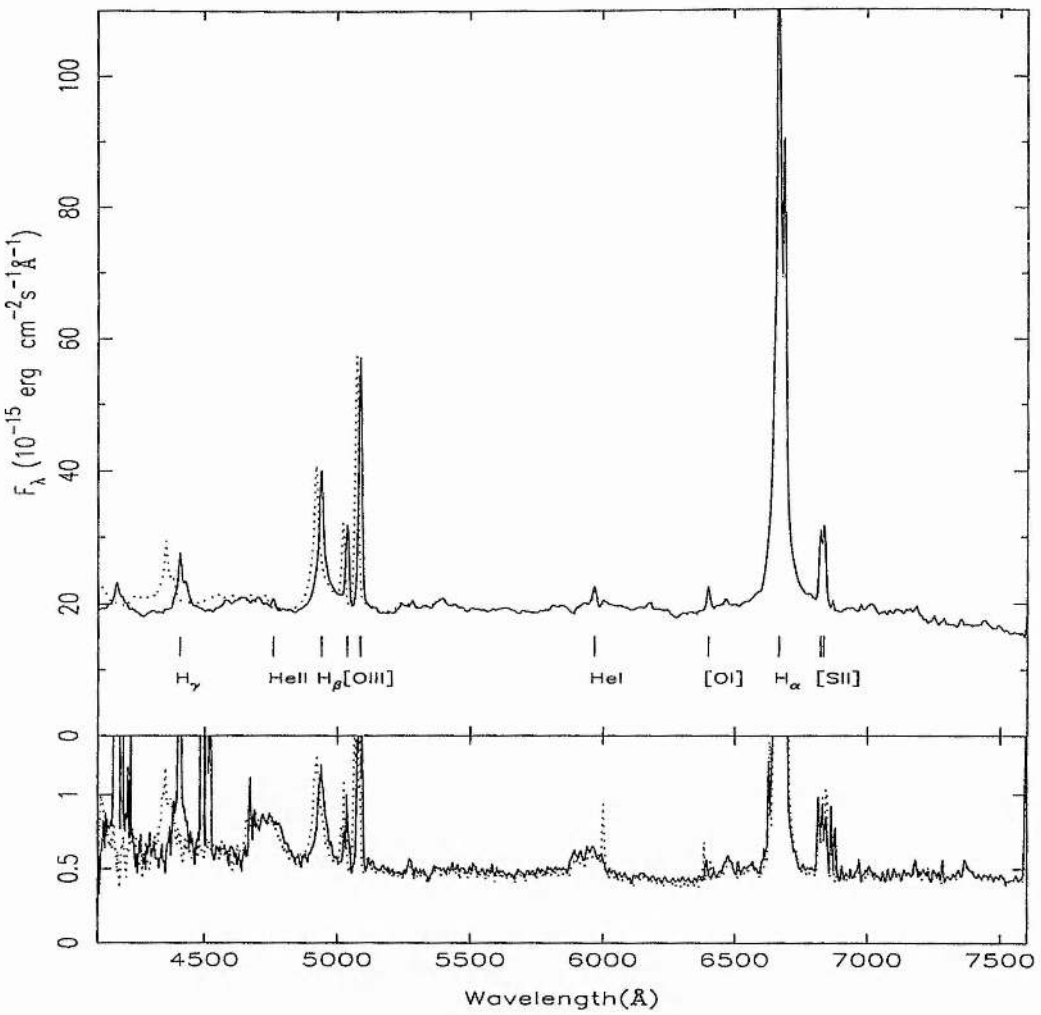

Figure 2.2: Top panel: Comparison of the mean spectra of NGC 7469; the solid line denotes the mean spectrum using the corrected dispersion function, and the dotted line denotes the mean spectrum with the old dispersion function. Note the anomalous stretching in the wavelength scale in the old mean spectrum that makes the blue region too blue. Bottom panel: A similar comparison of the RMS spectra of NGC 7469, showing the spectra of the variable component. The solid and dotted lines represent the use of the corrected and old dispersion functions respectively. Note that the two RMS spectra are approximately consistent, neglecting the stretch in the wavelength scale, confirming that the variable component of the spectra is unaffected by this systematic error in the wavelength calibration

2.3.4 Relative and Absolute Flux Calibration

Airmass corrections were applied to account for continuous extinction using an empirically derived estimate for the extinction as a function of wavelength for the Wise Observatory observing site. The strongly wavelength-dependent continuous extinction, $a_c \propto \lambda^4$, is due to Rayleigh scattering of photons by molecules in the earth's atmosphere. Absolute flux calibration was based on observations of BD+28°4211 observed on photometric nights. The essence of the procedure is the comparison of the observed counts with the tabulated fluxes to correct for the large scale sensitivity variations and the spectral response. This was achieved by fitting a spline with 17 knots to the ratio of the counts/flux continuum standard star observations, which in turn permitted the flux calibration of all the spectra.

Atmospheric absorption bands were removed from the AGN spectra with a first order "B-star" calibration technique (Wade & Horne (1988)). Each comparison star spectrum was divided by a spline fit to normalise its continuum, and all regions outside the telluric absorption bands were set equal to unity. Dividing the AGN spectra by this telluric band spectrum, Fig. 2.3, removed the atmospheric absorption bands.

Relative flux calibration was then achieved by calibrating a time- and wavelength-dependent slit loss. An average comparison spectrum was composed from 5 observations on July 8, a photometric night. All comparison star spectra were divided by this photometric spectrum, and then third-order polynomials were fitted to the ratio spectra, masking any residual absorption features. The polynomial fits represent the wavelength-dependent light losses affecting each spectrum, assuming that the average spectrum is "photometric" and that the nucleus and comparison star experience the same slit losses. The final AGN spectra were produced by dividing by the corresponding polynomial fits, Fig. 2.4. After performing these slit loss corrections, the comparison star spectra yielded a constant flux to within $\sim$ 1%. This rms scatter is primarily attributable to the uncertainty in fitting

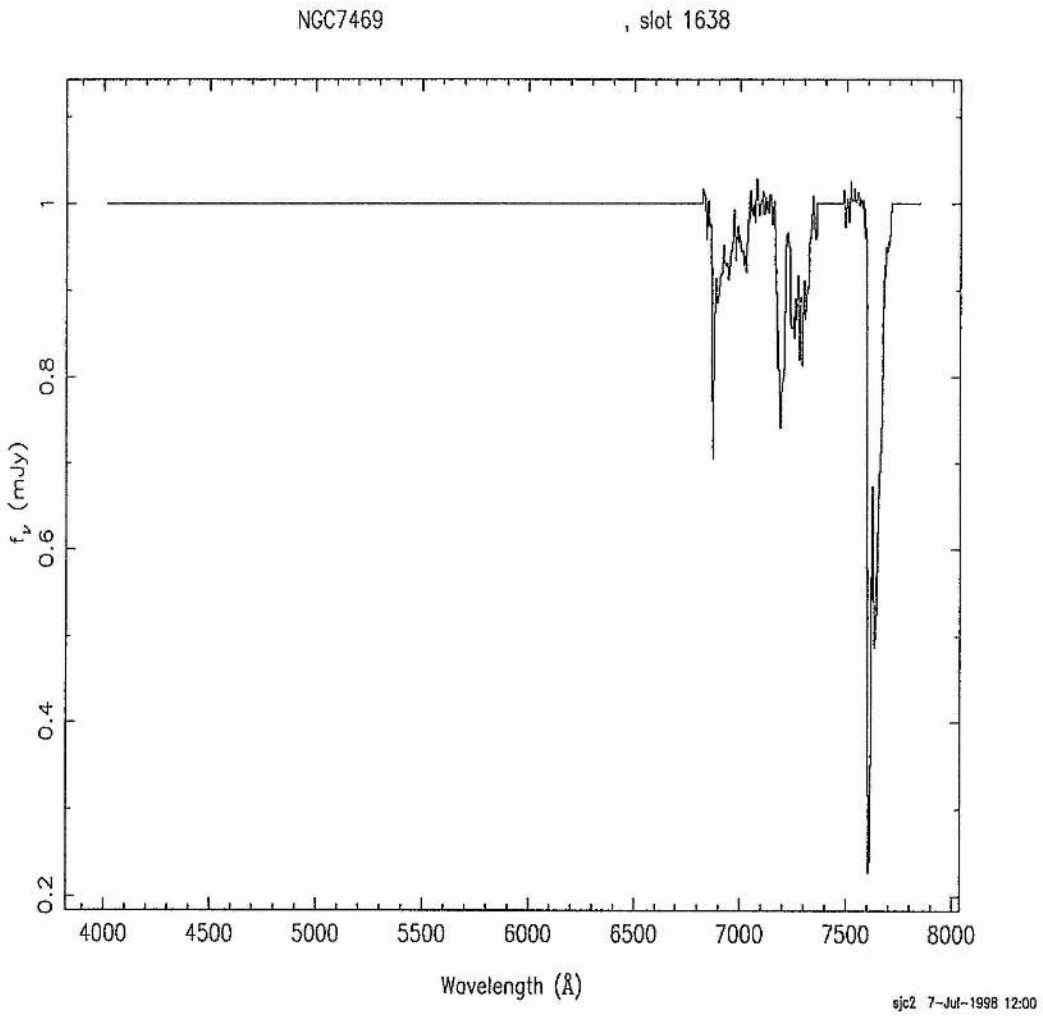

Figure 2.3: An illustrative example of a telluric band spectrum taken on July 8, 1996. The absorption bands long-ward of 6800 Å are due to specific vibrational and rotational transitions of H_2O molecules.

the low order polynomial and represents a lower limit to the uncertainty in the relative flux calibration.

2.3.5 Extracting the Light Curves

Final light curves were computed by summing the fluxes in a given wavelength region. For emission-line light curves, the subtracted continuum was defined as a straight line fitted to continuum bands on either side of the line (defined in §3.2.1). Then when multiple spectra were obtained on a given night, a weighted average with $1/\sigma^2$ weights was computed, where σ is the flux error associated with each pixel. A 1% calibration error was added in quadrature to the error in the weighted mean, to give the final error bars on each measurement. In future it may be best to compute the unweighted nightly average of the fluxes, since a weighted average biases the final flux measurement to low flux states, since when the flux is high, σ(flux) is larger (Mike Goad, private communication). This comment applies equally to the computation of the mean spectrum for similar reasons.

2.3.6 Intercalibration

A more extensive temporal coverage was achieved by intercalibrating the additional datasets with the reference dataset taken at the Wise Observatory. The low amplitude of the variability seen in the Wise dataset placed heightened emphasis on high quality homogeneous datasets overlapping with the intensive monitoring at Wise Observatory. We required the calibrated fluxes to agree to $\leq 3\%$ with the Wise fluxes. Two datasets met these criteria, the Ohio State University dataset (8 spectra), and the CAO dataset (19 spectra).

The intercalibration procedure assumes that the flux emitted in the narrow [O III] emission lines is constant on the time-scales of interest, because these low-density lines have a longer recombination time t_{rec} (electron densities $n_e \approx 10^3$ cm^{-3}, $t_{rec} \sim 100$ years) and form at much greater distances from the central source (typically at distances

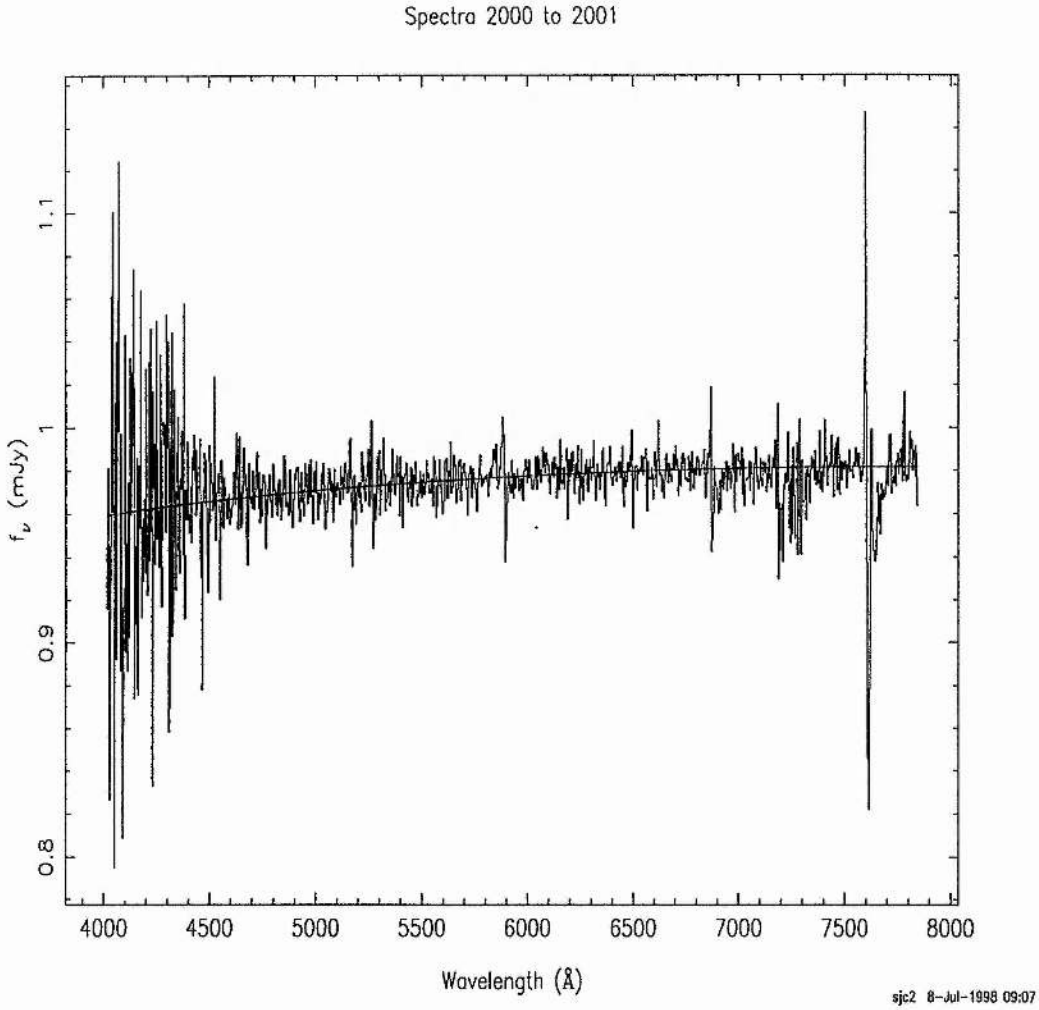

Figure 2.4: An illustrative 3rd order polynomial slit-loss correction function is fitted to the July 8, 1996, spectrum. The blue end of the spectrum is noticeably noisier due to low quantum efficiency of the CCD in this spectral region.

of 100 – 1000 light years) than the broad emission lines. The [O III] emission line flux was computed for each spectrum of the reference dataset by summing the flux in the 5025–5103Å region, after subtracting a straight line continuum connecting 5000–5020Å to 5110–5130Å. This is not an ideal method of measurement for the [O III] flux since the [O III] emission lines sit upon the broad red wing of Hβ, and are also contaminated by blends of Fe II emission. However, this method allows highly desirable unambiguous and automated measurements of the [O III] flux. The 194 Wise spectra gave a mean [O III] flux of $(7.5 \pm 0.2) \times 10^{-13}$ergs s^{-1} cm^{-2}. The rms scatter of $\sim 2.7\%$ indicates the level of stability of the narrow [O III] emission lines, Fig. 2.5

To validate the accuracy of the relative flux calibration, we used the van Groningen & Wanders (1992) scaling algorithm to scale the [O III] flux of the spectroscopic Wise dataset to a constant value (i.e without the spectrophotometric calibrations). This method uses a template spectrum, which we obtained from a photometric, high signal to noise spectrum. The algorithm subtracts the (scaled, shifted, blurred) template spectrum, then fits a low order function to a given wavelength region, minimizing the χ^2 of the residuals. Nightly mean [O III] fluxes were calculated, and their rms scatter of $\sim 2.7\%$ was consistent with that found from the relative flux calibration based on the comparison star. The 27 additional spectra from the OSU & CAO datasets were scaled to a constant [O III] flux, using the van Groningen & Wanders (1992) algorithm, with the mean of the 194 Wise spectra as the template spectrum.

Subsequent stages of intercalibration involved correcting for differences in the light loss suffered by various AGN components due to aperture size differences among the datasets. The importance of aperture effects for the NLR is discussed by Collin-Souffrin (1980), Peterson & Collins (1983), and Wanders et al. (1992). Peterson et al. (1995) extended the aforementioned work, emphasizing that the use of small spectrograph apertures ($2'' \times 10''$)

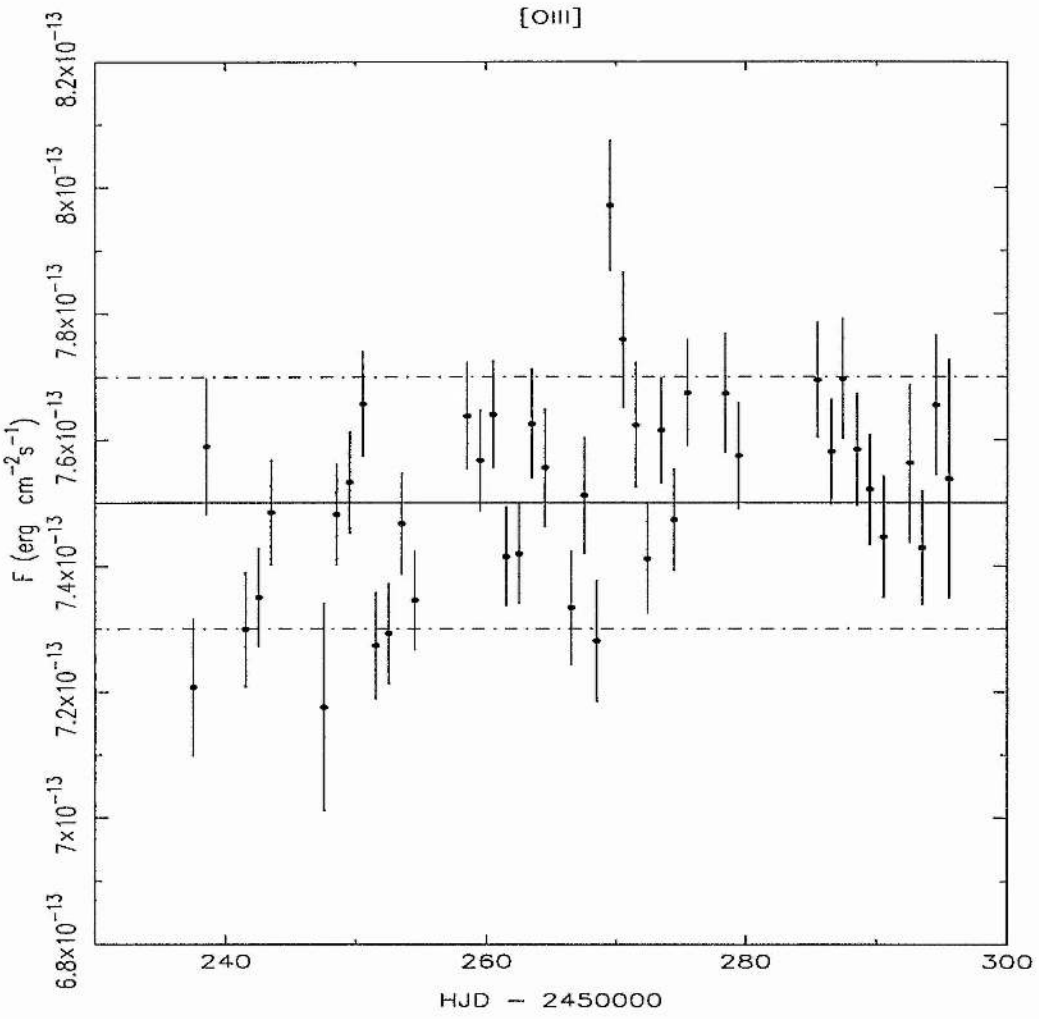

Figure 2.5: The [O III] flux light curve for the intensive monitoring period, June 2 to July 31, 1996. The mean [O III] flux ($(7.5\pm0.2)\times10^{-13}$ ergs s^{-1} cm^{-2}) and 1-σ error are denoted by the solid and dot-dashed-dotted lines respectively. The scatter in this plot indicates the level of stability of the narrow [O III] lines. We note the [O III] flux measurement is likely to be contaminated by the Hβ red wing and possibly the Fe II line complexes.

in variability studies were highly undesirable since they potentially led to large, 10-20%, photometric errors when using the constancy of the narrow emission lines as a means of flux calibration. This is because the Narrow Line Region (NLR) of Seyfert galaxies are often partially resolved and seeing fluctuations and mis-centering of sources in the slit can lead to variations in the amount of narrow line flux admitted into the aperture and hence to potential artificial correlated variations of the broad line and continuum fluxes.

An empirical intercalibration procedure, devised by Peterson et al. (1991), was used to correct for differences in the light loss suffered by various AGN components due to aperture size differences among the datasets. The Wise observations used a $10'' \times 16''.8$ slit and were found not to suffer large light losses during the monitoring period, as discussed in §2.3 and §3.4.1. As previously mentioned the Wise dataset was adopted as the reference dataset. A wavelength-independent point-source multiplicative correction factor accounts for apertures admitting different fractions of the point spread function and of the extended narrow line emission region. The point spread function describes the surface brightness distribution of both the broad emission lines and the nuclear continuum source. The point-source correction factor ϕ is defined by

$$F(H\beta) = \phi F(H\beta)^{\rm obs}, \tag{2.2}$$

where $F(H\beta)^{\rm obs}$ is the Hβ line flux measured from each spectrum of the [O III] scaled OSU and CAO datasets, and $F(H\beta)$ is the Wise Hβ flux from an epoch within ± 2 days of the $F(H\beta)^{\rm obs}$ epoch of measurement.

A wavelength-dependent additive correction corrects for apertures admitting different fractions of starlight from the host galaxy. This additive correction factor applies to continuum regions, and is a function of wavelength due to the wavelength dependence of the host galaxy starlight. This wavelength-dependent additive correction factor G is

defined by

$$F(\lambda)^{\rm contn} = \phi F(\lambda)^{\rm contn}_{\rm obs} - G, \tag{2.3}$$

where $F(\lambda)^{\rm contn}_{\rm obs}$ is the continuum flux measured from each spectrum of the [O III] scaled OSU and CAO datasets, and $F(\lambda)^{\rm contn}$ is the Wise continuum flux from an epoch within ± 2 days of the $F(\lambda)^{\rm contn}_{\rm obs}$ epoch of measurement.

The intercalibration constants ϕ and G were then determined for each spectrum of the OSU and CAO datasets, using the light curves extracted from the 4840–4890Å, 4900–5000Å and 5160–5220Å wavelength regions. Formal errors were assigned to the intercalibrated datasets based on the accuracy to which we could compute the correction factors previously described. In both cases the error-bars assigned were $\leq 2\%$, based on the dispersion of the computed intercalibration constants about their mean value for each individual dataset. At longer wavelengths intercalibration proved problematic due to the errors of the intercalibrated fluxes becoming comparable to the amplitude of variability observed.

Chapter 3

The Analysis and Results of the NGC 7469 Monitoring Campaign

3.1 Summary

As for chapter 2, this chapter is based on the paper **Collier et al., "Steps Toward Determination of the Size and Structure of the Broad Line Region in Active Galactic Nuclei.XIV.Intensive Optical Spectrophotometric Observations of NGC 7469", ApJ, 500, 162, 1998.** In §3.2 we discuss the mean and RMS spectra. In §3.2.1 and §3.2.2 we present the light curves and variability characteristics of the dataset. The cross-correlation analysis of both the emission lines and continuum time delays is discussed in §3.3. This section introduces the application of a 'quasi-bootstrap' technique to assess the uncertainties of measured time delays in AGN variability studies, and was used in Dietrich, M., et al. (*inc. Collier, S.*), ApJS, 115,185 (1998). Furthermore, it led to the development of a model-independent method of assessing the uncertainties of the measured time delays as presented by Peterson, B., M., Wanders, I., Horne, K., *Collier, S.*, Alexander, T., Kaspi, S., and Maoz, D., "*On Uncertainties in Cross-Correlation Lags and the Reality of Wavelength-dependent Continuum Lags in Active Galactic Nuclei*", PASP, 110, 660, 1998. In §3.4 we interpret our results as evidence for an accretion

disc in NGC 7469, we fit simplified models to the data to validate our claims, and present calculations for the mass and accretion rate of the purported black hole. We present the conclusions of this work in §3.5.

3.2 Mean and RMS spectra

The mean and root-mean-square (rms) of 194 spectra (the complete Wise dataset) are shown in Fig. 3.1. The rms spectrum characterises the variable component of the spectrum.

Salient features in the mean spectrum are broad Hγ, Hβ and Hα emission lines, observed at wavelengths of $\sim$ 4407Å, 4940Å and 6667Å. Broad He I λ5876 and He II λ4686 are observed as low contrast features. Forbidden narrow lines of [O III], [O I], and [S II] are observed at $\sim$ 5036Å, 5086Å, 6400Å, 6824Å and 6836Å respectively. Typical FWHMs are $\sim$ 2000 km s^{-1} for the broad lines and 500 km s^{-1} for the narrow lines. Broad band features from blended Fe II multiplets are observed at $\sim$ 4650Å and 5350Å. The mean spectrum declines in flux towards longer wavelengths. This may be a result of the relatively blue component of the starburst rings that surrounds NGC 7469 at radii of $\sim$ 8–10″ and $\sim$ 1″.5 (Salamanca et al. (1995)). The more rapid decline of continuum flux long-ward of 7200Å results from imperfect calibration of the sensitivity of the CCD detector.

The rms spectrum (lower panel of Fig. 3.1) confirms that low-amplitude line and continuum variability was detected during the intensive monitoring period. The continuum varies by $\sim$ 4% at both 4800Å and 7000Å. The broad He II λ4686 emission is not clearly visible in the mean spectrum due to blending with Fe II emission, but the rms spectrum reveals a broad peak with rms variations up to $\sim$ 5% of the corresponding mean flux. Imperfect wavelength calibration results in spurious peaks in the rms spectrum near each of the narrow lines, but this does not seriously affect the continuum and broad line features.

The host galaxy contribution was estimated in the following crude way: Two spectra

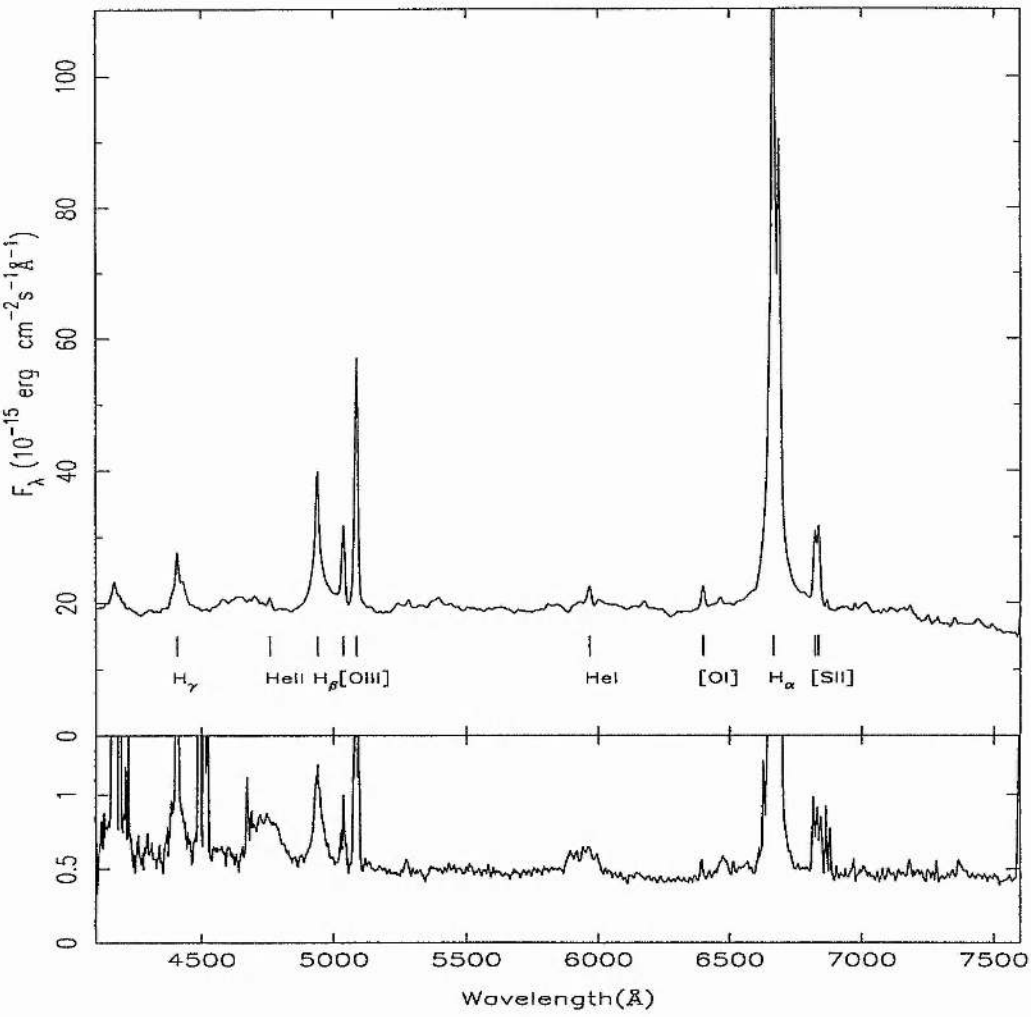

Figure 3.1: Top panel: Mean spectrum of NGC 7469. Bottom Panel: The rms spectrum of NGC 7469. Imperfect wavelength calibration results in spurious peaks near each of the narrow lines

were extracted from a high signal-to-noise data frame, with extraction windows of 16″.8 and 42″ respectively. Subtracting the smaller from the larger aperture spectrum led to an estimate of the host galaxy spectrum in two 10″ x 12″.6 apertures straddling the 10″ x 16″.8 window. We assume that the spectral shape of the host galaxy is the same in both apertures, but apply a scale factor (0.79) to account for the smaller solid angle, and higher surface brightness of the host galaxy in the 10″ x 16″.8 aperture. From this we estimate that the host galaxy contaminates the mean spectrum by $\sim 18\%$ or 3.7 ± 0.7 mJy at 5400Å. This compares favourably with an independent estimate of 3.2 ± 0.6 mJy, from the results presented by Malkan & Filippenko (1983).

However, our crude estimate for the host galaxy contribution is incorrect. We note it was only intended as a very crude estimate. This is because a) the assumption that the spectral shape of the host galaxy is the same in both apertures is not valid, since the starlight is mostly concentrated close to the nucleus (For example we do not include emission from the bright circumnuclear ring of starburst activity (a starburst is a region where intense star formation is occurring) $\sim$ 1″.5 from the nucleus), and b) no rigorous attempt to model the nuclear and galaxy point-spread-function (psf) was undertaken. Malkan & Filippenko (1983)'s measurement of the stellar contribution was based on ground-based images and high resolution spectra. The relative amount of light, in a given aperture, from the unresolved nucleus was measured from direct images. By comparing the observed equivalent width of stellar absorption lines with average values from a spectrum of an ordinary galaxy they determined the fraction of stellar light in the nuclear region, which in turn allowed the total optical non-stellar and stellar continuum fluxes to be estimated. Their measurements, through a $\sim$ 1″.6 $\times$ 3″.7 slit, did not allow for the contaminating contribution from the starburst ring 1″.5 from the nucleus. As the starburst ring emission is not due to a red giant stellar population, the absorption line measurements most

probably underestimate the stellar light contribution.

In contrast, the HST observations of NGC 7469 (Welsh et al. (1998)) were taken with a 0″.86 square aperture, and indicate that > 99.5% of the light is contained within 0″.5 of the nucleus. Their aperture contained negligible, if any, contaminating light from the host galaxy and starburst ring, contrary to the ground-based observations, and can be successfully used to estimate the spectrum of the host galaxy + starbursts by subtracting the mean HST PRISM spectrum from the mean ground-based optical spectrum. Welsh et al. (1998) show that the contribution of light from the host galaxy + starbursts in the ground-based spectra is about 50% at 4200Å and about 80% at 7400Å. These results agree with those presented by Bonatto & Pastoriza (1990) who estimate the stellar light contribution to be about 47% at 4200Å and 50% at 5300Å in an 8″ × 15″ aperture. Fig. 3.2 presents the mean optical, HST PRISM, and derived host galaxy + starbursts spectra (Fig. 3.2 kindly supplied by Dr William Welsh). Fig. 3.3 shows the percentage contamination of the mean optical spectrum by the host galaxy + starlight spectrum (Fig. 3.3 kindly supplied by Dr William Welsh).

3.2.1 Light Curves

Fig. 3.4 presents the 4840-4890Å continuum and Hβ light curves for the complete monitoring campaign, May 9 to Oct 17. Observed wavelengths and fluxes are used throughout, with no correction for the redshift ($z = 0.0164$) of the object. Emission-line light curves were constructed by summing the flux in a given wavelength region after subtracting a pseudo-continuum defined as a straight line fitted to the continuum about the wavelength region of interest. The light curves are tabulated in Table 3.1. Referring to Fig. 3.4, both light curves begin with an $\sim$ 18% decrease in flux over 12 days to a lower flux level, where $\sim$ 10% flux fluctuations occur on time-scales of $\sim$ 1 week during the 60-day intensive

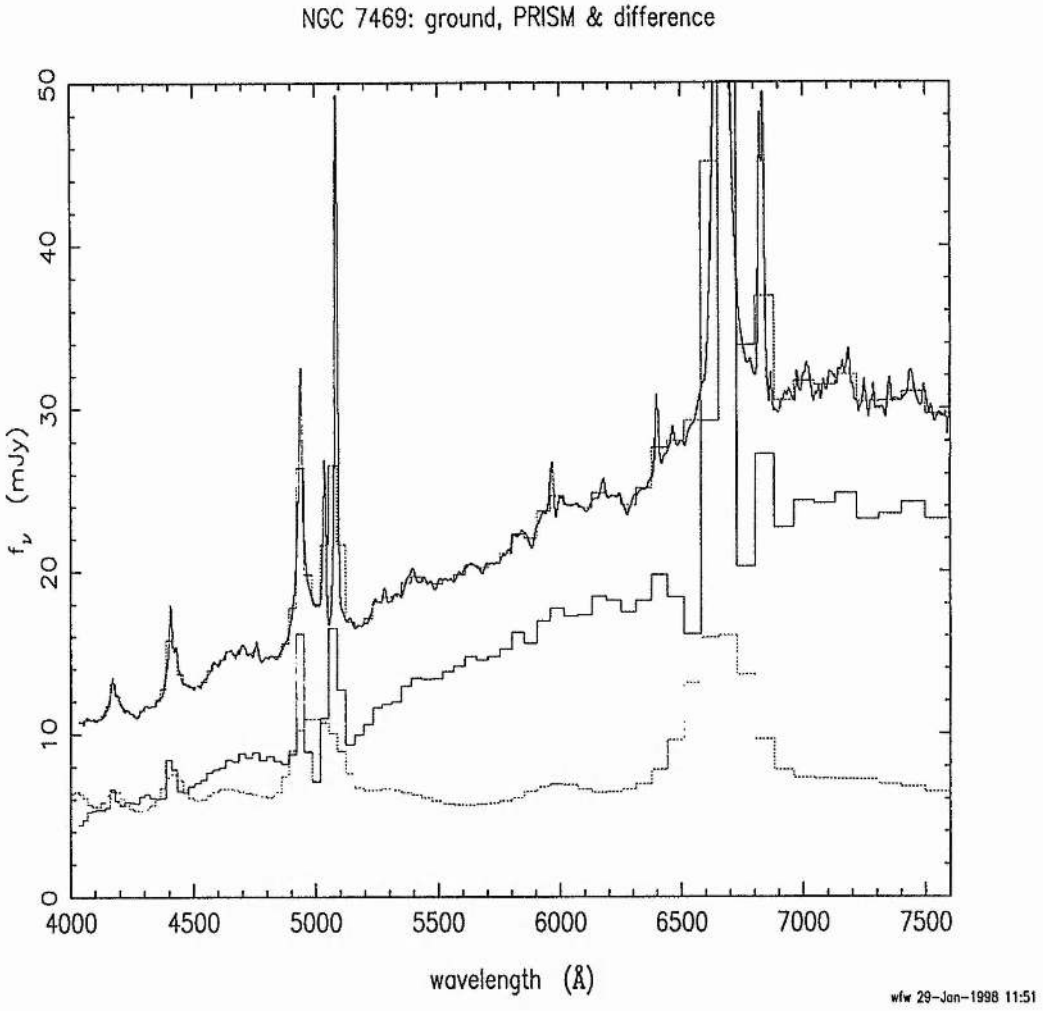

Figure 3.2: The upper spectrum is the mean optical spectrum, overlaid is the mean optical spectrum with identical binning to that of the HST PRISM spectrum. The lower spectrum is the HST PRISM spectrum (for details see Welsh et al. 1998). The middle spectrum is the difference spectrum, mean optical - HST PRISM, and is the host-galaxy + starburst spectrum. The host-galaxy + starburst spectrum is wavelength-dependent and dominates the mean optical spectrum at most wavelengths (Figure kindly supplied by Dr William Welsh).

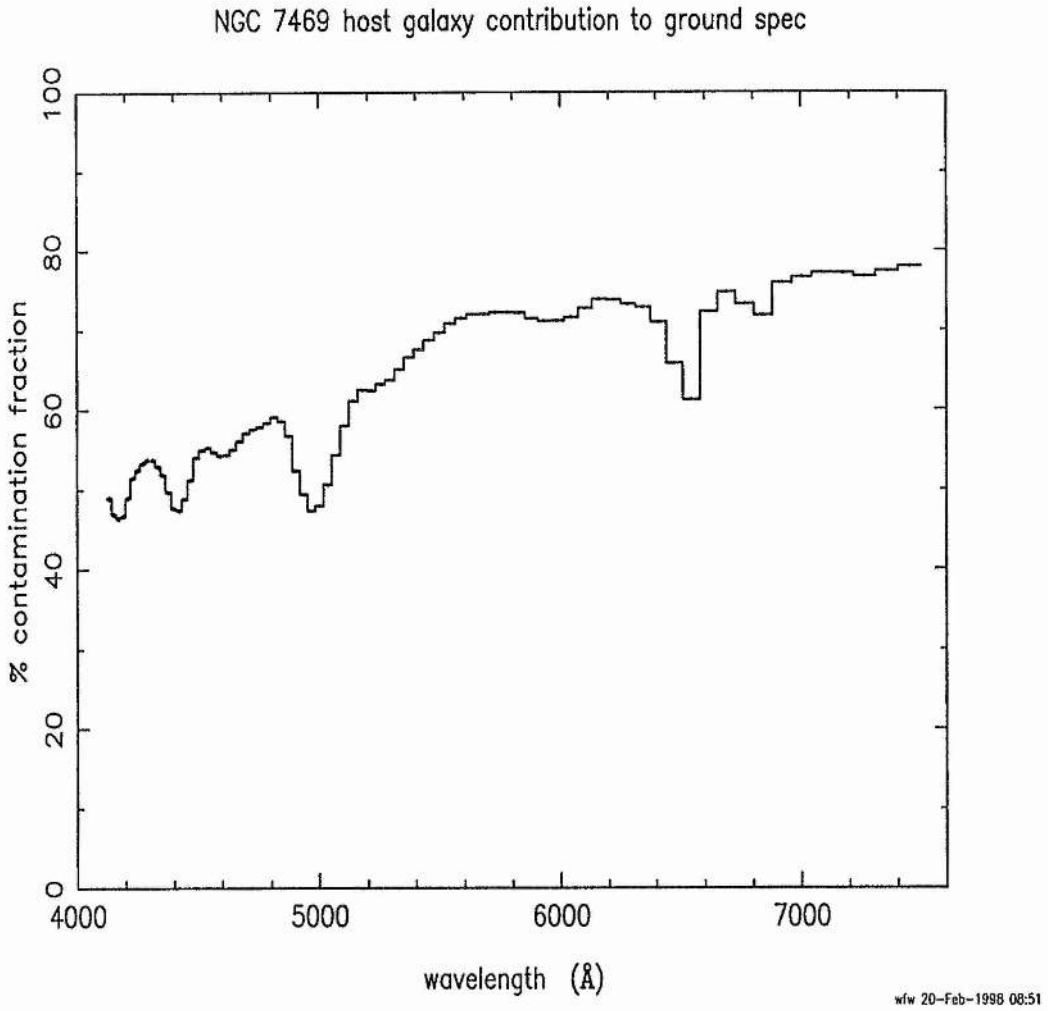

Figure 3.3: The wavelength-dependent percentage contamination of the mean optical spectrum by the host galaxy + starburst spectrum. At wavelengths long-ward of 7000 Å the percentage contamination approaches 80% (Figure kindly supplied by Dr William Welsh).

monitoring period. There follows a rise in flux of $\sim$ 40% over the next 2 months, levelling out for the last $\sim$ 30 days of the monitoring campaign.

Light curves for the intensive monitoring period are presented in Fig. 3.5. Descending from the top panel the wavelength regions are 4840–4890Å, 6925–7000Å, Hβ (4900–5000Å), and Hα (6630–6730Å). The 1315Å light curve from the IUE observations (Wanders et al. 1997) is scaled and vertically shifted to fit each of the optical light curves and is shown by the over-plotted solid line in Fig. 3.5

All the continuum regions show the same general up and down undulations in flux, with a quasi-period of $\sim$ 17 days. The full range of the variations, as defined by $(F_{\rm max}/F_{\rm min}-1)$, is $\sim$ 0.11 at 4865Å and $\sim$ 0.11 at 6925Å. A trend of decreasing flux throughout the intensive monitoring period in both emission lines is evident. The full range of variability, primarily attributable to this trend, is $\sim$ 0.21 for the Hβ light curve, and $\sim$ 0.09 for the Hα light curve. A less pronounced decline in the continuum fluxes is also evident.

3.2.2 Variability Characteristics

We use four parameters to characterise the line and continuum variability of the light curves presented in Fig. 3.5: the mean ($\overline{F}$) and rms flux ($\sigma_{\rm F}$) defined in the standard fashion (see Wanders et al. (1997)). The ratio of the maximum to the minimum flux, $R_{\rm max}$, and the amplitude of the intrinsic variability relative to the mean flux, $F_{\rm var}$, corrected for the measurement errors ϵ defined by

$$F_{\rm var} = \frac{1}{\overline{F}}\sqrt{(\sigma_{\rm F}^2 - \Delta^2)}, \tag{3.1}$$

where Δ^2 is the mean square of the measurement uncertainties, defined as

$$\Delta^2 = \frac{1}{N}\sum_{i=1}^{N}\epsilon_i^2, \tag{3.2}$$

where N is the number of data points in the light curve (Rodríguez-Pascual et al. 1997).

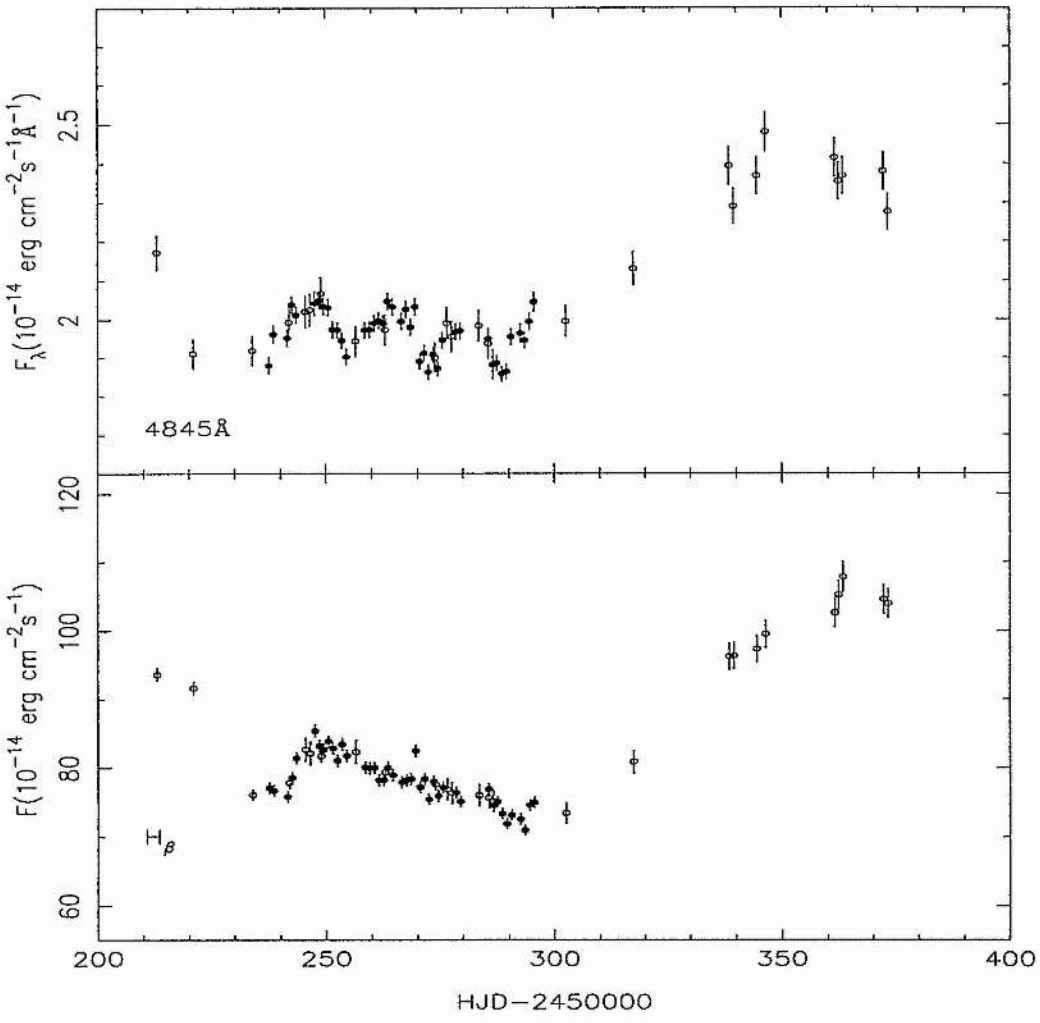

Figure 3.4: Light curves for the entire monitoring campaign, May 9 to October 16, 1996. Top panel: 4865 Å light curve. Bottom panel: Hβ light curve. The open symbols denote intercalibrated data. Discussion as in text.

Table 3.1: Continuum and Emission Line Fluxes

HJD	4845 Å	6962 Å	Hβ	Hα
212.973*	2.16± 0.04	—	89.86± 0.90	—
220.944*	1.90± 0.04	—	87.97± 0.88	—
233.952*	1.91± 0.04	—	73.04± 0.73	—
237.53	1.87± 0.02	1.95± 0.02	76.81± 1.26	394.39± 4.00
238.51	1.96± 0.02	1.93± 0.02	73.38± 1.20	389.36± 3.95
241.54	1.94± 0.02	1.90± 0.02	70.04± 1.11	382.25± 3.85
241.93*	1.98±0.04	—	74.72±0.75	—
242.54	2.02± 0.02	1.95± 0.02	75.60± 0.87	385.94± 3.87
243.49	1.99± 0.02	1.96± 0.02	76.27± 0.87	389.84± 3.92
245.53†	2.01± 0.04	—	79.34± 1.59	—
246.52†	2.01± 0.04	—	78.80± 1.58	—
247.58	2.03± 0.03	2.04± 0.03	83.41± 2.13	394.20± 4.13
248.54	2.02± 0.02	2.00± 0.02	79.82± 0.86	391.78± 3.93
248.95*	2.05± 0.04	—	78.40±0.78	—
249.54	2.01± 0.02	2.01± 0.02	80.25± 0.87	396.76± 3.98
250.55	2.01± 0.02	2.00± 0.02	81.13± 0.89	396.51± 3.98
251.54	1.95± 0.02	1.97± 0.02	80.78± 0.91	392.90± 3.95
252.55	1.93± 0.02	1.93± 0.02	78.38± 0.87	386.70± 3.89
253.53	1.91± 0.02	1.94± 0.02	80.33± 0.85	393.28± 3.94
254.54	1.89± 0.02	1.90± 0.02	78.83± 0.86	388.86± 3.90
256.51†	1.93± 0.04	—	79.90± 1.58	—
258.54	1.96± 0.02	1.93± 0.02	76.99± 0.82	388.20± 3.89
259.54	1.96± 0.02	1.92± 0.02	77.36± 0.82	387.15± 3.88

Table 3.1: continued

HJD	4845 Å	6962 Å	Hβ	Hα
260.54	1.97± 0.02	1.93± 0.02	76.45± 0.81	384.72± 3.86
261.53	1.98± 0.02	1.92± 0.02	74.33± 0.80	383.30± 3.85
262.53	1.96± 0.02	1.92± 0.02	75.29± 0.80	383.03± 3.84
262.93*	1.96±0.04	—	76.20±0.76	—
263.48	2.03± 0.02	2.00± 0.02	77.52± 0.88	396.84± 3.98
264.54	2.01± 0.02	1.98± 0.02	76.34± 0.86	391.19± 3.93
266.50	1.99± 0.02	1.91± 0.02	73.94± 0.87	379.02± 3.80
267.52	2.02± 0.02	1.97± 0.02	76.31± 0.94	390.09± 3.92
268.50	1.96± 0.02	1.92± 0.02	74.44± 0.96	382.49± 3.84
269.54	2.01± 0.02	1.99± 0.02	79.47± 1.07	396.11± 3.99
270.54	1.89± 0.02	1.86± 0.02	72.93± 0.89	382.03± 3.86
271.55	1.90± 0.02	1.90± 0.02	75.27± 0.87	381.85± 3.84
272.45	1.87± 0.02	1.88± 0.02	73.26± 0.92	379.91± 3.82
273.53	1.89± 0.02	1.92± 0.02	76.06± 0.82	388.00± 3.89
273.91*	1.89±0.04	—	74.48±0.74	—
274.53	1.87± 0.02	1.85± 0.02	72.80± 0.77	375.32± 3.76
275.55	1.93± 0.02	1.93± 0.02	74.74± 0.80	387.17± 3.88
276.51†	1.98± 0.04	—	73.78±1.48	—
277.53†	1.94± 0.04	—	73.30±1.47	—
278.46	1.95± 0.02	1.92± 0.02	73.34± 0.91	381.52± 3.85
279.45	1.96± 0.02	1.91± 0.02	71.42± 0.84	378.49± 3.81
283.50†	1.97± 0.04	—	72.98±1.46	—

Table 3.1: continued

HJD	4845 Å	6962 Å	Hβ	Hα
285.51	1.93± 0.02	1.93± 0.02	74.14± 0.83	382.17± 3.84
285.53†	1.92± 0.04	—	72.62±1.45	—
286.54†	1.87± 0.04	—	72.17±1.44	—
286.55	1.88± 0.02	1.90± 0.02	71.88± 0.82	378.68± 3.81
287.42	1.89± 0.02	1.91± 0.02	73.17± 0.83	382.98± 3.84
288.51	1.86± 0.02	1.88± 0.02	70.07± 0.77	372.36± 3.74
289.49	1.84± 0.02	1.84± 0.02	68.94± 0.77	367.97± 3.70
290.54	1.93± 0.02	1.91± 0.02	69.94± 0.80	374.86± 3.77
292.56	1.98± 0.03	1.95± 0.02	70.58± 1.42	375.93± 3.91
293.51	1.96± 0.02	1.88± 0.02	69.12± 0.81	365.35± 3.66
294.54	1.99± 0.02	1.93± 0.02	72.46± 1.00	367.85± 3.71
295.55	2.04± 0.03	1.92± 0.02	72.49± 1.42	368.96± 3.78
302.55†	1.98± 0.04	—	70.51± 1.41	—
317.43†	2.11± 0.04	—	77.59± 1.55	—
338.43†	2.38± 0.05	—	92.36± 1.85	—
339.42†	2.27± 0.05	—	92.47± 1.85	—
344.45†	2.35± 0.05	—	93.41± 1.87	—
346.36†	2.46± 0.05	—	95.51± 1.91	—
361.49†	2.40± 0.05	—	98.49± 1.97	—
362.30†	2.34± 0.05	—	101.0± 2.0	—
363.29†	2.35± 0.05	—	103.5± 2.1	—
372.22†	2.36± 0.05	—	100.4± 2.0	—
373.22†	2.26± 0.05	—	99.76± 2.00	—

* OSU Data. † CAO Data.

Heliocentric Julian Date - 2450000

Continuum fluxes in units of 10^{-14} erg cm^{-2} s^{-1} Å^{-1}. Emission line fluxes in units of 10^{-14} erg cm^{-2} s^{-1}

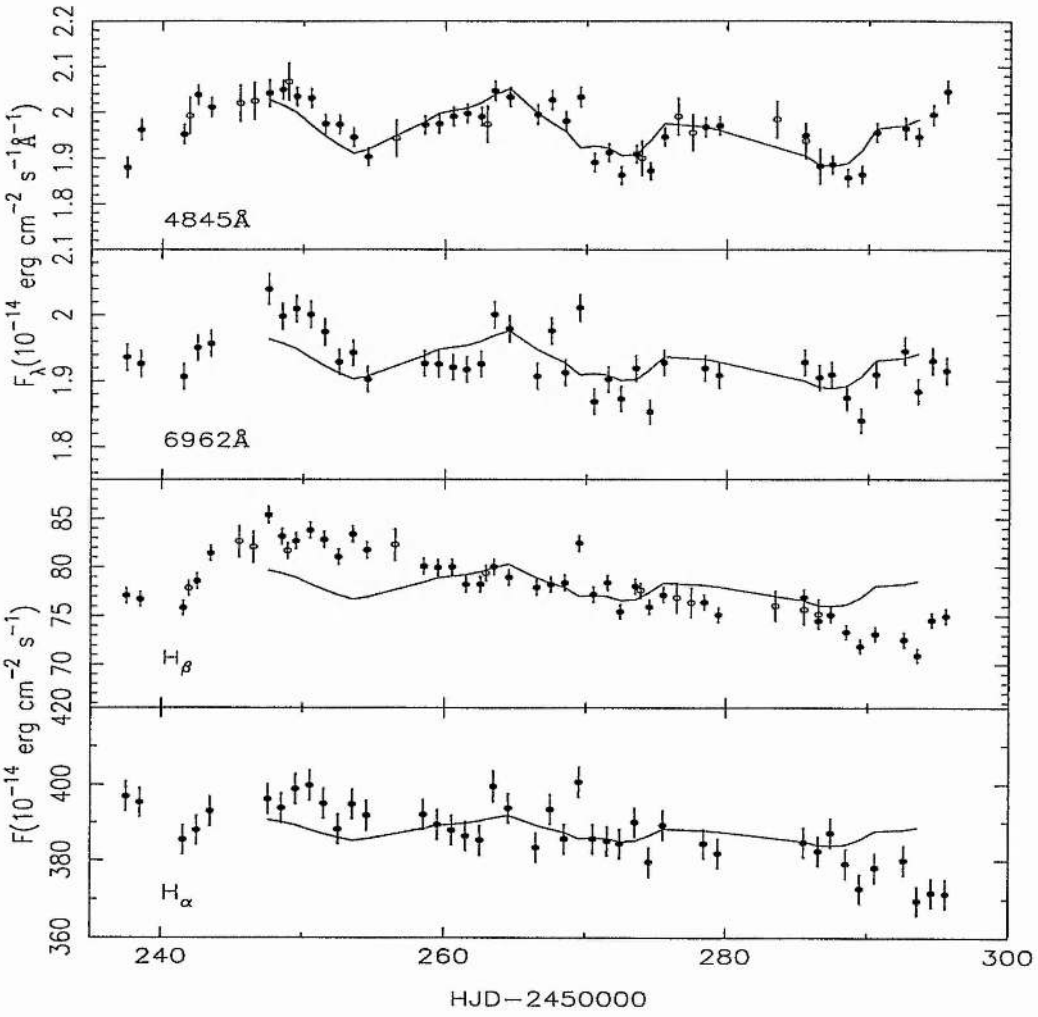

Figure 3.5: Light curves for the intensive monitoring period, June 2 to July 31, 1996. Wavelength regions as labelled in the figure. The 1315Å light curve is scaled and vertically shifted to fit each of the optical light curves, and is denoted by the solid line in each panel. The open symbols denote intercalibrated data. Line and continuum fluxes in units as labelled.

Table 3.2: Variability Parameters

Light Curve	N	$\overline{F}$[1]	σ_F^1	F_{var}	R_{max}
(1)	(2)	(3)	(4)	(5)	(6)
4865Å	54	1.95	0.05	0.02	1.11
6962Å	42	1.93	0.04	0.02	1.11
Hβ	54	7.52	0.34	0.04	1.21
Hα	42	38.4	0.84	0.02	1.09

[1] Units are 10^{-14} erg cm^{-2} s^{-1} Å^{-1} for continuum fluxes and 10^{-13} erg cm^{-2} s^{-1} for line fluxes.

The results are presented in Table 3.2, in which column 1 is the light curve considered, column 2 is the associated number of data points (N), column 3 is the mean flux ($\overline{F}$), column 4 is the rms flux (σ_F), column 5 is F_{var}, and column 6 is R_{max}. The amplitude of the intrinsic variations, F_{var}, is $\approx 2\%$ at both 4865Å and 6962Å. We note that R_{max} is not a robust measure of the variability, since the constant contribution of the host galaxy + starbursts does not cancel out in this parameter, c.f the difference of two spectral measurements, and will be sensitive to the noisier minimum flux measurement. The large red stellar spectral component acts to dilute the relative variability amplitude of the spectral variations, and is partly responsible for the apparent blue colour of the fractional variations evident in the rms spectrum, Fig. 3.1

3.3 Cross Correlation Analysis

3.3.1 NGC 7469 Cross-Correlation Analysis

A cross-correlation analysis was carried out to quantify time delays for the emission-lines and to investigate wavelength-dependent time delays in the continuum. Two algo-

rithms were employed to compute cross-correlation functions (CCFs): the interpolation CCF (ICCF) of Gaskell & Sparke (1986) (Gaskell & Peterson (1987)), as implemented by White & Peterson (1994), and the Z-transformed Discrete Correlation Function algorithm (ZDCF) of Alexander (1997). For our well sampled data the results recovered by the two algorithms are very similar.

Fig. 3.6 presents the CCFs. Earlier reports of small ($\sim$ 0.3 day) wavelength-dependent time delays in the UV data from this same monitoring campaign (Wanders et al. (1997)) led us to investigate time delays between the UV and optical data. All the optical light curves are cross-correlated with the 1315Å light curve, and only data points within the intensive monitoring period are included in the analysis. Each panel contains the CCFs for both methods. The ICCF results are presented as solid lines, the ZDCF results as the points with error-bars. The CCFs appear shifted by 1–2 days for the continuum, and 4–6 days for the lines.

The autocorrelation function (ACF) for the 1315Å light curve is over-plotted in all panels as the dashed line. The FWHM of the ACF is $\sim$ 4.9 days, indicative of the variability time-scale of the 1315Å variations. The CCFs, presented in Fig. 3.6, are broader than the 1315Å ACF, see Table 3.3. This may suggest that the optical responses extend over a range of time delays.

Table 3.3 summarizes our cross-correlation results. Column 1 is the wavelength band considered. Columns 2 and 3 detail the centroid of the CCF, $\tau_{\rm cen}$, as determined by the ICCF and ZDCF algorithms. The ICCF centroid is calculated over all points above 0.8 times the maximum cross-correlation amplitude, whereas the ZDCF centroid is computed from all points near the peak with a cross-correlation coefficient above half that of the peak. The method of calculating the ZDCF centroid is likely to suffer from a similar bias to that of the DCF, where there is some compromise between resolution and accuracy

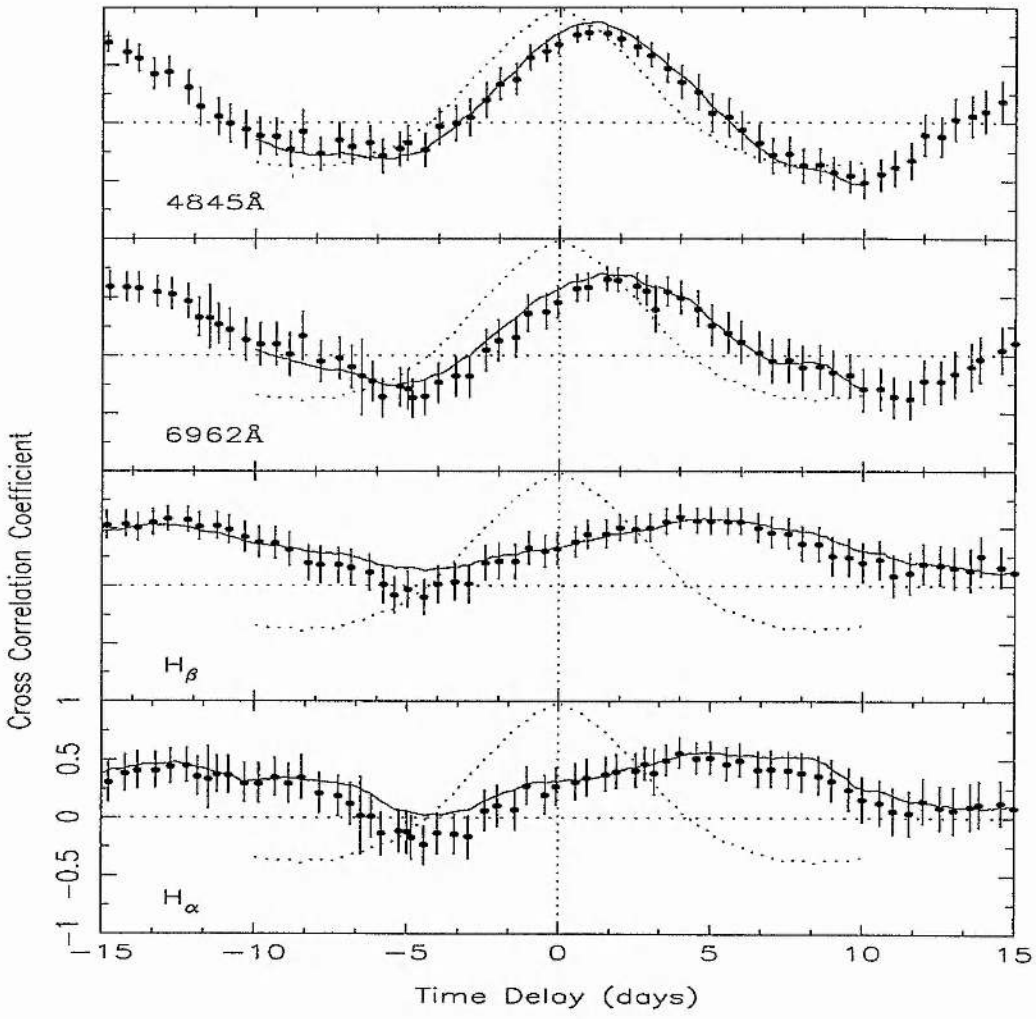

Figure 3.6: Results of Cross Correlation Analysis. The solid line represents the ICCF CCF, the dashed line is the 1315 Å ACF, and the data-points with error-bars present the ZDCF CCF. A full discussion is given in the text.

Table 3.3: Cross Correlation Analysis

Band	τ_{cen}		τ_{peak}		r_{max}		FWHM
	ICCF	ZDCF	ICCF	ZDCF	ICCF	ZDCF	ICCF
(1)	(2)	(3)	(4)	(5)	(6)	(7)	(8)
4865 Å	1.0±0.3	1.2	1.1±0.1	$0.9^{+0.7}_{-0.5}$	0.9	0.8	5.1
6962 Å	1.5±0.7	1.9	1.4±0.2	$1.6^{+0.8}_{-0.8}$	0.7	0.7	6.0
Hβ	5.4±0.8	4.3	4.8±0.5	$4.0^{+1.4}_{-1.0}$	0.6	0.6	11.9
Hα	5.6±1.3	4.4	4.3±0.4	$4.0^{+2.0}_{-1.7}$	0.5	0.6	10.9

according to the exact binning characteristics employed. This will affect the exact value of the centroid measurement, and could in principle be a significant source of uncertainty (Ignaz Wanders, Private Communication). The analysis presented here is unaffected by this particular problem. Similarly, columns 4 and 5 report the time delay, τ_{peak}, found from the peak of the CCF. Columns 6 and 7 report the maximum cross correlation-coefficient, r_{max}. Column 8 gives the FWHM of the CCF, as determined from the ICCF algorithm.

The centroid of the ICCF is 1.0±0.3 days at 4865Å, and 1.5±0.7 days at 6962Å. The corresponding strength of the correlation, r_{max}, defined by the highest cross-correlation coefficient is 0.9 at 4865Å and 0.7 at 6962Å. The error estimates for the centroid of the ICCF are computed using a "quasi-bootstrap method", as described in §3.4.3. The cross-correlation results from the two methods are always in agreement to within the quoted uncertainties.

3.3.2 Emission Line Time Delays

The bottom two panels of Fig. 3.6 show the cross-correlation of the 1315Å light curve with the mean Hβ and Hα light curves, Fig. 3.5. For Hβ and Hα, the ICCF peaks at

4.3 ± 0.4 days and 4.8 ± 0.5 days respectively, and the cross-correlation coefficient is ~ 0.6. From Fig. 3.6 and Table 3.3 we conclude that both emission line CCFs are broader than the continuum CCFs. This suggests that the Balmer line gas is responding to continuum variations with a range of time delays.

3.3.3 Continuum Time Delays

The CCFs shown in Fig. 3.6 indicate a UV to optical time delay of $\sim$ 1–2 days. To investigate further we bin the 194 Wise spectra into 40Å wide bins, over the wavelength range 4040–7720Å, and cross-correlate each of the resulting 94 mean light curves with the 1315Å light curve. Subsequently, we computed $\tau_{\rm cen}$ for each wavelength bin. The results are presented in the upper panel of Fig. 3.7. The ICCF centroid increases with wavelength, from $\sim$ 1 day at 4800Å to $\sim$ 2 days at 7500Å. The error-bars on the data-points were determined using a quasi-bootstrap method to be discussed shortly. The maximum cross correlation coefficient $r_{\rm max}$, shown in the lower panel of Fig. 3.7, is around 0.6–0.8 at most wavelengths, but with some dips near the wavelengths of the emission lines. The time delay increases above the overall trend near the emission lines because here the light curve has a mix of continuum and line flux. The lines respond with longer time delays, and the net delay is a mix of emission line and continuum time delays. This mixing also produces a decrease in $r_{\rm max}$. Dips in $r_{\rm max}$ also occur near narrow [O III] and [S II] lines due to poor wavelength shifts. Fig. 3.7 strengthens the evidence for wavelength-dependent time delays between the UV and optical continua, and confirms the time delays observed from Fig. 3.6 and Table 3.3.

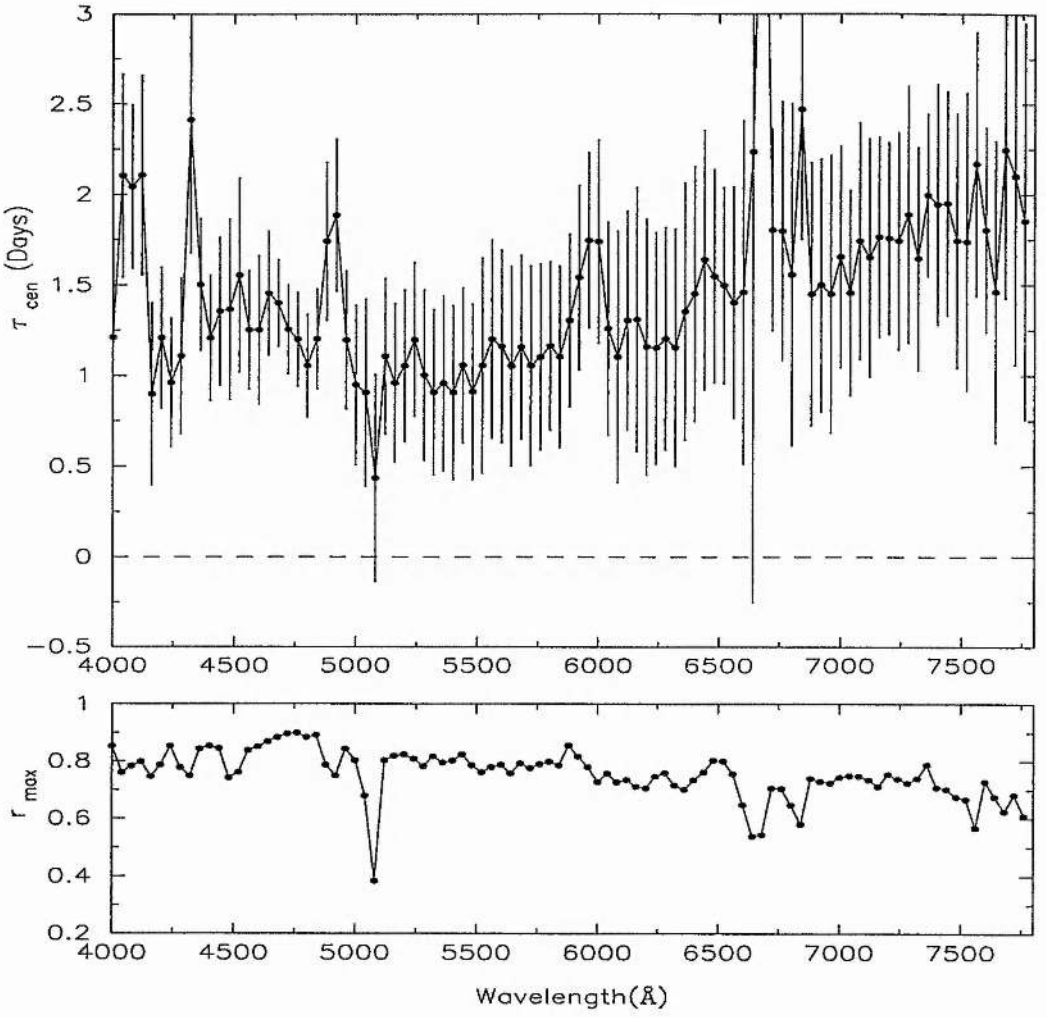

Figure 3.7: Wavelength-dependent time delays, binned to 40Å: Top panel: The data-points connected by the solid line denote the centroid of the CCF using the ICCF algorithm. The errors were assigned via a quasi-bootstrap method described in the text. Bottom panel: The data-points connected by the solid line detail the maximum cross-correlation coefficient of the ICCF algorithm.

3.4 Significance of the Wavelength-Dependent Continuum Lags

3.4.1 Instrumental and Observational Considerations

Given the implications of the results, it was considered whether the observed lags could arise from an instrumental effect. The most plausible effect, although somewhat contrived, is perhaps a modulation of the contaminating red galaxy light induced by seeing variations or pointing errors. Since the host galaxy is redder than the AGN, suitable seeing and pointing errors could in principle produce variations that mimic by accident a time delay increasing toward the red end of the spectrum. However, the following considerations convince us that this is not the case.

Fig. 3.5 shows that the rms difference between the optical continuum light curves and the scaled and shifted 1315Å light curve is $\sim$ 5%. Therefore $\sim$ 5% perturbations of the optical continuum are needed to produce the time delay. Given our estimate in §3.2 of $\sim$ 18% for the host galaxy contribution (including the starbursts contributions) , a $\sim$ 27% change in the host galaxy contamination is required to change the optical continuum by $\sim$ 5%. However, as discussed in §3.2, the host galaxy + starbursts contribution was vastly underestimated. Instead, if we assume that the host galaxy contributes about 50% of the optical continuum light, a $\sim$ 10% change in the host galaxy contamination is sufficient to change the optical continuum by $\sim$ 5%.

To assess whether so large a change in the level of contamination could be introduced by fluctuations in the seeing, we modelled how the light entering our $10'' \times 16''.8$ aperture from the nucleus and host galaxy may depend on seeing. We quantified the seeing by measuring the FWHM of the comparison star profile on each CCD frame, finding FWHM's of $\sim$ 2.8-3.3 pixels ($5''.9$–$6''.9$), Fig. 3.8. Here the top panel illustrates the approximate constancy of our seeing estimates throughout the intensive monitoring campaign. The bottom panel plots our seeing estimates against the contemporaneous 4845Å continuum

fluxes, no discernable correlation is evident to within the measurement uncertainties. A similar relationship holds for the 6962Å flux measurements.

Aperture losses from the nuclear and host galaxy component were estimated in the following simplified manner: The nuclear component was modelled as a Dirac delta function. This delta function was convolved with a Gaussian point-spread-function (psf) of FWHM = 2.8 pixels, defining the maximum nuclear light admitted through the aperture. The delta function was then convolved with progressively broader Gaussian functions in order to compute the fractional loss of light relative to the maximum admitted (the fractional loss of light was defined by the difference in areas of the resulting Gaussians). Similarly, the intrinsic galaxy component was modelled as a Gaussian with $\mathrm{FWHM}_g^2 = \mathrm{FWHM}_c^2 - \mathrm{FWHM}_{star}^2$, where FWHM_c is the FWHM estimate of the galaxy profile as estimated from the spatial profile of an individual CCD data frame, and FWHM_{star} is the FWHM of the best comparison star psf, i.e. 2.8 pixels. This procedure was then repeated to estimate the relative fractional light losses of the galaxy component. Fig. 3.9 details the aperture losses of the nuclear and galaxy components expected for the range of seeing conditions experienced throughout the monitoring campaign.

The seeing varied from $\sim 5''.9$–$6''.9$, but in this range the maximum aperture loss in light from the two components was $\sim 1\%$. Indeed on July 3 when the seeing was most variable, there were no significant ($\geq 1\%$) fluctuations. Similarly, misguiding and mis-centering (pointing) errors could result in a maximum perturbation in the aperture centre of 1 pixel, $\sim 2''$, but the change in galaxy contamination that would result is $\leq 1\%$. These tests indicate that changes in the seeing or inaccurate guiding or mis-centering of the aperture can produce changes at the 1% level, but this is not sufficient to modulate the continua by 5%. This increases our confidence in the reality of the wavelength dependent lags observed.

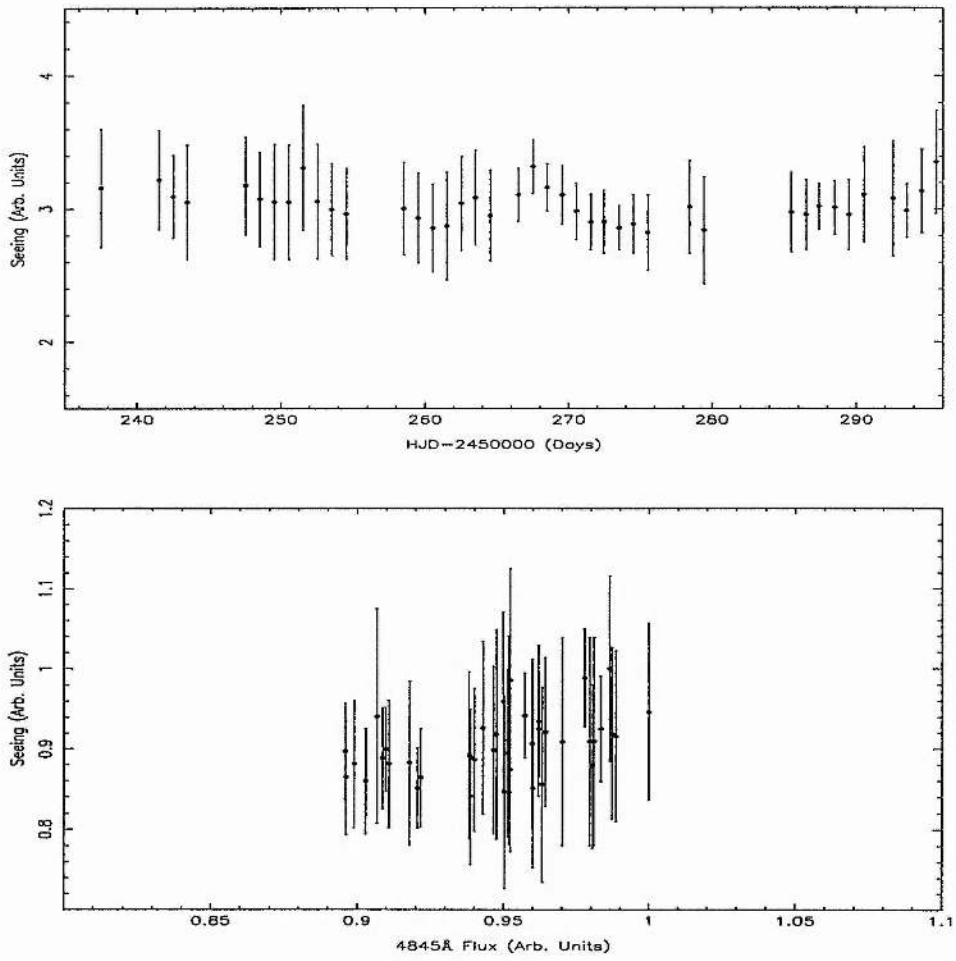

Figure 3.8: Top panel: Seeing light curve for the intensive monitoring period, June 2 to July 31, 1996. Note the approximate constancy of the seeing estimates throughout the campaign. Bottom panel: The seeing estimates are plotted against the contemporaneous 4845Å continuum flux measurements, no clear correlation is present.

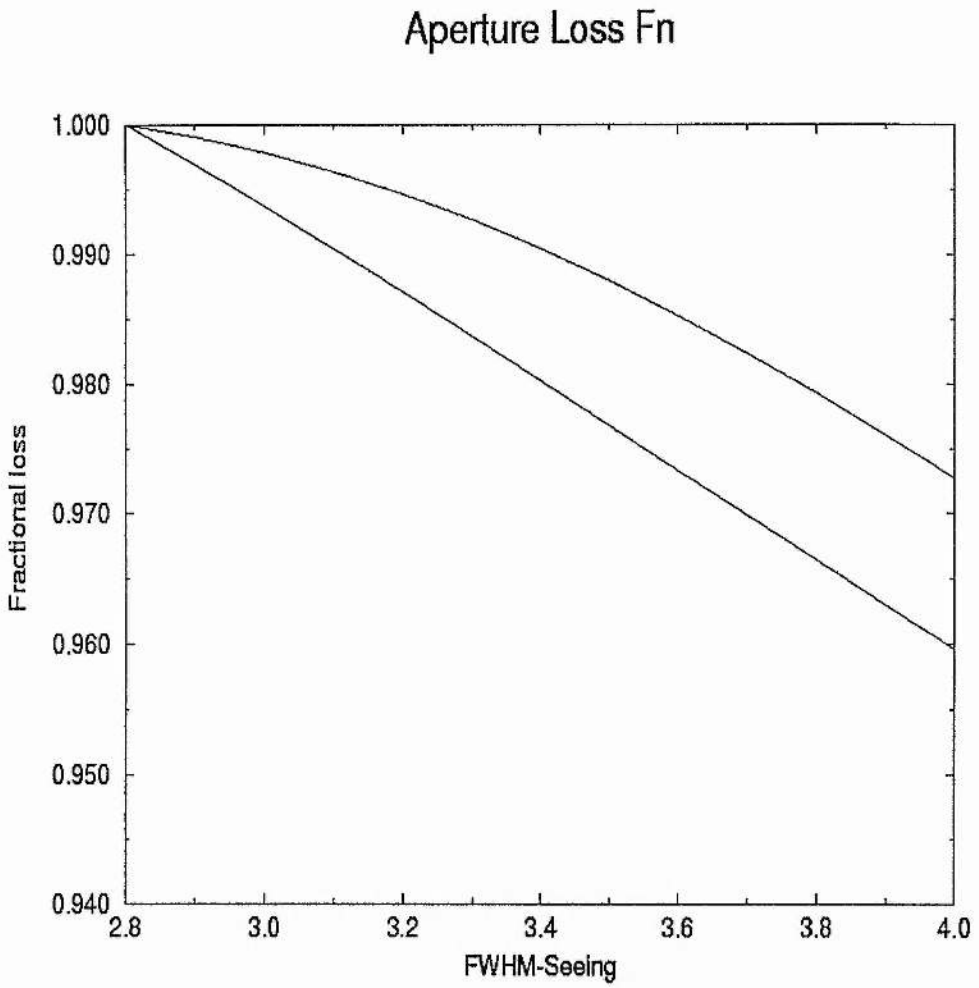

Figure 3.9: The aperture loss functions of the nuclear (upper solid line) and host galaxy (lower solid line) components. The y-axis denotes the fractional light loss relative to the best simulated conditions that are assumed to admit all the light from the nuclear and galaxy components. The x-axis denotes the seeing as estimated from the FWHM of the comparison star on each CCD data frame. The average seeing is equivalent to FWHM=3 pixels, and the observing conditions are almost always better than a seeing denoted by FWHM=3.2 pixels. It is unlikely that seeing variations throughout the campaign are a significant source of continuum modulation. Full details in text.

Table 3.4: Error Estimates for CCF lags

λ_{centre}	# bins	$< lag >$	σ
Å		days	days
(1)	(2)	(3)	(4)
5260	4	0.94 ± 0.06	0.11
7060	4	1.54 ± 0.06	0.12
7420	4	1.71 ± 0.06	0.12

3.4.2 Assessing the Uncertainties in the Continuum Lags: Method 1; RMS

To quantify and assess the significance of any wavelength-dependent lags we first validate the estimated error bars of the centroid lag determinations, represented in Fig. 3.7. The first of two methods we considered is the RMS method, as described by Wanders et al. (1997). Assuming the lag measurements of each wavelength bin are independent, we estimate $\sigma_{\rm RMS}$ as the root-mean-square variation about the mean lag over N wavelength bins. The three continuum regions considered were 5200–5320Å, 7000–7120Å, and 7360–7480Å. Table 3.4 details the results of the analysis. Column (1) is the central wavelength of the N wavelength bins, column (2) is the number of bins, column (3) is the average lag over the N bins, and column (4) is $\sigma_{\rm RMS}$. We note that $\sigma_{\rm RMS}$ should be an upper limit, since it assumes a constant lag within each continuum region. We conclude that the error in the lag determinations per bin is 0.12 days. Note the RMS error estimates may be underestimated if there is a strong correlation in the errors at different wavelengths in the same spectrum.

3.4.3 Assessing the Uncertainties in the Continuum Lags: Method 2; 'Bootstrap'

The second method was a "quasi-bootstrap" method, based on the bootstrap method (Press et al. (1992)). Given a light curve with N data points, we create 1000 synthetic light curves by selecting N points from the original light curve at random. Repeating the cross-correlation analysis for each of the 1000 synthetic datasets gives a probability distribution describing the uncertainty in the measured time delay, $\sigma_{\rm BS}$. Monte Carlo tests on Gaussian random numbers indicated that this procedure gives a distribution which is too narrow by a factor $\sqrt{(N-1)/N}$. This correction factor is applied, but is very close to 1 for large N, within 1% for the sample size of our light curves. Using the ICCF algorithm to calculate the CCFs, the 4865Å and 6962Å continua were found to lag the 1315Å light curve by 1.0 ± 0.3 and 1.5 ± 0.7 days respectively. Note that in each synthetic dataset some data points are omitted, others are duplicated. This is intended to modulate the weight given to each data-point. However, because the ICCF algorithm simply interpolates the light-curves the duplicated data-points are also effectively removed. For this reason the quasi-bootstrap errors over-estimate the errors in the centroid determination. Indeed when these error-bars are plotted in Fig. 3.7, they are clearly larger than the point-to-point scatter in the time delays at different wavelengths.

Bradley M. Peterson, Ignaz Wanders, Keith Horne, *Stefan Collier*, Tal Alexander, Shai Kaspi, and Dan Maoz, PASP, 110, 660 (1998) use a combination of this 'bootstrap' technique and assessment of flux measurement errors to investigate the reality of wavelength-dependent continuum lags in AGN. This method is a model-independent method of assessing the uncertainties in 'lags' determined by cross-correlation analysis. These authors confirm the reality of wavelength-dependent continuum lags in NGC 7469 with 97% confidence, find suggestive evidence for the existence of similar lags in NGC 4151, and statistically rule out the existence of inter-band continuum delays in NGC 5548, NGC3783, and

Fairall 9. The primary reason why wavelength-dependent continuum lags have not been observed in other extensively monitored AGN is because the campaigns lacked sufficient monitoring duration and/or temporal resolution. For example, arguably the most intensively monitored AGN was NGC 4151 (see §1.9), prior to NGC 7469, which was observed near continuously for 10 days across the electromagnetic spectrum. This compares with the NGC 7469 campaign which had comparable resolution and lasted for about 50-60 days. If this method of assessing the uncertainties in cross-correlation lags is to become widely used, we would like to see quantification of the conservative nature of the error estimates (i.e use a cross-correlation algorithm, e.g DCF, that weights the data-points).

3.5 Discussion

3.5.1 Evidence of an Accretion Disc?

The 1–2 day time delay between the UV and optical continuum variations is an intriguing result. Are we observing an extended reprocessing region? Could this be the signature of an accretion disc in this system, with harder photons from the centre of the disc reprocessed into softer ones at radii farther out? As mentioned in Chapter 1, previous campaigns indicated that continuum regions in NGC 5548 vary synchronously to within about ±2days.

The observation of wavelength-dependent time delays offers a new opportunity to test the accretion disc model of AGN. This will be the subject of the next chapter. A steady state accretion disc has a temperature distribution (ignoring effects near the centre) given by

$$T^4 = \frac{3GM\dot{M}}{8\pi\sigma R^3}, \tag{3.3}$$

where T is the effective temperature, R the radius from disc centre, M the mass of the central object, and $\dot{M}$ the accretion rate of the system. Continuum radiative reprocessing

at radius R incurs a mean time delay, $\tau = R/c$, which is independent of the disc inclination. The reprocessed light elevates the photospheric temperature of the disc, and if it resembles blackbody emission, it will peak at a wavelength $\lambda = hc/kT_*X$, where X is of order unity and T_* is the temperature of the disc due to viscous processes (equation 3.3) and heating of the disc photosphere through irradiation. We assume departures from the viscous temperature and $T \propto R^{-3/4}$ temperature structure (defined by equation 3.3) due to reprocessing are small, i.e. irradiation heating is not dominant. Substituting τ for R and λ for T in equation 3.3, we find that for an irradiated blackbody accretion disc one expects

$$\tau = 3.1\mathrm{d} \left(\frac{M\dot{M}}{10^6 M_\odot^2/\mathrm{yr}} \right)^{1/3} \left(\frac{\lambda}{10^4 \text{Å}} \right)^{4/3}. \tag{3.4}$$

We have set $X = 5.97$, i.e where the $\partial B_\lambda / \partial T$ distribution peaks, to reflect the fact that we are interested in the sensitivity of the surface brightness distribution to temperature changes. Detailed modelling will be required to justify the use of this value of X, see §4.3.9.

Having established error-bars, we now consider further the significance of the wavelength-dependent lags by fitting a number of simple models to $\tau_{(\lambda)}$. We employ wavelength bins (Fig. 3.7) within 5200–5880Å, 6080–6520Å, and 7000–7760Å, thereby excluding regions of dominant line emission. We include the data-point at 1315Å, where the lag is $\tau = 0.00 \pm 0.08$ days. The results of the model fitting are summarized in Table 3.5. Column (1) details the model fitted to the data, column (2) details which lag uncertainty estimates were used in the fitting procedure (σ =BS denotes quasi-bootstrap error estimates, σ =RMS denotes $\sigma_{\mathrm{RMS}} = 0.12$d as described earlier, column (3) is the reduced χ^2 of the model fit, χ^2_ν, and columns (4) and (5) report the relevant fitted parameter values for each model. For all cases, the number of data-points fitted is 51, and the reported error-bars have not been re-scaled to account for the quality of the fit.

Table 3.5: Model Fitting to τ vs λ relationship

Model	σ	χ^2_ν	a_1	a_2
			days	
(1)	(2)	(3)	(4)	(5)
$\tau = a_1$	BS	3.03	0.65 ± 0.10	—
	RMS	9.80	1.35 ± 0.10	—
$\tau = a_1(\lambda_*^{4/3} - \lambda_0^{4/3})$	BS	0.08	2.82 ± 0.10	1.33
	RMS	2.43	2.81 ± 0.03	1.33
$\tau = a_1(\lambda_*^{a_2} - \lambda_0^{a_2})$	BS	0.08	2.87 ± 0.19	1.40 ± 0.33
	RMS	2.47	2.77 ± 0.01	1.20 ± 0.03

Model 1 tests the null hypothesis that the continuum lag is constant over all wavelengths, i.e $\tau = a_1$. Using $\sigma_{\rm RMS}$ Model 1 gives a very poor fit to the data as indicated by the large value of $\chi^2_\nu = 9.80$, and the null hypothesis may be ruled out with great confidence. A reasonably good fit to the data is indicated by $\chi^2_\nu \simeq 1.0 \pm 0.2$, provided the error estimates are realistic. Using the larger error-bars $\sigma_{\rm BS}$ Model 1 is still a poor fit to the data, $\chi^2_\nu = 3.03$. We conclude that a constant time delay is inconsistent with the data.

Model 2 fits the function $\tau = a_1(\lambda_*^{4/3} - \lambda_0^{4/3})$, and tests the $\tau \propto \lambda^{4/3}$ prediction for an irradiated blackbody accretion disc. Here $\lambda_* = \lambda/10^4$Å, and $\lambda_0 = 0.1315 = 1315$Å$/10^4$Å. Model 2 gives $\chi^2_\nu = 0.08$ using $\sigma_{\rm BS}$, and $\chi^2_\nu = 2.43$ using $\sigma_{\rm RMS}$. The low χ^2_ν obtained using $\sigma_{\rm BS}$ indicates that these error-bars may be too large. Figure 3.10 presents the results of fitting Model 2 to the data. The top panel assumes $\sigma_{\rm RMS}$, and the bottom panel uses the $\sigma_{\rm BS}$. The best fit line for Model 2 is detailed as the solid line in each panel.

Model 3 fits the function $\tau = a_1(\lambda_*^{a_2} - \lambda_0^{a_2})$, similar to Model 2 except that the data is given more freedom to determine a best fit wavelength dependence, a_2. The fits are similar

to those obtained with Model 2, $\sigma_{\rm BS}$ yielding $\chi^2_\nu = 0.08$, and $\sigma_{\rm RMS}$ giving a $\chi^2_\nu = 2.47$. Model 3 tests the $T \propto R^{-3/4}$ law, which gives rise to $\tau \propto \lambda^{4/3}$.

Adopting $\sigma_{\rm BS}$ Models 2 and 3 are both consistent within the quoted uncertainties and support the notion of a wavelength-dependent lag that is consistent with the prediction of a steady state irradiated blackbody accretion disc. Adopting the best fit estimate for the parameter a_1 in Model 3 (σ =RMS) we find that $a_1 = 2.8 \pm 0.7$ days, where the error estimate is the 68% confidence estimate. This error estimate accounts for the correlation of the parameters a_1 and a_2.

3.5.2 Mass and Accretion Rate of the Black Hole

The best fit parameter $a_1 = 2.8 \pm 0.7$ days in Model 3 can be identified with the constant $3.1(M\dot{M}/10^6 M_\odot^2 {\rm yr}^{-1})^{1/3}$days in equation 3.4 to estimate $M\dot{M}$. We estimate $M\dot{M} = (0.7^{+0.7}_{-0.4}) \times 10^6 M_\odot^2 {\rm yr}^{-1}$. Lines of $M\dot{M} = 10^5$, 10^6 and 10^7 $M_\odot^2 {\rm yr}^{-1}$ are over-plotted in each panel of Fig. 3.10

A crude estimate for the mass of the supposed black hole in NGC 7469 may be made. We calculate the "Keplerian mass" assuming an edge-on circular accretion disc, with a velocity $V = FWHM/2$. For the "virial mass" we assume random motions of line emitting material in a spherical geometry, with a velocity $V = (\sqrt{3}/2)FWHM$ (Netzer (1990)). The mass is

$$M = \frac{V^2 \tau c}{G}. \tag{3.5}$$

For the $FWHM$ we use the velocity profile of the line from the rms spectrum in Fig. 3.1, and for τ we use the cross-correlation time delay, $\tau_{\rm cen}$, with respect to the 1315Å light curve. The $FWHM$ of the Balmer lines was measured by fitting a single Gaussian plus straight line model to the *variable* component of the line profile. The fit to the Hβ line profile yielded a $\chi^2_\nu = 0.7$. The fit to the Hα line profile yielded a poor $\chi^2_\nu = 9.0$,

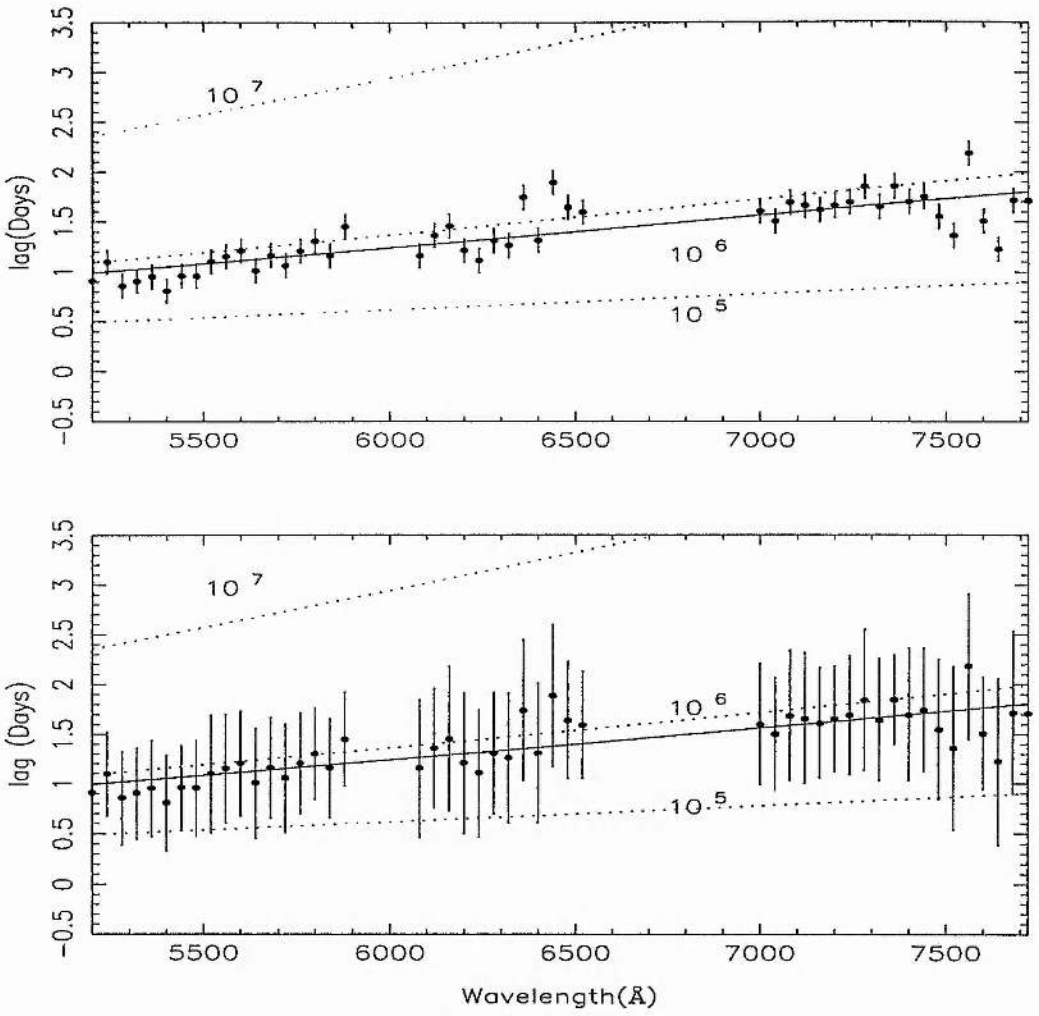

Figure 3.10: The irradiated blackbody accretion disc model $\tau = a_1(\lambda_*^{4/3} - \lambda_0^{4/3})$ is fitted to the wavelength-dependent time delays ($\lambda_0 = 0.1315$ and $\lambda_* = \lambda/10^4$ Å). To exclude regions of dominant line emission only wavelength bins within 5200-5880Å, 6080-6520Å, and 7000-7760Å are included in the fit. Top panel: Assumes constant lag uncertainties of 0.12 days. The solid line represents the best fit line (Model 2) to the data, $\chi^2_\nu = 2.43$. The three dashed lines represent $M\dot{M} = 10^7, 10^6$, and $10^5 M_\odot^2 \mathrm{yr}^{-1}$. Bottom panel: Identical to the top panel, but with lag uncertainties as estimated from the quasi-bootstrap procedure described in §3.4.3. The solid best fit line has a $\chi^2_\nu = 0.08$. We estimate $M\dot{M} = (0.7 \pm^{+0.7}_{-0.4}) \times 10^6 M_\odot^2 \mathrm{yr}^{-1}$.

Table 3.6: Virial and Keplerian Mass Estimates

Emission Line	V_{Virial} (km s^{-1})	$V_{Keplerian}$ (km s^{-1})	R (light-days)	M_{Virial} $10^6\,M_\odot$	$M_{Keplerian}$ $10^6\,M_\odot$
(1)	(2)	(3)	(4)	(5)	(6)
Hα	2343±300	1353±300	5.6 ± 1.3	6.0 ± 4.5	2.0 ± 1.4
Hβ	2934±152	1694±152	5.4 ± 0.8	9.1 ± 2.8	3.0 ± 0.9

due to imperfect wavelength calibration resulting in spurious peaks in the rms spectrum near each of the narrow lines. We reflect this fact in the error estimate for the $FWHM$ measurement of this line. We note that multiple narrow and broad Gaussian component fits to the Balmer lines of the mean spectrum, Fig. 3.1, yield estimates for the $FWHM$ of the lines to be $\sim$ 30–40% larger than those estimated by fitting to the variable component of the lines. Table 3.6 summarises the rough mass estimates. Column 1 is the emission line feature considered, column 2 is the virial velocity V of the emission line as measured from the rms spectrum in Fig. 3.1, column 3 is the Keplerian velocity of the emission line as measured from the rms spectrum in Fig. 3.1, column 4 is the time delay of the emission feature from the CCF (Fig. 3.6), column 5 is the virial mass estimate and column 6 is the Keplerian mass of the central source.

The different mass estimates for the lines are internally consistent to within the quoted uncertainties. A weighted average of the mass estimates yields virial and Keplerian masses of $(8.3 \pm 2.4) \times 10^6 M_\odot$ and $(2.7 \pm 0.8) \times 10^6 M_\odot$ respectively. The difference in mass estimates indicates the large systematic uncertainty, depending on the unknown geometry and kinematics of the line emitting gas. Koratkar & Gaskell (1991) derived the mass of the central object in 10 AGNs in a consistent manner. The central sources were found to have masses of about $10^{7-8}\,M_\odot$. Their mass estimates utilised the FWHM as measured from a

mean spectrum compared to our measurement of the FWHM from an rms spectrum.

Combining the Keplerian mass estimate with the estimate of $M\dot{M}$ we derive an estimate for the accretion rate of the system, $\dot{M} = (0.3 \pm 0.2) M_{\odot}$ yr^{-1}. Assuming an accretion efficiency $\eta = 0.1$, the bolometric luminosity ($\eta \dot{M} c^2$) of NGC 7469 would then be $(1.7 \pm 1.1) \times 10^{45}$erg s^{-1}. The observed X-ray luminosity in the 0.5–4.5 keV region is $10^{43.4}$erg s^{-1} (Green et al. (1992)). Note the values for $M\dot{M}, M, \dot{M}$ and the bolometric luminosity are calculated under strict assumptions, as detailed in this chapter, that require extensive investigation.

3.6 Conclusions

An intensive spectrophotometric optical monitoring campaign on the Seyfert 1 galaxy NGC 7469 was undertaken during June-July 1996. The main results are summarised as follows:

1. The Hβ and Hα emission lines respond to the 1315Å continuum variations with a time delay of $\sim$ 5–6 days. We consider this to be identification of gas emitting variable Balmer lines at a distance of $\sim$ 5–6 light days from the central source.

2. By combining the emission line lags and the widths of the variable component of the emission lines, we estimate the mass of the central source is $M \sim 10^{6-7}\, M_{\odot}$.

3. Significant wavelength-dependent time delays are detected in the continuum. Variations at optical wavelengths lag behind those at 1315Å. Cross-correlation of the light curves shows the delay increases from $\sim$ 1 day at 4800Å to $\sim$ 2 days at 7500Å. We interpret this as evidence for a stratified continuum reprocessing region close to the central source, possibly that of an accretion disc. With this interpretation the delays are consistent with the predicted $\tau \propto (M\dot{M})^{1/3} \lambda^{4/3}$ relationship for an irradiated blackbody accretion disc with temperature profile $T \propto R^{-3/4}$, and suggest $M\dot{M} = (0.7^{+0.7}_{-0.4}) \times 10^6 M_{\odot}^2$ yr^{-1}.

More detailed modelling and analysis of the results remains to be done to investigate these wavelength-dependent time delays, and test the applicability of the disc hypothesis. Concurrently, we believe the potential implications of these observations require immediate observational verification. Principally, this is possible with high signal to noise, photometric observations of comparable temporal resolution.

Chapter 4

A new direct method for measuring the Hubble constant, H_0, from reverberating accretion discs in active galaxies

4.1 Summary

The optical variations of NGC 7469 lagged behind those at UV wavelengths by about 1−2 days. This was interpreted, §3.4, as evidence for a stratified continuum reprocessing region close to the central source, possibly that of an accretion disc. The delays are consistent with the $\tau \propto \lambda^{4/3}$ relationship for an irradiated blackbody accretion disc with temperature profile $T \propto R^{-3/4}$. These wavelength-dependent time delays test the standard black hole-accretion disc paradigm of AGN by tracing the temperature structure of the gaseous material that surrounds the purported black hole, and will provide the indirect, 'smoking gun', evidence for the existence of accretion disc structures in AGN.

When we observe a time delay τ at wavelength λ, that in effect measures the mean radius $R = \tau c$ at which the disc has a temperature T. The temperature T is then related to wavelength λ for a given local thermal energy distribution, e.g. for blackbody radiation $T = hc/k\lambda X$ with $X \approx 3 - 4$. The disc flux, which is a function of the distance D to the AGN, can be calculated by summing up the contributions from various disc annuli. The predicted spectrum is then scaled to the observed spectrum to derive a

redshift-independent luminosity distance. The luminosity distance permits an estimate of $H_0\sqrt{\cos i}$. Analysis of the observed spectral energy distribution and wavelength-dependent time delays will yield redshift-independent distances to AGNs. This opens up a new route to H_0 and by extension to fainter objects at $z \sim 1$, q_0.

This chapter is based on the paper **Collier, S et al., "A new direct method for measuring the Hubble constant from reverberating accretion discs in active galaxies", MNRAS, 302, L24, 1999.** This chapter serves as an introduction to the method. In §4.2 we present introductory material concerning the extragalactic distance scale and outline the importance of accurate measurements of cosmological parameters. The theory of the method is discussed in §4.3, and applied to data from the International AGN Watch multi-wavelength monitoring campaign on NGC 7469 in §4.4. §4.5 presents a discussion of systematic uncertainties in the method. We discuss a selection of simple blackbody disc fits in §4.6, and the accuracy of our Hubble constant estimate in §4.7. The conclusions of this work are presented in §4.8

4.2 Introduction: The Extragalactic Distance Scale

The Hubble constant H_0 and deceleration parameter q_0 are fundamental parameters in cosmology, measuring respectively the rate at which the Universe is expanding and the rate at which that expansion is impeded by the attractive force of gravity. Moreover, H_0 determines a size scale and age of the Universe, constrains the baryonic density produced in the Big Bang, the amount of dark matter in the Universe, and the epoch for galaxy and quasar formation in the early Universe. An accurate measurement of the deceleration parameter determines the ratio of the actual density to the critical density required to just halt the expansion of the Universe at some infinite cosmic epoch, and hence determines the geometry of the Universe.

The value of the Hubble constant remains in dispute after over half a century of intensive studies (Rowan-Robinson (1988), van den Bergh (1992), and de Vaucouleurs (1993)). A corollary concerns the age of the Universe, t_0. If one adopts $H_0 > 75\ \mathrm{km\,s^{-1}\,Mpc^{-1}}$, the age of an Einstein-de Sitter Universe is $t_0 < 8.7\,\mathrm{Gyr}$ (For an Einstein-de Sitter Universe $H_0 \to 0$ with $t_0 \to \infty$). This age would be in severe conflict with the $12 - 17\,\mathrm{Gyr}$ ages of the oldest globular clusters (van den Bergh (1992)) and less than the age of the galactic disc derived from nucleo-cosmochronology (Winget (1987)). Therefore the value of H_0 and subsequent t_0 must not only be consistent with Inflation models for the early Universe, structure formation, and cold dark matter (CDM) theories but also with the available observational data (For a complete treatment of different cosmological models the reader is referred to any good cosmology textbook).

Inextricably linked with the determination of H_0 is the accurate measurement of distances to astronomical sources. The *extragalactic distance scale* is defined by the application of numerous methods of calibrating and measuring distances to different types of astronomical sources, from the nearby Milky Way stars to distant Supernova explosions of stars in other galaxies.

There are a variety of methods for determining distances to astronomical objects; The method of trigonometric parallax, used to determine the distance to Venus in 1761, can measure distances to about a kiloparsec (kpc) or so. The moving cluster method was used to determine the distance to the Hyades cluster, and by comparing other cluster main sequences (*main sequence fitting*) with that of the Hyades cluster, distances to about 7 kpc can be measured. Spectroscopic parallax measurements allow measurements to distances of about 7 Mpc.

Broadly speaking there are two distinct methods of calibrating distances to galaxies. The first group of methods relies on accurate distances to nearby objects to calibrate a

'distance ladder' extending to objects further away. A recent successful example of this is the HST key project (Freedman et al. (1994), Freedman et al. (1997)) that aims to measure the Hubble constant with an accuracy of 10% by using Cepheid variables as standard candles to measure distances to the Virgo Cluster.

Cepheid variables are a class of variable star that have a well defined period-luminosity relationship. The pulsation period determines the absolute magnitude of the star, and combined with the apparent magnitude allows the inference of the distance modulus. This period-luminosity relationship requires zero-point calibration, by measurement of the distance to a classical, nearby Cepheid. Similar techniques can be applied to variable RR Lyrae stars in globular clusters, and extend the distance scale to about 20 Mpc.

Uncertainties in distance measurements using this method are of the order of 10-20%, and include; zero-point calibration errors (i.e. the distance to the Large Magellanic Cloud), extinction of fluxes by intervening dust, the relative positioning of galaxies within Clusters of galaxies and peculiar velocities that are independent of the Hubble flow. Current estimates of H_0 using this and similar methods (Tanvir et al. (1995)) are in the range $\approx 60 - 90\ \mathrm{km\,s^{-1}\,Mpc^{-1}}$.

By accurately calibrating distances to the Virgo Cluster galaxies the 'distance ladder' is extended via numerous secondary methods: The empirical $D_{\mathrm{ang}} - \sigma$ relation (Faber et al. (1989)) relates the angular diameter D_{ang} (strictly speaking the D_{ang} to a given surface brightness level) of an elliptical galaxy to its velocity dispersion σ. The galaxy surface brightness distribution is independent of the galaxy's distance D, and D_{ang} is inversely proportional to D. The zero-point primary distance calibration of the relationship is complicated by the absence of bright elliptical galaxies, however, relative distances of clusters can be determined to about 100 Mpc. The Tully-Fisher relationship (Tully & Fisher (1977)) for spiral galaxies relates the absolute magnitude to the maximum rota-

tional velocity, and extends to similar distances of about 100 Mpc. The surface–brightness fluctuation method (Tonry & Schneider (1988)) is a statistical analysis that measures a galaxy's distance from the magnitude of the spatial pixel-to-pixel surface brightness variations recorded by a CCD camera, and currently extends to distances of about 50 Mpc. Finally, the type Ia supernova method (Sandage et al. (1996)) defines the absolute magnitude of the supernova at maximum light, $M_B = -19.6 \pm 0.2$, and allows distance measurements to about 1000 Mpc.

The second group of methods does not require any calibration or progression along a 'distance ladder' but applies directly to the object concerned. These methods include; gravitational lens systems (Refsdael (1964) and Kundic et al. (1997)) where a time delay between light variations from two gravitationally lensed images of a background point source, e.g. a quasar, and the angular separation of the images allows measurement of H_0. In principle this technique can be used to measure distances $>$ 1000 Mpc, however, uncertainties in the underlying luminous and/or dark mass distributions and perturbations in the lensing potential due to clustering are yet to be quantified. The Sunyaev-Zel'dovich (SZ) method (Sunyaev & Zel'dovich (1980), McHardy et al. (1990), and Freedman et al. (1997)); which measures a decrement in the microwave background spectrum, caused by the inverse-Compton scattering of photons from the cosmic microwave background off hot electrons in the X-ray gas of rich clusters. By mapping the spatial distribution of the SZ effect and X-ray cluster gas one constrains the density and temperature, with the mean electron temperature derived from an X-ray spectrum. The X-ray flux is distance dependent whereas the SZ decrement temperature is not. This allows an estimate of H_0 based on the definitions of the angular diameter and luminosity distances. Similarly, the SZ method may be applied to distances $>$ 1000 Mpc, but with the following caveats; Clumpiness of the X-ray cluster gas (which serve to reduce the derived value of H_0),

projection effects (e.g. if the cluster is prolate, H_0 may be underestimated), model-dependencies and assumptions for the cluster system, and possible contamination from surrounding point sources. Current early estimates of H_0 using these two methods are in the range $\approx 30 - 80$ km s^{-1} Mpc^{-1}. These direct methods give an important check on 'distance ladder' methods.

AGNs are important cosmological probes because their high luminosity allows them to be observed at large redshifts (observing a $z = 5$ quasar allows us to look back in time to when the Universe was about 7% of its current age, probably < 1 Gyr after the Big Bang). By searching for the oldest quasars one can determine a time-scale for the discrete formation of galaxies in the early Universe, and quasar surveys allow detailed studies of the evolving chemical and spatial distribution of the Universe, e.g. measuring luminosity functions (relative numbers of objects of different luminosities in a given volume of space, see for example Boyle et al. (1998)). However, a vital prerequisite of the aforementioned is the determination of the distance to the AGN.

Correlations between the luminosity and various emission line strengths and ratios (Baldwin (1977) and Kinney et al. (1990)) have been investigated for many years, but have not yet allowed a consistently accurate inference of the distance to AGNs independently of their redshifts. For example, the empirical Baldwin effect (1977) relates the equivalent width of a broad emission line, typically C IV, to the continuum luminosity, $EW(CIV) \propto L_\lambda^\beta$ with $\beta = -0.17$. The aim is to use the Baldwin effect (1977) as a 'standard candle' tool. By taking a spectrum of an object, the equivalent width can be measured and the source luminosity inferred, and hence the distance measured. Significant difficulties persist in the application of this technique, such as, calibration and removal of the scatter in the relationship due to light travel time effects that relate the continuum luminosity at some prior epoch to a later emission line epoch, a poor understanding of the nature of the

correlation (e.g. disc-inclination effects, the continuum luminosity driving the emission lines, etc) and problems associated with evolutionary effects of the AGN population (see Korista et al. (1998) and references therein).

A promising geometrical method that uses proper motions and line-of-sight accelerations of water vapour maser emission in NGC 4258 yields an accurate distance of 6.4 ± 0.9 Mpc (Miyoshi et al. (1995)). In principle, a similar method may be employed to infer distances to AGN maser sources but not to much higher redshifts where proper motions become too small. This method may also be limited by its preferential selection of near edge-on systems.

We propose a new method that utilizes the relatively simple physics of light travel time and blackbody radiation to measure directly redshift-independent luminosity distances to AGNs, and hence determine H_0. Concurrently, the method allows a powerful test of the standard paradigm of AGN by tracing the temperature structure of the gas in the innermost regions.

4.3 Theory

4.3.1 The Reprocessing Hypothesis

The reprocessing hypothesis assumes that the UV/optical continuum variations represent the response of gaseous material to variations in the higher-energy continuum. The stringent upper limits, < 0.3 day, on time delays between the X-ray and UV variations in NGC 4151 (Edelson et al. (1996)) suggest that the variations in different wave-bands must be radiatively coupled (i.e. any possible time delays are due to light-travel time effects), since, for example, viscous time scales are much too long. The viscous time scale $t_{\rm vis}$ is the time-scale on which the local surface density changes, and is of the order of hundreds of days to years for AGN accretion discs. Furthermore, the equivalent width of

Fe Kα at 6.4 KeV (EW in the range 50-300 keV (Mushotzky et al. (1993)) corresponds to velocity dispersions of the order $10\,000\,\mathrm{km\,s^{-1}}$. Further, the location of rest energy of the line depends on the ionization state of Fe, and suggests it is formed in low-ionization cold gas) and the strength of Compton reflection (i.e. inelastic scattering of high energy photons off low energy, cold electrons) observed at > 10 KeV suggest that a large fraction of X-rays generated by an isotropic source must be reprocessed by relatively cold ($< 10^6$ K) optically thick gas, possibly that of an accretion disc (Pounds (1990) and George & Fabian (1991)). This has led to 'ad hoc' models where the higher-energy, e.g X-ray, source illuminates the accretion disc from above.

We assume a similar mechanism must be operating, i.e some variable source of high-energy radiation in the vicinity of the disc axis illuminates the disc and radiatively drives the UV/optical continuum variations. The exact mechanism is unknown, but may include; magnetic flaring in a hot corona surrounding the accretion disc (Haardt & Maraschi (1993)), electron scattering in the disc corona (Laor & Netzer (1989)), self-irradiation of the disc by high-energy photons being bent from the back side of the disc (Sanbuichi et al. (1993)), central illumination of a flared concave disc surface (Shakura & Sunyaev (1973)) and illumination from a source above a flat disc geometry.

4.3.2 The Temperature Structure of the Accretion Disc

An optically thick steady state blackbody accretion disc illuminated by a central source has a radial temperature profile $T(R)$ that is a non-linear combination of the surface temperature due to viscous heat dissipation $T_{\rm vis}$ and that due to irradiation $T_{\rm irr}$ of the disc, $T^4 = T_{\rm vis}^4 + T_{\rm irr}^4$. Explicitly (ignoring general relativistic and other effects near the centre),

$$T^4 = T_{\rm vis}^4 + \left(\frac{AL_x}{4\pi\sigma R_*^2}\right)\cos\theta_{\rm x},$$

$$T_{\rm vis}^4 = \left(\frac{3GM\dot{M}}{8\pi\sigma R^3}\right), \tag{4.1}$$

where $T_{\rm vis}$ is the temperature of the disc surface due to viscous heat dissipation, A is the absorbed fraction of the radiation impinging on the disc surface, M is the mass of the black hole, $\dot{M}$ is the accretion rate, R is the radial distance from the black hole, $L_{\rm x}$ is the irradiating luminosity, R_* is the distance from the illuminating source to the surface element of the disc, and $\theta_{\rm x}$ is the angle between the disc surface normal and a unit vector from the surface element to the variable central source.

It is clear from eqn. 4.1 that $T(R)$ depends on both the geometry of the accretion disc (i.e. $\cos\theta_{\rm x}$) and the relative prominence of viscous heat dissipation and irradiation effects. For example, when $T(R)$ is determined by viscous dissipation alone, a $T \propto (M\dot{M})^{1/4}R^{-3/4}$ structure exists (Shakura & Sunyaev (1973)). Similarly, an irradiating source situated a height $H_{\rm x}$ above the disc plane induces a $T \propto (L_{\rm x}H_{\rm x})^{1/4}R^{-3/4}$ structure for $R >> H_{\rm x}$, provided the disc thickness $H << H_{\rm x}$ (This is realized by balancing the energy radiated per unit area (e.g. σT^4) with the irradiating energy per unit area (e.g. $(AL_{\rm x}/4\pi R_*^2)\cos\theta_{\rm x}$).

4.3.3 Wavelength-dependent Time Delays

When high-energy radiation is emitted from the central regions of the disc, a wave of heating propagates out at a speed c arriving at radius R after a mean time $\tau = R/c$. At this radius R the temperature $T(R)$ rises slightly, thereby emitting more photons near wavelength $\lambda = hc/kTX$, the peak of the local blackbody energy distribution given by the Wien Law (where $X \approx$3–4 for blackbody radiation). When we observe a time delay τ at wavelength λ that in effect measures the radius $R = \tau c$ at which the disc has temperature $T = hc/k\lambda X$.

The response of the reprocessed emission is delayed relative to detection of the high-

energy radiation because of the longer total path taken from the driving source–reprocessing site–observer, c.f the high-energy radiation path of source–observer. Explicitly, the time delay is given by

$$\tau = \frac{R}{c}(1 + \sin i \cos\theta), \tag{4.2}$$

where i is the disc inclination and θ is the azimuth angle from the back edge of the disc. So, a disc annulus of fixed R responds with mean time delay $\tau = R/c$ and a range of time delays $\tau = (R/c)(1 \pm \sin i)$. The exact functional form of the time delay distribution, eqn. 4.2, will depend on the geometry of the accretion disc model, Rokaki et al. (1992). Disc geometries that incur a time delay distribution given by eqn. 4.2 include; A flat disc illuminated by a source H_x above the plane for $R >> H_x$, a flaring concave disc, with height $H \propto R^{\beta}$, illuminated by a centrally located point source (provided $H/R << 1$), and a flaring concave disc illuminated by a source H_x above the disc midplane (provided $(H - H_x)/R << 1$).

For a temperature profile of the disc, $T = T_0(R/R_0)^{-b}$, the wavelength-dependent time delay is

$$\tau = R_0(h/k)^{-1/b} c^{-(b+1)/b} T_0^{1/b} \lambda^{1/b} X^{1/b}, \tag{4.3}$$

where T_0 is the temperature of the disc at radius $R_0 = 1$ light day. Hence, the observed $\tau(\lambda)$ determines $T(R)$.

Assuming a characteristic $T = T_0(R/R_0)^{-3/4}$, the wavelength-dependent time delay is

$$\tau(\lambda) = 3.9\mathrm{d} \left(\frac{T_0}{10^4\,\mathrm{K}}\right)^{4/3} \left(\frac{\lambda}{10^4\,\text{Å}}\right)^{4/3} \left(\frac{X}{4}\right)^{4/3}. \tag{4.4}$$

Note a disc with $T \propto R^{-3/4}$ predicts a $\tau \propto \lambda^{4/3}$ wavelength-dependent time delay. The explicit inclusion of X in the above equations is for heuristic purposes, since X is not a free parameter/variable but is determined by the blackbody model, see §4.3.9.

4.3.4 The Disc Spectrum

The predicted spectrum of the accretion disc can be calculated straightforwardly by summing up the blackbody contributions from various disc annuli (Shakura & Sunyaev (1973)). The disc spectrum is given by

$$f_\nu = \int_{R_{\rm in}}^{R_{\rm out}} B_\nu d\Omega = \int_{R_{\rm in}}^{R_{\rm out}} \frac{2hc}{\lambda^3} \frac{1}{e^{hc/\lambda kT} - 1} \frac{2\pi R dR \cos i}{D^2}, \tag{4.5}$$

where B_ν is the Planck function, $d\Omega$ is the solid angle subtended by the disc annuli, $R_{\rm in}$ is the inner radius of the disc, $R_{\rm out}$ is the outer radius of the disc, i is the inclination of the disc and D is the distance to the AGN.

Adopting the temperature profile $T = T_0 y^{-b}$ with $y = R/R_0$ and $s_0 = hc/\lambda k T_0$ such that $s = s_0 y^b$ and $dy = y ds/bs$, the disc spectrum is

$$f_\nu = \frac{2hc}{\lambda^3} \frac{2\pi R_0^2 \cos i}{D^2} \int_{R_{\rm in}}^{R_{\rm out}} \frac{y dy}{e^{s_0 y^b} - 1}. \tag{4.6}$$

This reduces to

$$f_\nu = \frac{4\pi R_0^2 \cos i}{D^2} (hc)^{1-2/b} \lambda^{2/b-3} (kT_0)^{2/b} \frac{I_2(b)}{b},$$

$$I_n(b) = \int_0^\infty \frac{s^{n/b-1} ds}{e^s - 1}, \tag{4.7}$$

where $I_n(b)$ is evaluated numerically and $I_2(3/4) = 1.93$ (see Fig. 4.1).

Assuming a temperature profile index $b = 3/4$, one can substitute $(kT_0)^{2/b}$ in eqn. 4.7 for $\tau^2 R_0^{-2} h^{2/b} c^{2(b+1)/b} \lambda^{-2/b} X^{-2/b}$ from eqn. 4.3 to obtain

$$f_\nu = 11.2 \text{ Jy} \left(\frac{\tau}{\text{days}}\right)^2 \left(\frac{D}{\text{Mpc}}\right)^{-2} \left(\frac{\lambda}{10^4 \text{ Å}}\right)^{-3} \left(\frac{X}{4}\right)^{-8/3} \cos i. \tag{4.8}$$

Note that the classical thin disc spectrum, $f_\nu \propto \lambda^{-1/3}$, is recovered since $\tau \propto \lambda^{4/3}$, hence $f_\nu \propto \tau^2 \lambda^{-3} \propto \lambda^{-1/3}$; and f_ν is the distribution of flux with frequency ν.

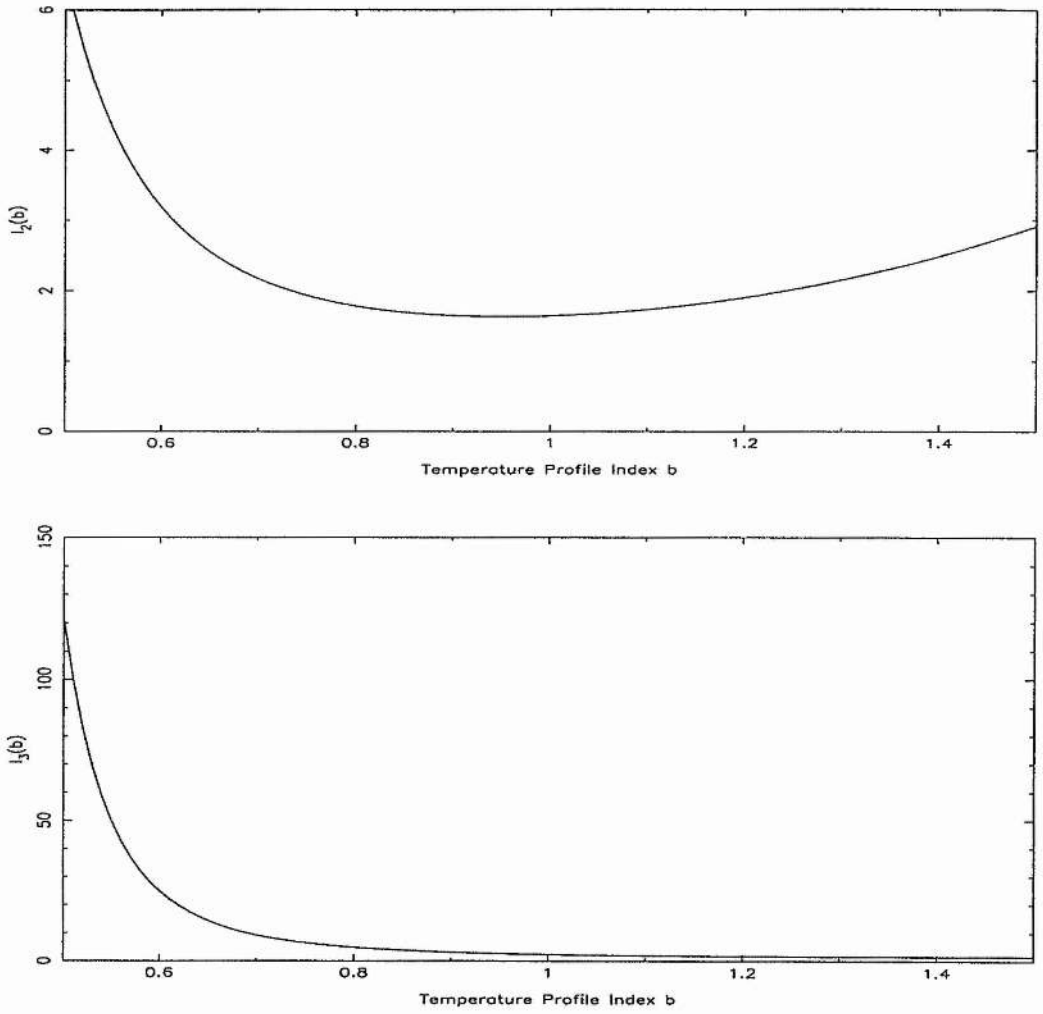

Figure 4.1: Top panel: The numerical evaluation of $I_2(b)$ for a given temperature profile index b (eqn. 4.7). Bottom panel: The numerical evaluation of $I_3(b)$ for a given temperature profile index b.

4.3.5 The Wavelength-dependent Time Delay Disc Transfer Function, $\Psi_\nu(\tau, \lambda)$

The disc *transfer function* $\Psi_\nu(\tau, \lambda)$ describes the responsivity of the gas at a given wavelength and time delay, and is defined by

$$\Psi_\nu(\tau, \lambda) = \int_{R_{\rm in}}^{R_{\rm out}} \int_0^{2\pi} \int_{\tau_{\rm min}}^{\tau_{\rm max}} \frac{\partial B_\nu}{\partial T} \frac{\partial T}{\partial L_{\rm x}} \frac{R dR d\theta \cos i}{D^2} \delta(\tau - (R/c)(1 + \sin i \cos\theta)) d\tau, \quad (4.9)$$

where $L_{\rm x}$ is the high-energy, e.g. X-ray, luminosity that is driving the continuum variations at longer wavelengths, $\tau_{\rm min}$ is the minimum time delay present in the disc, $\tau_{\rm max}$ is the maximum time delay present in the disc, and all other quantities are as previously defined.

The 2D transfer function $\Psi_\nu(\tau, \lambda)$ can be thought of as an "echo image", c.f Welsh & Horne (1991), that relates continuum variations at different wavelengths. Each surface element in an accretion disc model maps directly to a point in the observed wavelength-time delay plane with a weight determined by the responsivity of the gas to small variations in the continuum luminosity.

The observational re–construction of $\Psi_\nu(\tau, \lambda)$ is limited by the quality of the data; requiring extensive high $s : n$ observations with temporal sampling of ≤ 1 day sustained over a baseline of at least several weeks to months. Additionally, the amplitude of the continuum variations should be appreciably larger than the typical measurement errors. The small amplitude of the NGC 7469 continuum variations, §3.2.2, most likely prohibits a full re-construction of $\Psi_\nu(\tau, \lambda)$, but this may be possible with better datasets.

4.3.6 The 1D Wavelength-dependent Time Delay Transfer Functions, $\Psi_\nu(\tau)$ and $\Psi_\nu(\lambda)$.

A 1D transfer function $\Psi_\nu(\tau)$ is realized by integrating the 2D transfer function $\Psi_\nu(\tau, \lambda)$ over wavelength λ, and $\Psi_\nu(\lambda)$ by integrating $\Psi_\nu(\tau, \lambda)$ over time delay τ. We present example transfer functions, $\Psi_\nu(\tau, \lambda)$, for $\lambda = 5000$Å and $\lambda = 8000$Å in Fig. 4.2.

As discussed in §3.3, the cross-correlation of continuum variations for different wavebands estimates the luminosity weighted radius R of the continuum reprocessing region, by measuring the centroid $\tau_{\rm cen}$ of the cross-correlation function (CCF). This gave a 'lag spectrum', Fig. 3.7, that showed that $\tau_{\rm cen}$, and hence R, increased with wavelength λ.

Koratkar & Gaskell (1991) showed that the centroid $\tau_{\rm cen}$ of the CCF is equivalent to the centroid of the transfer function that relates the variations, although see Robinson & Pérez (1990). Hence, by measuring the centroid of the model transfer function $\Psi_\nu(\tau,\lambda)$ for a given wavelength λ, one can then determine the 'lag' between continuum variations at different wavelengths. The centroid $<\tau>$ of $\Psi_\nu(\tau,\lambda)$ for a given λ is given by

$$<\tau>=\frac{\int \tau\Psi_\nu(\tau,\lambda)d\tau}{\int \Psi_\nu(\tau,\lambda)d\tau}, \tag{4.10}$$

or in context (for finite changes in $\Delta L_{\rm x}$),

$$<\tau>=\frac{\int_{R_{\rm in}}^{R_{\rm out}}\int_0^{2\pi}(R/c)(1+\sin i\cos\theta)(B_\nu(T_2)-B_\nu(T_1))(RdRd\theta\cos i)/D^2}{\int_{R_{\rm in}}^{R_{\rm out}}\int_0^{2\pi}(B_\nu(T_2)-B_\nu(T_1))(RdRd\theta\cos i)/D^2}, \tag{4.11}$$

with $T_2=T_{\rm B}(R/R_0)^{-b}$ and $T_1=T_{\rm F}(R/R_0)^{-b}$ describing the bright and faint states of the disc, $\Delta L_{\rm x}\propto(T_{\rm B}^{2/b}-T_{\rm F}^{2/b})$.

Since the $\int_0^{2\pi}\cos\theta=0$, $<\tau>$ becomes

$$<\tau>=\frac{\int_{R_{\rm in}}^{R_{\rm out}}(B_\nu(T_2)-B_\nu(T_1))(R^2/c)dR}{\int_{R_{\rm in}}^{R_{\rm out}}(B_\nu(T_2)-B_\nu(T_1))(RdR)}. \tag{4.12}$$

Adopting the substitutions $y=R/R_0$, $s=s_0y^b$ and $\varepsilon=(T_{\rm F}/T_{\rm B})^{2/b}$, it follows $y^2dy=s_0^{-3/b}s^{3/b-1}ds/b$ and

$$<\tau>=\frac{R_0}{c}\left(\frac{\lambda kT_B}{hc}\right)^{1/b}\frac{I_3(b)}{I_2(b)}\frac{1-\varepsilon^{3/2}}{1-\varepsilon}. \tag{4.13}$$

The centroid of $\Psi_\nu(\tau,\lambda)$ for a given λ, determines a 'lag' $<\tau>$ that can be compared with the observed 'lag' $\tau_{\rm cen}$, §3.3.4. As expected $\tau_{\rm cen}\equiv<\tau>\propto\lambda^{4/3}$ with $T\propto R^{-3/4}$. The 'lag' $<\tau>$ reflects the average time delay distribution determined from the bright and faint state flux distributions, i.e $T_0=T_{\rm B}$ and $T_{\rm F}$ respectively (see §4.3.3 and §4.3.9), assuming that b is the same in the bright and faint states.

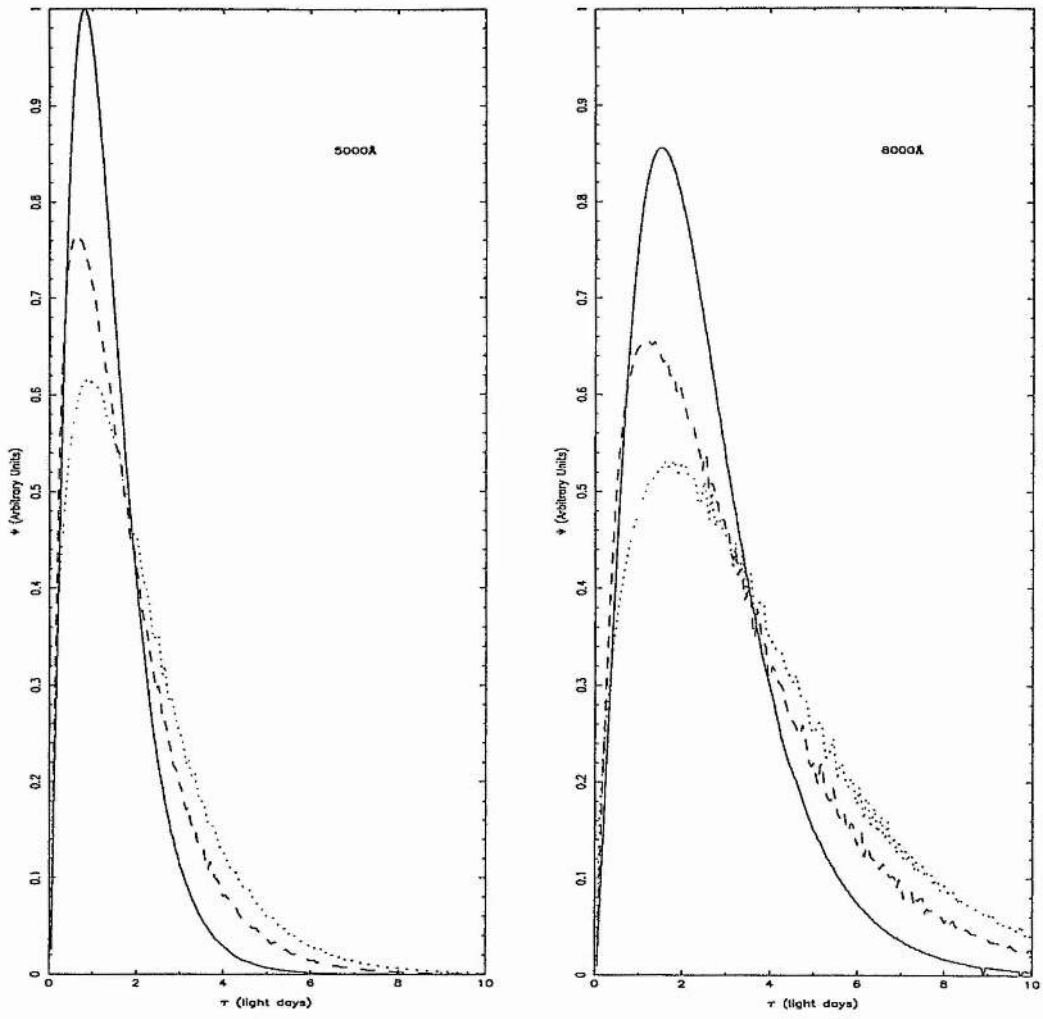

Figure 4.2:

Illustrative transfer functions $\Psi_\nu(\tau, \lambda)$ for $\lambda = 5000$Å (left panel) and $\lambda = 8000$Å (right panel), $T_B = 7749$ K, $T_F = 6519$ K, distance $D \approx 117$ Mpc, and inclinations $i = 0°$, $i = 45°$, and $i = 90°$ denoted by the solid, dashed, and dotted lines respectively. The transfer functions are normalized relative to the 5000Å transfer function with $i = 0°$. The centroid of the transfer function increases with wavelength, see Fig. 4.3, with the longer wavelength response less coherent, occurring over a larger range of time delays. The width of the transfer function is a function of the disc inclination, with it becoming broader with increasing i. However, the close similarity of transfer functions for different i's and a given λ, probably preclude the derivation of i from the observed transfer functions.

In Fig. 4.3 we present wavelength-dependent time delays, eqn. 4.13, for different temperature profile indices, confirming $< \tau > \propto \lambda^{1/b}$.

4.3.7 Bright, Faint, and Difference Spectra

Following §4.3.4 the bright state spectrum is given by

$$f_\nu^{\rm B} = \frac{4\pi R_0^2 \cos i}{D^2} (hc)^{1-2/b} \lambda^{2/b-3} (kT_B)^{2/b} \frac{I_2(b)}{b}. \tag{4.14}$$

One can substitute $(kT_{\rm B})^{2/b}$ in eqn. 4.14 for $< \tau >^2$ $(c/R_0)^2 (hc/\lambda)^{2/b} (I_2(b)/I_3(b))^2 (1 - \varepsilon/1 - \varepsilon^{3/2})^2$ from eqn. 4.13 to obtain

$$f_\nu^{\rm B} = \frac{4\pi \cos i}{D^2} hc^3 \lambda^{-3} < \tau >^2 \frac{I_2(b)^3}{I_3(b)^2 b} \left(\frac{1-\varepsilon}{1-\varepsilon^{3/2}} \right)^2. \tag{4.15}$$

The faint state spectrum is given by

$$f_\nu^{\rm F} = \frac{4\pi R_0^2 \cos i}{D^2} (hc)^{1-2/b} \lambda^{2/b-3} (kT_F)^{2/b} \frac{I_2(b)}{b}. \tag{4.16}$$

It can be shown that

$$f_\nu^{\rm F} = (T_{\rm F}/T_{\rm B})^{2/b} f_\nu^{\rm B} = \varepsilon f_\nu^{\rm B}, \tag{4.17}$$

where $\varepsilon = (T_{\rm F}/T_{\rm B})^{2/b}$.

Hence the difference spectrum, that is the change in the disc spectrum between the bright and faint states, is given by

$$\Delta f_\nu = f_\nu^{\rm B} - f_\nu^{\rm F} = \frac{4\pi \cos i}{D^2} hc^3 \lambda^{-3} < \tau >^2 \frac{1}{b} \frac{(I_2(b)(1-\varepsilon))^3}{(I_3(b)(1-\varepsilon^{3/2}))^2}. \tag{4.18}$$

Fig. 4.4 presents a selection of difference spectra based on generic disc models with power-law temperature profiles, $T = T_0 (R/R_0)^{-b}$, $T_2 = T_{\rm B}(R/R_0)^{-b2}$ and $T_1 = T_{\rm F}(R/R_0)^{-b1}$. We have fixed $T_0 = 7314$ K, $T_{\rm B} = 7314$ K, $T_{\rm F} = 6905$ K, distance $D \approx 98$ Mpc, and inclination $i = 45°$. The top-left panel presents a difference spectrum with $b = 3/4$, and shows $f_\nu \propto \lambda^{-1/3}$. The top-right panel presents difference spectra with $b = 1/2$ and $b = 1$,

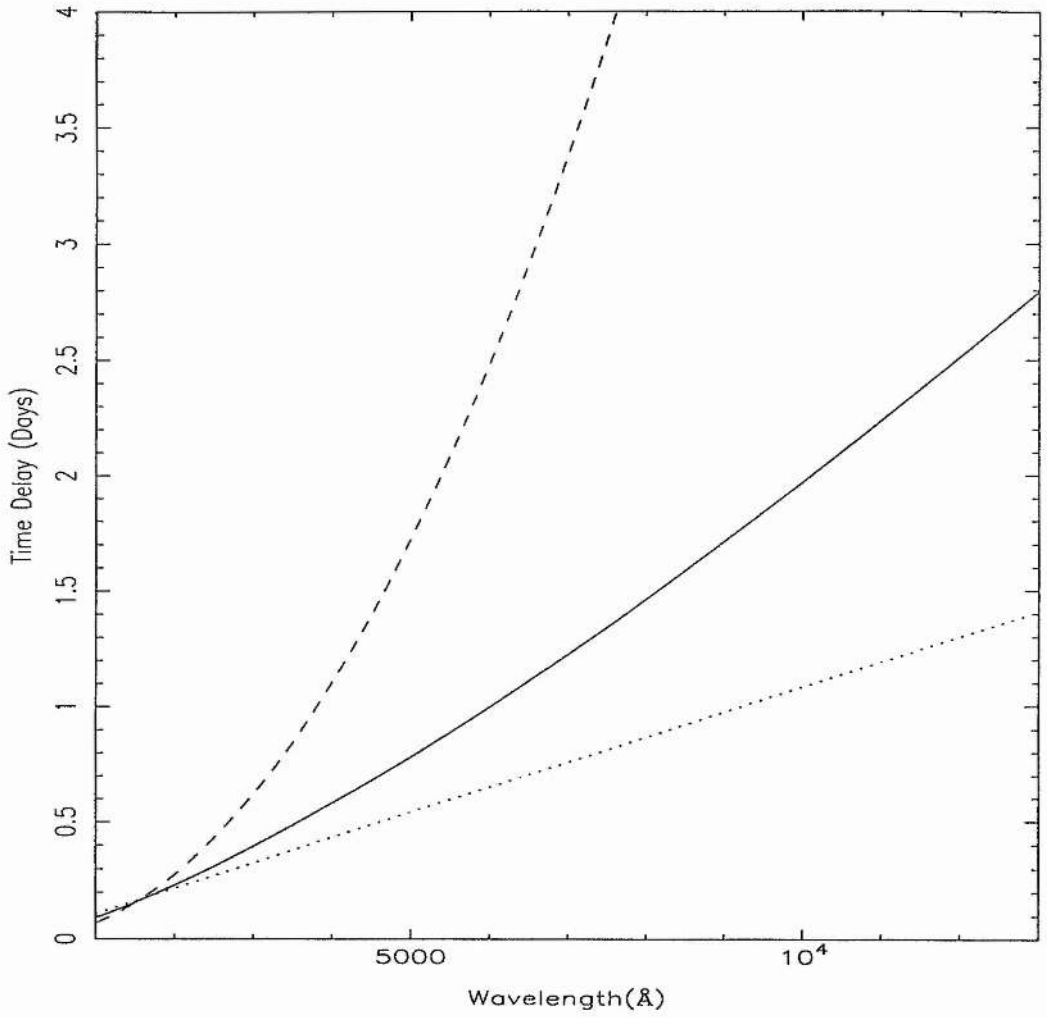

Figure 4.3: Wavelength-dependent time delays for temperature profile indices $b = 0.5$, $b = 0.75$ and $b = 1$ denoted by the dashed, solid and dotted lines respectively ($T_{\rm B} = 7314$ K : $T_{\rm F} = 6905$ K). The shallowness of the temperature profile represented by the dashed line translates to the steepest wavelength-dependent time delay, with a time delay of about 2 light days between the continuum variations at 4000 Å and 7000 Å, c.f about 0.5 light day for the steepest temperature profile represented by the dotted line.

represented by the solid and dotted lines respectively. This illustrates that $T \propto R^{-b}$ structures result in $f_\nu \propto \lambda^{2/b-3}$ distributions, hence de-reddened nuclear spectra will sense the temperature structure of the disc. The bottom-left panel represents a spectrum with the bright and faint state spectra due to a non-linear combination of two temperature profiles with $b2 = 3/4$ and $b1 = 1/2$. The shape of the difference spectrum is determined by the relative prominence of the individual temperature structures present. Similarly, the bottom-right panel represents a spectrum with the bright and faint state spectra due to a non-linear combination of two temperature profiles with $b2 = 3/4$ and $b1 = 1$. It is obvious that the shape of the spectral energy distribution will be influenced by the temperature structure of the disc.

4.3.8 Determination of the Distance D and the Hubble Constant H_0

Using eqn. 4.8 the redshift-independent distance D to the AGN is simply derived to be

$$D = 3.3 \text{ Mpc} \left(\frac{\tau}{\text{days}}\right) \left(\frac{\lambda}{10^4 \text{ Å}}\right)^{-3/2} \left(\frac{f_\nu / \cos i}{\text{Jy}}\right)^{-1/2} \left(\frac{X}{4}\right)^{-4/3}. \qquad (4.19)$$

By inserting observed values of $\tau(\lambda)$ and f_ν into the above equation, a redshift-independent distance to the object is derived. Hubble's constant, $H_0 = cz/D$, is then,

$$H_0 = 89.6 \left(\frac{\text{kms}^{-1}}{\text{Mpc}}\right) \left(\frac{\lambda}{10^4 \text{Å}}\right)^{3/2} \left(\frac{z}{0.001}\right) \left(\frac{\tau}{\text{day}}\right)^{-1} \left(\frac{f_\nu / \cos i}{\text{Jy}}\right)^{1/2} \left(\frac{X}{4}\right)^{4/3}, \qquad (4.20)$$

where $z \ll 1$ is the redshift of the AGN.

Since, the difference spectrum cancels any starlight contamination and gives a lower limit to the nuclear spectrum, §4.4, it is more appropriate to derive the redshift-independent distance from the difference spectrum. This gives

$$D = \left(\frac{4\pi \cos i}{\Delta f_\nu}\right)^{1/2} h^{1/2} c^{3/2} \lambda^{-3/2} < \tau > (1/b)^{1/2} \frac{(I_2(b)(1-\varepsilon))^{3/2}}{(I_3(b)(1-\varepsilon^{3/2}))}. \qquad (4.21)$$

The above equation is equivalent to eqn. 4.19 with $b = 0.75$, and may be re-arranged to derive a similar expression, eqn. 4.20, for the Hubble constant.

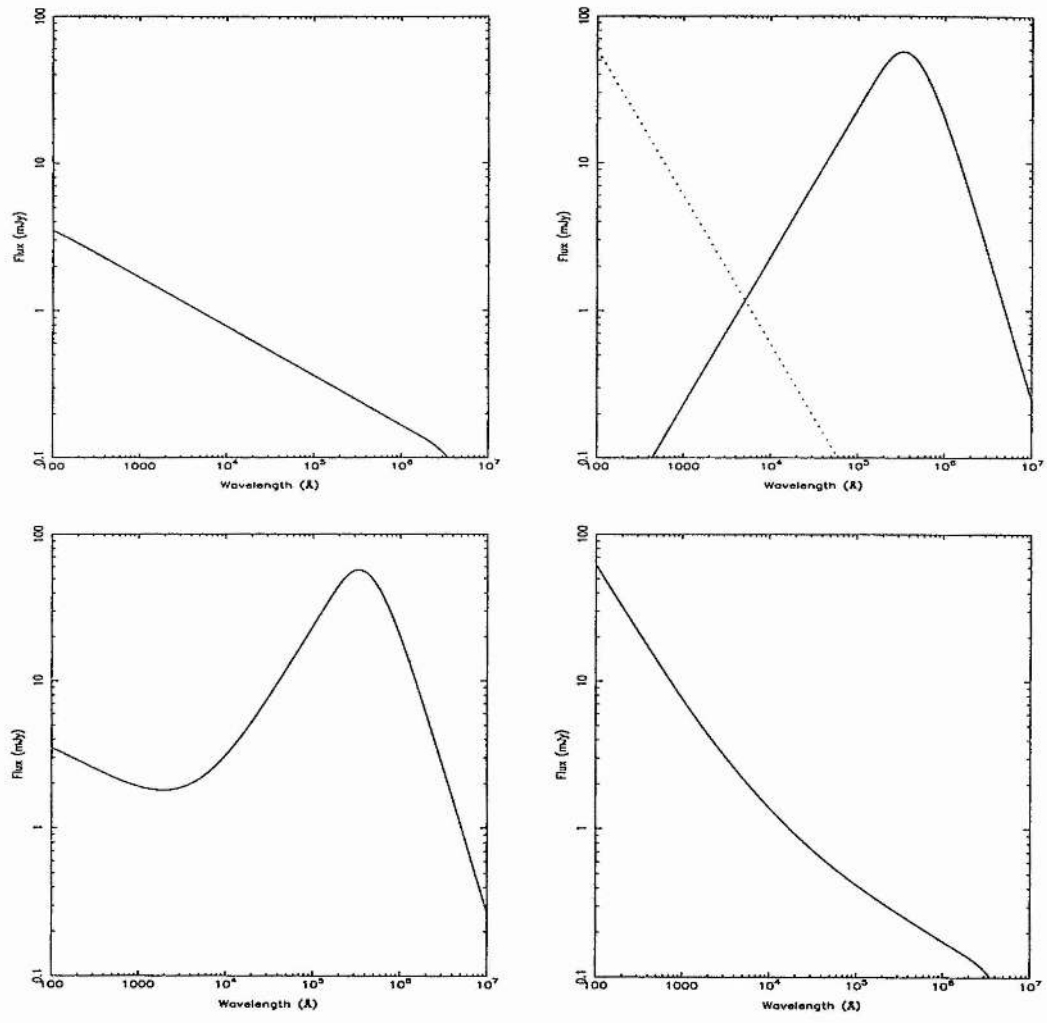

Figure 4.4: A selection of difference spectra based on generic accretion disc models with power-law temperature profiles. Top-left panel, $T \propto R^{-b}$ with $b = 3/4$. Similarly, top-right panel with $b = 1/2$ (solid line) and $b = 1$ (dashed line). Bottom panels present difference spectra with bright and faint state spectra due to a non-linear combination of two temperature profiles. Bottom-left panel, $T_2 \propto R^{-b2}$ and $T_1 \propto R^{-b1}$ with $b2 = 3/4$ and $b1 = 1/2$. Similarly, bottom-right panel, with $b2 = 3/4$ and $b1 = 1$. See text for details.

4.3.9 The Blackbody Model: X

As previously mentioned, §4.3.3, the parameter X embodies the blackbody approximation and appears in the initially derived expressions for the wavelength-dependent time delay (§4.3.3), disc spectrum (§4.3.4), distance determination and Hubble constant estimate (§4.3.8). Our new expression for D (eqn. 4.21) does not depend on X. The value of X is determined by matching the observed $T(R)$ given by $\tau(\lambda)$ with that expected from the Wien Law. Additional physical insight into X is achieved by comparing eqn. 4.3 with eqn. 4.15, and using eqn. 4.14 to solve for X. This gives

$$X_{\rm B} = \left(\frac{I_3(b)}{I_2(b)} \frac{1-\varepsilon^{3/2}}{1-\varepsilon} \right)^b , \tag{4.22}$$

where all quantities have been previously defined. $X_{\rm B}$ is determined by the bright and faint state temperatures of the disc at $R_0 = 1$ light day, and the temperature profile index b. The subscript B on X, eqn. 4.22, denotes that we have used the time delay distribution defined by the bright state flux distribution. In a similar fashion, it can be shown that $X_{\rm F} = \varepsilon^{-b/2} X_{\rm B}$, hence, $X_{\rm F} > X_{\rm B}$. It remains unclear how the observed time delays relate to the time delay distributions predicted by the bright and faint state flux distributions. We assume that the observed time delays reflect the average time delay distribution, as derived from the bright and faint state flux distributions.

In Fig. 4.5 we show the variation of $X_{\rm B}$ with temperature profile index b for $T_{\rm B} = 7314$ K and $T_{\rm F} = 6905$ K. Inferred temperatures depend on X, but distances do not.

4.4 First Application of the Method to the NGC 7469 Monitoring Campaign Data

To apply the new method we use data from a seven-week International AGN Watch multi-wavelength monitoring campaign on NGC 7469, $z = 0.0164$, which showed optical

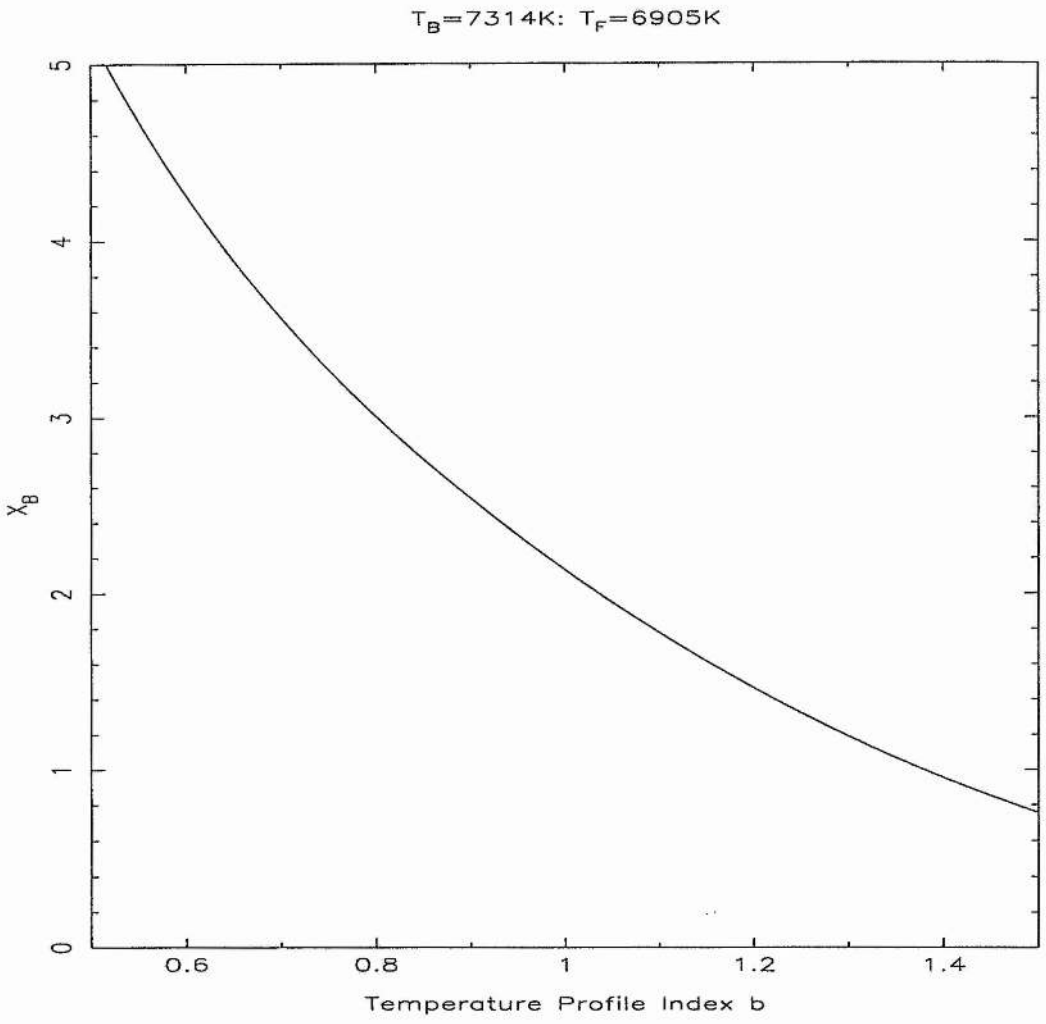

Figure 4.5: The variation of X_{B} with temperature profile index b ($T_{\mathrm{B}} = 7314$ K and $T_{\mathrm{F}} = 6905$ K). For $b = 0.75$, X_{B} is about 3.2.

continuum variations lagging behind those in the UV by about 1 day at 4800Å and about 2 days at 7500Å (Wanders et al. (1997) and Collier et al. (1998)). These UV/optical continuum lags have been shown to be statistically significant at no less than 97% confidence (Peterson et al. (1998)). The measured time delay between the flux variations at wavelength λ and those at wavelength 1315Å is shown in the top panel of Fig. 4.6. The observed time delays are encompassed by the $\tau \propto \lambda^{4/3}$ predictions, shown as dashed and dotted lines, for irradiated blackbody accretion disc models with $T = T_0(R/R_0)^{-3/4}$ structure, with $T_0 \approx 6500$ K and $T_0 \approx 7700$ K respectively. The observed delays increase above the overall trend at wavelengths near emission lines. Here there is a mix of continuum and line flux, the lines responding with larger delays than the continuum light. The horizontal axes in Fig. 4.6 give for each wavelength λ the corresponding temperature T in the disc. The temperature is calculated assuming $T = hc/k\lambda X$, with $X = 3.89$ being appropriate for black body discs with $T \propto R^{-3/4}$ as indicated by numerical simulations, §4.3.9.

The bottom panel of Fig. 4.6 compares the de-reddened UV/optical maximum, minimum and difference spectra of the NGC 7469 monitoring campaign with predicted spectra for $H_0 = 42$ km s^{-1} Mpc^{-1} ($D \approx 117$ Mpc) based on the irradiated accretion disc model inclined at $i = 45°$ to the observer's line-of-sight. The dotted and dashed lines represent model spectra for bright and faint states of the irradiated accretion disc, and define maximum and minimum temperatures, $T_B \approx 7700$ K and $T_F \approx 6500$ K, at radius $R_0 = 1$ light day respectively. The brightest and faintest spectra seen during the NGC 7469 campaign are both much redder than the predicted disc spectra. This is caused by contamination of the observed spectra by a red starlight component from the host galaxy. We therefore consider these spectra to be upper limits to the spectrum of the active nucleus. The solid line represents the predicted difference spectrum between the bright and faint states of

the disc. This agrees approximately with the difference spectrum between the brightest and faintest spectra recorded in the NGC 7469 AGN Watch campaign. The difference spectrum, which cancels any starlight contamination, gives a lower limit to the nuclear spectrum.

The results shown in Fig. 4.6 demonstrate that the observed variability in the continuum spectrum of NGC 7469 is in approximate agreement with a blackbody disc, $T \propto R^{-0.75}$, and $H_0 \, (\cos i)^{1/2} = 35 \pm 6 \, \mathrm{km\,s^{-1}\,Mpc^{-1}}$. The error-bars reflect statistical uncertainties in the measured fluxes f_ν and time delays τ, e.g. equation 4.8. The point-to-point scatter in the continuum time delays allows us to assign a 10% uncertainty to the time delay measurements. A lower limit to the flux of the nucleus, is $\Delta f_\nu = 3.5 \pm 1.0$ mJy at $\lambda = 1315$Å. The 10% uncertainty in τ and 29% uncertainty in Δf_ν result in a 17% uncertainty in $H_0 \, (\cos i)^{1/2}$.

4.5 Systematic Errors

The estimate of H_0 is subject to several systematic errors.

4.5.1 Reddening of Spectra by Dust

The AGN spectrum is diminished and reddened by intervening dust. The amount of extinction (in magnitudes), a_λ, is approximately equal to the optical depth, τ_λ, along the observer's line-of-sight. By assuming the dust scattering cross-section, σ_λ, is constant along the line-of-sight, it can be shown that $a_\lambda \simeq \tau_\lambda = \sigma_\lambda N_\mathrm{d}$, where N_d is the dust column density.

Mie scattering theory shows that for wavelength $\lambda \approx a$, with a the radius of a spherical dust grain, $a_\lambda \propto \lambda^{-1}$. Hence, blue light is preferentially scattered out of the observer's line-of-sight, causing the AGN to appear redder than its effective temperature would otherwise

continuum variations lagging behind those in the UV by about 1 day at 4800Å and about 2 days at 7500Å (Wanders et al. (1997) and Collier et al. (1998)). These UV/optical continuum lags have been shown to be statistically significant at no less than 97% confidence (Peterson et al. (1998)). The measured time delay between the flux variations at wavelength λ and those at wavelength 1315Å is shown in the top panel of Fig. 4.6. The observed time delays are encompassed by the $\tau \propto \lambda^{4/3}$ predictions, shown as dashed and dotted lines, for irradiated blackbody accretion disc models with $T = T_0(R/R_0)^{-3/4}$ structure, with $T_0 \approx 6500$ K and $T_0 \approx 7700$ K respectively. The observed delays increase above the overall trend at wavelengths near emission lines. Here there is a mix of continuum and line flux, the lines responding with larger delays than the continuum light. The horizontal axes in Fig. 4.6 give for each wavelength λ the corresponding temperature T in the disc. The temperature is calculated assuming $T = hc/k\lambda X$, with $X = 3.89$ being appropriate for black body discs with $T \propto R^{-3/4}$ as indicated by numerical simulations, §4.3.9.

The bottom panel of Fig. 4.6 compares the de-reddened UV/optical maximum, minimum and difference spectra of the NGC 7469 monitoring campaign with predicted spectra for $H_0 = 42$ km s^{-1} Mpc^{-1} ($D \approx 117$ Mpc) based on the irradiated accretion disc model inclined at $i = 45°$ to the observer's line-of-sight. The dotted and dashed lines represent model spectra for bright and faint states of the irradiated accretion disc, and define maximum and minimum temperatures, $T_B \approx 7700$ K and $T_F \approx 6500$ K, at radius $R_0 = 1$ light day respectively. The brightest and faintest spectra seen during the NGC 7469 campaign are both much redder than the predicted disc spectra. This is caused by contamination of the observed spectra by a red starlight component from the host galaxy. We therefore consider these spectra to be upper limits to the spectrum of the active nucleus. The solid line represents the predicted difference spectrum between the bright and faint states of

the disc. This agrees approximately with the difference spectrum between the brightest and faintest spectra recorded in the NGC 7469 AGN Watch campaign. The difference spectrum, which cancels any starlight contamination, gives a lower limit to the nuclear spectrum.

The results shown in Fig. 4.6 demonstrate that the observed variability in the continuum spectrum of NGC 7469 is in approximate agreement with a blackbody disc, $T \propto R^{-0.75}$, and $H_0 (\cos i)^{1/2} = 35 \pm 6\,\mathrm{km\,s^{-1}\,Mpc^{-1}}$. The error-bars reflect statistical uncertainties in the measured fluxes f_ν and time delays τ, e.g. equation 4.8. The point-to-point scatter in the continuum time delays allows us to assign a 10% uncertainty to the time delay measurements. A lower limit to the flux of the nucleus, is $\Delta f_\nu = 3.5 \pm 1.0$ mJy at $\lambda = 1315$Å. The 10% uncertainty in τ and 29% uncertainty in Δf_ν result in a 17% uncertainty in $H_0 (\cos i)^{1/2}$.

4.5 Systematic Errors

The estimate of H_0 is subject to several systematic errors.

4.5.1 Reddening of Spectra by Dust

The AGN spectrum is diminished and reddened by intervening dust. The amount of extinction (in magnitudes), a_λ, is approximately equal to the optical depth, τ_λ, along the observer's line-of-sight. By assuming the dust scattering cross-section, σ_λ, is constant along the line-of-sight, it can be shown that $a_\lambda \simeq \tau_\lambda = \sigma_\lambda N_\mathrm{d}$, where N_d is the dust column density.

Mie scattering theory shows that for wavelength $\lambda \approx a$, with a the radius of a spherical dust grain, $a_\lambda \propto \lambda^{-1}$. Hence, blue light is preferentially scattered out of the observer's line-of-sight, causing the AGN to appear redder than its effective temperature would otherwise

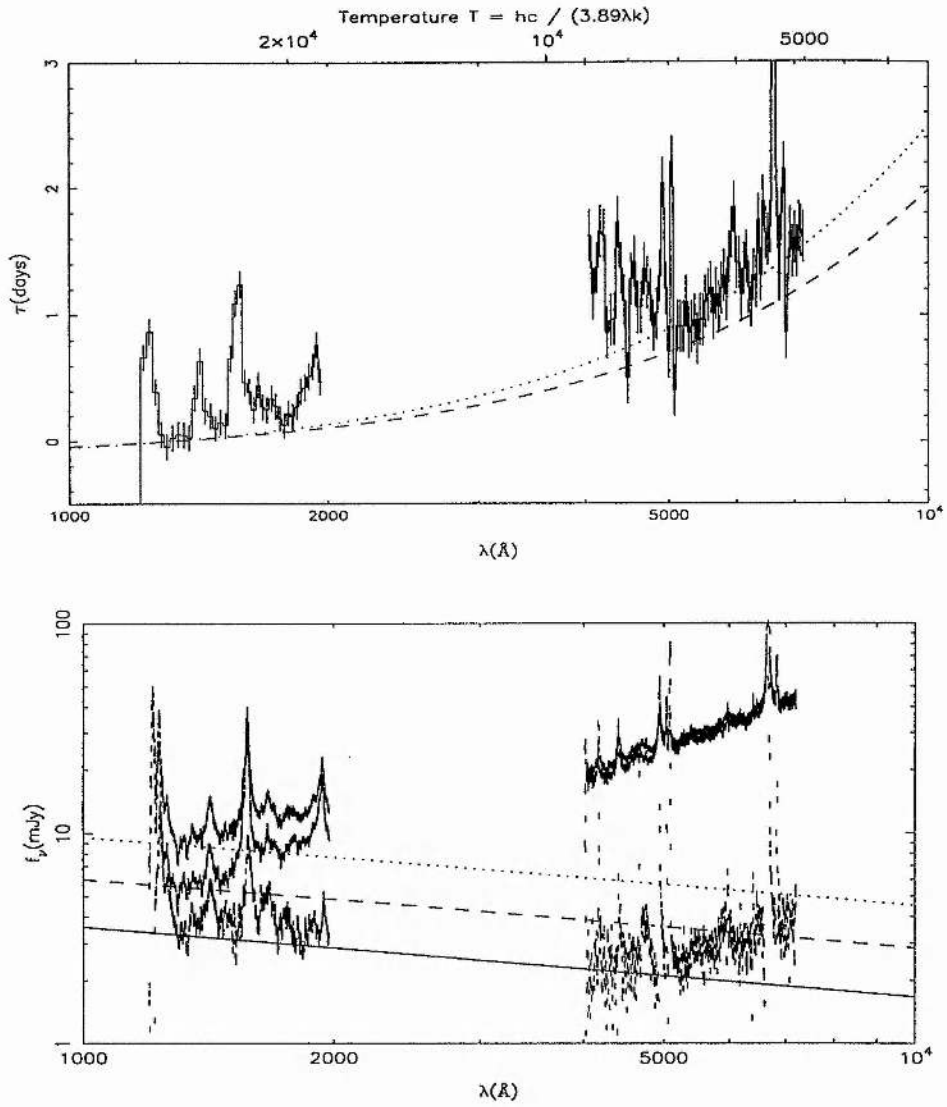

Figure 4.6: Top Panel: The predicted time delays for the irradiated accretion disc model are compared with the observed time delays, measured relative to 1315Å. The time delay increases above the overall trend near the emission lines because here there is a mix of continuum and line flux. The lines respond with longer time delays and this results in a larger net delay. Bottom panel: Model spectra for an irradiated accretion disc (assuming $H_0 = 42\,\mathrm{km\,s^{-1}\,Mpc^{-1}}$ and $i = 45°$) are compared with observed spectra of NGC 7469 from the 1996 AGN Watch multi-wavelength monitoring campaign. See text for details.

imply.

The exact location of the dust is unknown, with galactic, intergalactic, internal to the AGN host galaxy, or internal to the AGN all distinct possibilities. Numerous methods for evaluating the amount of dust extinction are employed. Pointed 21cm observations relate the neutral Hydrogen column density $N_{\rm H}$ to τ_λ, and give $E(B-V) \approx 0.074 - 0.096$ for NGC 7469 (Elvis et al. (1989) and Lockman & Savage (1995)). Estimates based on the strength of the 2200 Å dust absorption feature give $E(B-V) \approx 0.14$ (Westin (1985)). We have corrected our spectra, Fig. 4.6, with the standard reddening law of Seaton (1979), using $E(B-V) = 0.14$. Other methods include; Balmer decrement measurements and the strength of X-ray absorption features. A more complete discussion of the methods, and their relative strengths and weaknesses is discussed by Mathis (1990) and references therein. We note reddening corrections based on the strength of the 2200Å absorption feature can be spurious given the low resolution of IUE spectra and the presence of Fe II lines long-ward of 2200Å.

4.5.2 The Host-galaxy Contamination

The host-galaxy contamination can be estimated from off-nuclear observations of the host galaxy, e.g using HST or ground based adaptive optics. In the difference spectra the host-galaxy contamination is negligible. The red slope of the mean spectrum is due to contamination by starlight from the host galaxy, which contributes at least $\approx$ 40% at 5400Å in a circular 10 arcsecond radius aperture (Malkan & Filippenko (1983)). Recently, Welsh et al. (1998) used HST observations of NGC 7469, taken during the same monitoring campaign, to show that the percentage host galaxy contamination approached 80% of the total flux at 7000Å, see Fig. 3.3.

4.5.3 The Disc Inclination i

A systematic error arises from uncertainty in $(\cos i)^{1/2}$. However, the inclination uncertainty is probably not a major obstacle, see Fig. 4.7. According to unified schemes (Antonucci (1993) and Hes et al. (1993)), Seyfert I galaxies, in which we see the broad emission line region (BLR), have $i \leq 60°$, while Seyfert II galaxies, in which the BLR is obscured by a dusty torus, have $i \geq 60°$. For $i < 60°$, $(\cos i)^{1/2} > 0.7$. By adopting $i = 45°$, $(\cos i)^{1/2} = 0.84$, we commit a maximum error of $\pm 17\%$, and an RMS error of $\pm 11\%$ (assuming the disc i is randomly oriented, so $\cos i$ is uniformly distributed between 0 and 1). Averaging over 10 objects could reduce this by a factor $\sqrt{10}$ to $\pm 3.5\%$. With $(\cos i)^{1/2} = 0.84 \pm 0.1$ we find $H_0 = 42 \pm 9\,\mathrm{km\,s^{-1}\,Mpc^{-1}}$.

The echo mapping method in principle allows us to derive the inclination i, because the width of the time delay distribution at each wavelength is a function of i. However, referring to Fig. 4.2, this is likely to be extremely difficult. This method may be applied, in future, to NGC 7469 and other Seyfert I galaxies. Fits to the profile of the X-ray Fe Kα line in MCG-6-30-15 (Tanaka et al. (1995)) yielded a disc inclination $i = 30 \pm 3°$. Similar observations of an X-ray Fe Kα line in NGC 7469 may therefore measure i with about 10% accuracy. It may also be possible to determine i from polarization measurements, Kartje (1995). Therefore there are good prospects for measuring inclinations of individual AGNs.

4.5.4 The Blackbody Model

The blackbody model is a source of systematic uncertainty. The value $X = 3.89$ relies on the assumption that the changes in the UV/optical continuum can be modelled as irradiation of a blackbody disc with $T \propto R^{-3/4}$. This is justified by the approximate agreement of the predicted $f_\nu \propto \lambda^{-1/3}$ spectrum with the observed difference spectrum. This can be further investigated by considering models of the vertical structure and the

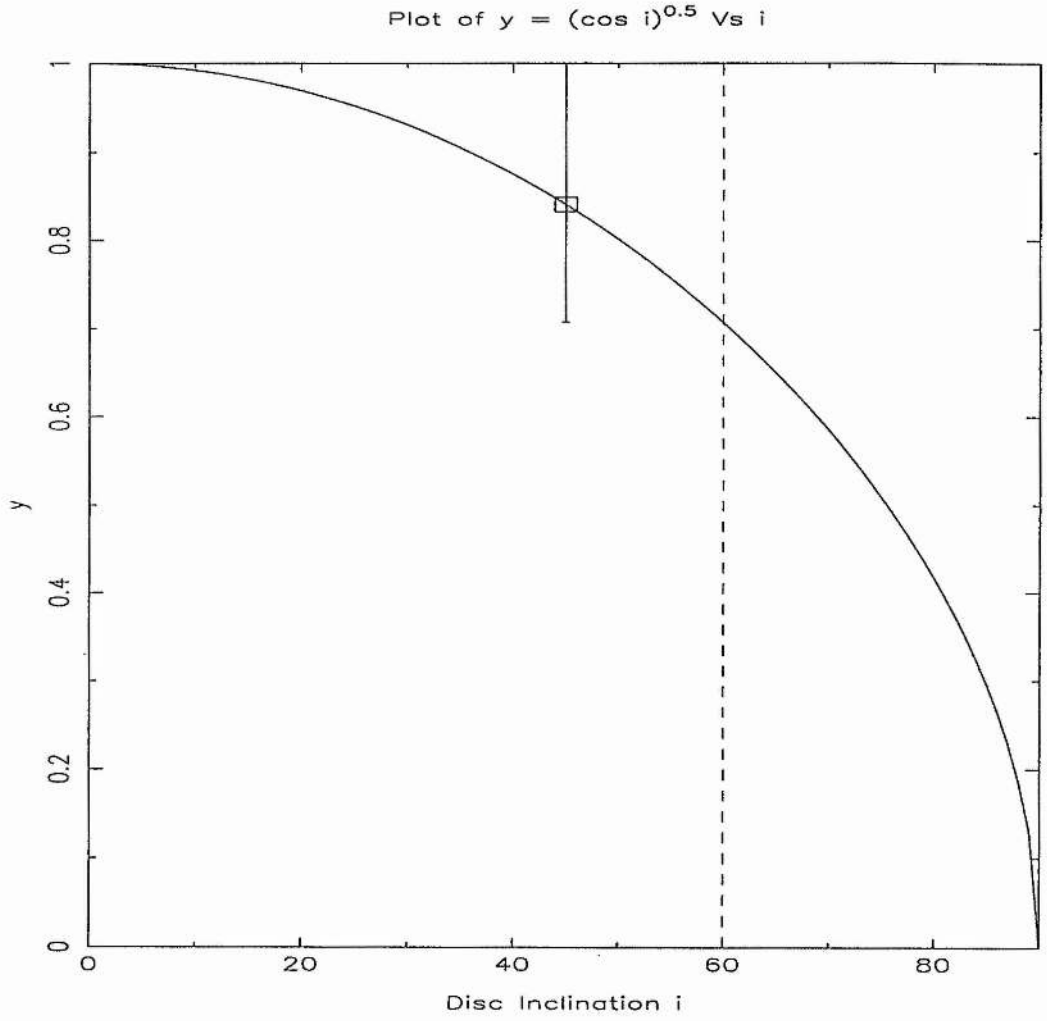

Figure 4.7: The variation of $(\cos i)^{0.5}$ with i. Unified schemes of AGN suppose Seyfert I galaxies have $i < 60°$ ($i = 60°$ is represented by the dashed line). By adopting $i = 45°$ one commits a maximum error of $\pm 17\%$, because $(\cos i)^{0.5}$ is a slow function of i for $i < 60°$. This is reflected by the data-point and its error-bar.

emitted spectra of irradiated accretion disc atmospheres, Sincell & Krolik (1997). Their models predict an UV spectral shape that may be consistent with the observations, but a Lyman edge emission feature that is not observed.

To first order the method of measuring distances should be insensitive to limb darkening (Hubeny et al. (1997)). First, the irradiation of the disc will flatten the temperature versus optical depth relationship in the atmosphere and conspire to reduce the limb darkening effect. Second, the lower temperatures observed at high inclinations will change the apparent $T(R)$ profile, but the same blackbody relationship will describe the relationship between surface brightness and wavelength that our method needs to compute the predicted flux. Hence, while the $T(R)$ profile is sensitive to limb darkening the inferred surface brightness and subsequent distance is not.

4.5.5 The Source Geometry and Nature of the Continuum Variations

Another source of systematic uncertainty is the source geometry and nature of the continuum variations. The reprocessing geometry considered thus far might be completely ruled out by the recent X-ray observations of NGC 7469 (Nandra et al. (1998)). The 2-10 KeV X-ray variations are poorly correlated or uncorrelated with the UV/optical variations described here. Either (a) the accretion disc sees different X-ray variations than we do, (b) the UV/optical variations are driven by another unobserved part of the spectrum, e.g. the extreme UV, or (c) the model geometry is completely wrong.

As is apparent, neither the nature or origin of the driving continuum variations is clearly defined. This remains a major uncertainty in our method, and can lead to a slight underestimation of the size of the emission region at a particular wavelength. In §4.4 we have normalized our predicted time delays to account for this effect, given the model assumptions of §4.3. Future simultaneous multi-wavelength experiments are required to

address the above issue, and determine the relative importance of these various systematic effects.

4.6 Model fits to the Data

The estimate of the Hubble constant, $H_0 = 42 \pm 9 \mathrm{km\,s^{-1}\,Mpc^{-1}}$ in §4.4 was based on the following disc parameters; $T_{\mathrm{B}} = 7753$ K, $T_{\mathrm{F}} = 6519$ K, $b = 0.75$, $E(B-V) = 0.14$, and $i = 45°$. We excluded regions of dominant line emission from the observed time delays and difference spectrum, Fig. 4.6, to formally fit the model to the data. The goodness-of-fit χ^2 statistic was found to be 874 for 302 degrees of freedom. The reduced χ^2_ν of the fit was 2.9. This may imply that the uncertainties in our H_0 estimate are underestimated and/or (as is most likely) the 'fit-by-eye' estimate is not the 'best fitting' model to the observational data.

In order to validate or otherwise the 'fit-by-eye' results presented in §4.4, the generic disc model is fitted to the data using a χ^2 minimization algorithm, i.e. a downhill simplex method (amoeba routine), e.g. Press et al. (1992). Our problem is defined by the bright and faint state temperatures, T_{B} and T_{F}, at 1 light day, the distance D to the AGN or the Hubble constant H_0, and the temperature profile index b ($T \propto R^{-b}$). The adopted $E(B-V)$ value and disc inclination i must also be considered.

The aforementioned parameters are used to fit a blackbody accretion disc model to the observed data, i.e the difference spectrum and time delays only (since the maximum and minimum spectra contain an unknown wavelength-dependent contribution from the underlying host galaxy). A number of constraints are imposed during the fitting procedure to limit the allowable range in parameter space. We adopt a brute-force method for the imposition of constraints. The predicted disc spectra are calculated for a given set of parameters, and if the flux constraints, detailed below, are violated an arbitrarily high

value of χ^2 is returned impeding the algorithms progress.

The adopted constraints are as follows: The predicted bright state flux at 1306Å must not be larger than the observed bright state flux (allowing for the 3-σ error on the observed flux measurement). Similarly, the faint state flux must be less than the observed faint state flux. The predicted contaminating galaxy contribution, defined by the difference between the predicted and observed bright state fluxes at 1306Å, must be less than the observed faint state flux at 1306Å, and finally, we adopted a conservative fiducial maximum allowed galaxy contamination value at 1306Å, defined to be 25% of the observed faint state flux, in order to reasonably constrain the predicted bright and faint state nuclear fluxes. Welsh et al. (1998) estimates the host galaxy + starburst light contribution, to the IUE spectra, ranges from $\sim$ 0% at 1300Å to $\sim$ 15% at 1850Å, thus partially justifying the latter assumption.

We found that if the galaxy contribution was not constrained in some reasonable fashion (i.e if the only constraints were the bright and faint states had to be less than those observed and the galaxy contribution less than the observed faint state flux at 1306Å), the permitted range of H_0 values was large, i.e $H_0 \sim 15{-}40\,\mathrm{km\,s^{-1}\,Mpc^{-1}}$, for $E(B{-}V) = 0.14$ and $i = 45°$. This is because there is a range of $T_{\rm B}$, $T_{\rm F}$, and H_0 that fit the observed difference spectrum and time delays equally well, on account of the poor constraints on the bright and faint state fluxes. The lower values for H_0 imply galaxy contaminations of $\sim$ 90% of the observed faint state flux, with the higher H_0 values requiring progressively smaller galaxy contamination levels. We note, for a normal Sab galaxy $\sim$ 4% of the light at 2688Å would be due to starlight, Edelson et al. (1996). However, it is possible that the stellar spectral energy distribution of AGN are not well approximated by those of normal galaxies, given, for example, enhanced star formation activity would result in a larger UV stellar contribution.

A single implementation of the amoeba algorithm with four, $T_{\rm B}$, $T_{\rm F}$, b, and H_0, free parameters ($E(B-V) = 0.14$ and $i = 45°$) gives $H_0 = 41$ km s^{-1} Mpc^{-1}, $T_{\rm B} = 8514$ K, $T_{\rm F} = 7233$ K, and $b = 0.73$. The reduced χ^2_ν of the fit is 1.35 for 302 degrees of freedom. A similar fit with $E(B-V) = 0.0$ gives $H_0 = 40$ km s^{-1} Mpc^{-1}, $T_{\rm B} = 7286$ K, $T_{\rm F} = 6121$ K, $b = 0.61$, and $\chi^2_\nu = 1.35$. We note a reasonably good fit to the data is indicated by $\chi^2_\nu \approx 1$, provided the error estimates are realistic. We conclude, from a visual inspection, that both solutions are reasonable fits to the data.

It is immediately clear that there is a strong correlation between the reddening, i.e $E(B-V)$, and the temperature profile index b which determines the slope, α, of the difference spectra (see §4.3), i.e $\alpha = 2/b - 3$. Explicitly, for larger values of $E(B-V)$, larger values of b are required, and vice versa. At first sight the model fits suggest the Hubble constant or distance D to the AGN is insensitive to the reddening. The dust serves to make the disc dimmer, and this is compensated for by, primarily, lowering the two temperatures, $T_{\rm B}$ and $T_{\rm F}$.

The accuracy of the reported local minima for the four-parameter fits is evaluated by running the algorithm 1000 times with its simplex vertices randomly selected each time. In practice the number of successful runs is ~ 100 given the tendency for the initial random selection of the highly correlated parameters, $T_{\rm B}$, $T_{\rm F}$, and H_0, to return out-of-bounds values. This problem can be circumvented by either a) spending longer performing the calculation or b) through application of a simulated annealing technique, see, for example, Goad & Koratkar (1998). We do not discuss the implementation of a simulated annealing code here, but remark that the preliminary results substantiate those to be presented, and we assert that sufficient exploration of the multi-dimensional χ^2 topography has been achieved via the random–start technique employed.

Figure 4.8 presents the explored χ^2 topography for a series of four-parameter fits.

Figure 4.9 presents the resulting one-dimensional χ^2 surfaces for each of the four parameters. We estimate the parameters and their respective 1-σ uncertainties from Fig. 4.9 (i.e we examine the range in a given parameter for $\Delta\chi^2 \leq +1$ about the minimum χ^2); $H_0 = 33 \pm 6$ km s^{-1} Mpc^{-1}, $T_B = 9895 \pm 750$ K, $T_F = 8079 \pm 632$ K, $b = 0.73 \pm 0.02$, and $\chi^2_\nu = 1.34$, with $E(B-V) = 0.14$ and $i = 45°$.

There is a well-defined range of values for each fitted parameter, with b particularly well-defined. The index b is partly determined by the spectral slope of the difference spectrum, but is also constrained by the time delays. The range of T_B values is primarily influenced by the time delays, recall eqn. 4.14, which in turn influences the allowed range of T_F values. The high and low temperature cut-offs in T_B and T_F with allowed values of H_0 are governed by the galaxy contamination constraints imposed, with, for example, higher temperatures and lower values of H_0 permitted for larger levels of galaxy contamination.

The estimate of $H_0 = 41$ km s^{-1} Mpc^{-1}, from the single amoeba run, does not fall within the 1-σ confidence region of the random–start based estimate $H_0 = 33 \pm 6$ km s^{-1} Mpc^{-1}, but rather within its 3-σ confidence region. This underscores the importance of assessing the accuracy of the estimated parameters from an amoeba minimization algorithm.

To assess the effects of the uncertainty in the adopted $E(B-V) = 0.14$ value, we carried out a similar random–start technique for a series of five-parameter fits, with $E(B-V)$ the additional parameter (see also Table 4.1). The parameters and their respective 1-σ uncertainties, for permitted $E(B-V) = 0.0 \rightarrow 0.14$, are given by: $H_0 = 38 \pm 3$ km s^{-1} Mpc^{-1}, $T_B = 9550 \pm 350$ K, $T_F = 7400 \pm 400$ K, $b = 0.70 \pm 0.03$, and $\chi^2_\nu = 1.34$, with $i = 45°$. The range of permitted $E(B-V)$ values includes both $E(B-V)$ measurements derived from pointed 21cm observations and the 2200Å dust absorption feature, §4.5.1. The results confirm that to first order the derived D or H_0 is insensitive to reddening by dust, with the disc becoming cooler for lower $E(B-V)$ values via, primarily,

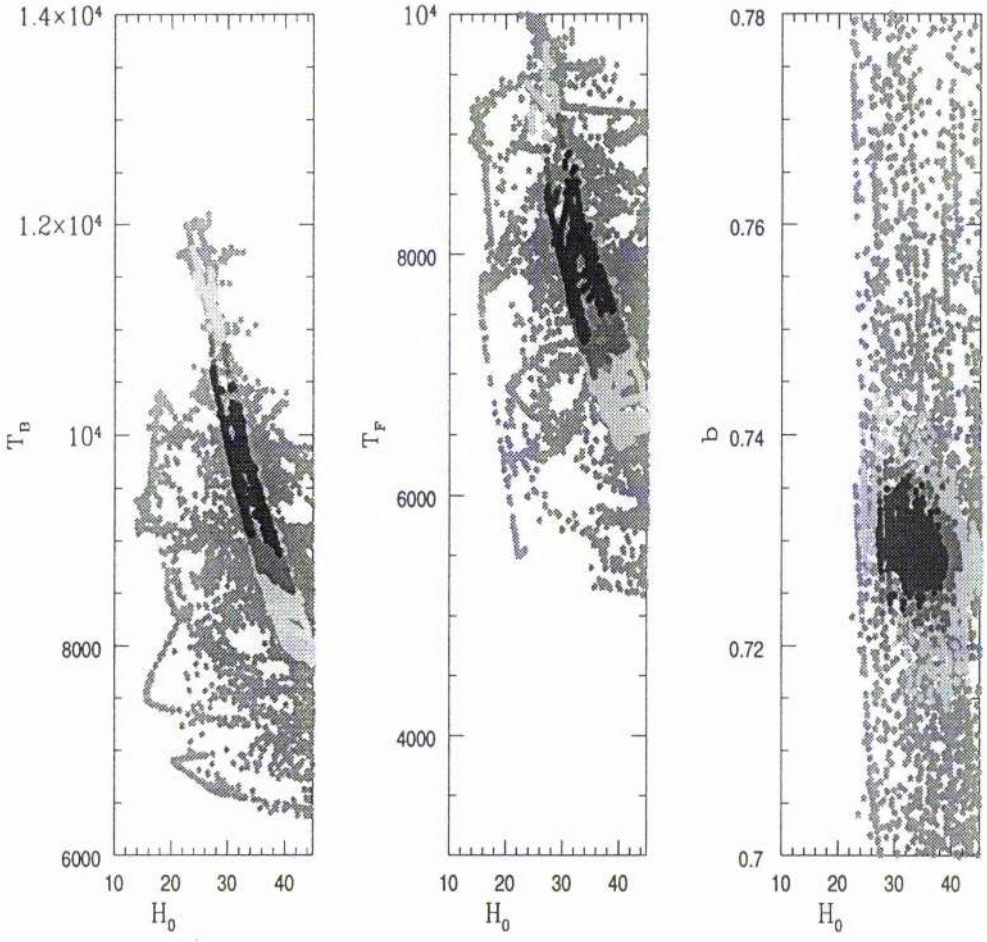

Figure 4.8: The χ^2 topography of the four-parameter blackbody disc fits. The left panel details the variation in χ^2 with $T_{\rm B}$ and H_0, with the two darkest and lightest shades of grey representing $\Delta\chi^2 \equiv \chi^2 - \chi^2_{\rm min} = 2.3$, 4.6, and 11.8 corresponding to 1-σ, 2-σ, and 3-σ confidence regions. Similarly, the middle and right panels detail the χ^2 topography for the parameters $T_{\rm F}$ and H_0, and b and H_0 respectively.

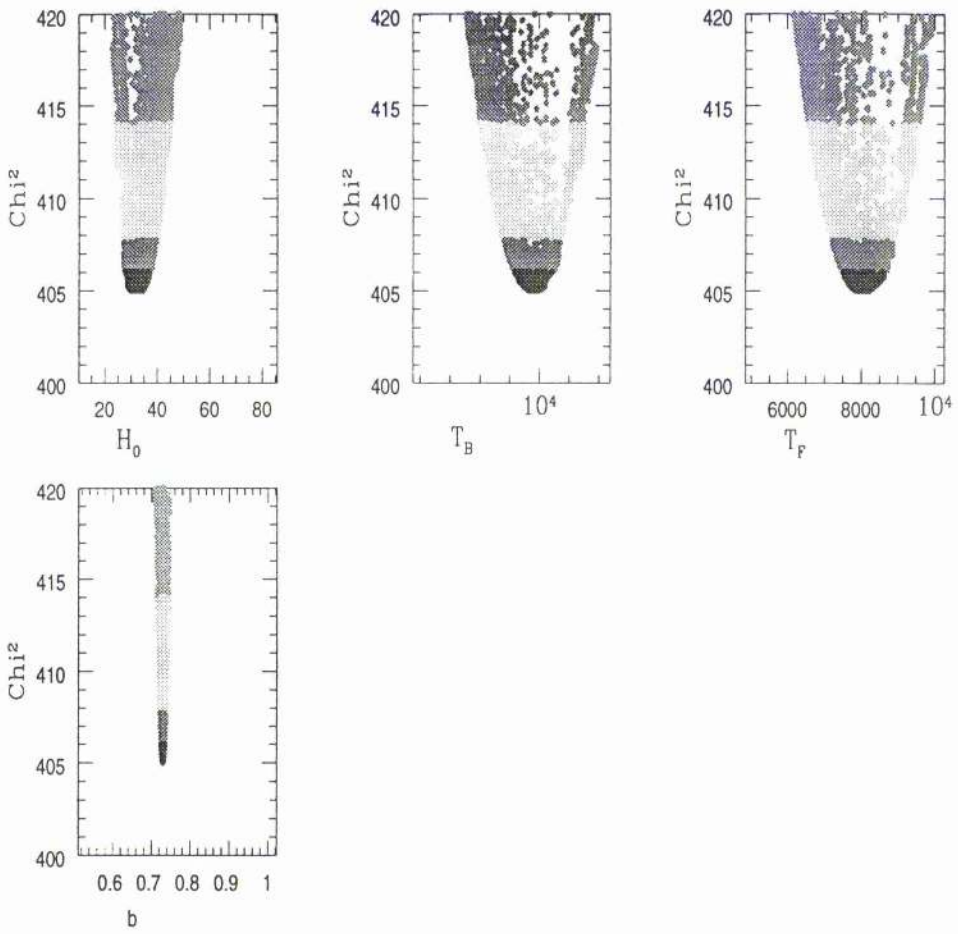

Figure 4.9: The one-dimensional χ^2 surfaces for the four-parameter blackbody disc fits. The top-left panel details the variation in χ^2 of H_0, the top-middle panel the variation in χ^2 of $T_{\rm B}$, the top-right panel the variation in χ^2 of $T_{\rm F}$, and the bottom-left panel the variation in χ^2 of b. For all panels the two darkest and lightest shades of grey represent $\Delta\chi^2 \equiv \chi^2 - \chi^2_{\rm min} = 1.0$, 2.7, and 9.0 corresponding to 1-σ, 2-σ, and 3-σ confidence regions.

Table 4.1: Accretion Disc Model fits to Data (For $i = 45°$)

$E(B-V)$	H_0	T_B	T_F	b	χ^2	χ^2_ν
mags	km s^{-1} Mpc^{-1}	K	K			
0.00	43	7342	6364	0.61	408.9	1.35
0.05	38	8087	6847	0.65	407.1	1.35
0.10	33	8957	7311	0.69	405.9	1.34
0.15	37	8762	7142	0.74	410.4	1.36
0.20	28	11030	8631	0.80	405.7	1.34
0.25	25	13830	11090	0.86	403.7	1.34

Note: For all fits the number of degrees of freedom is 302.

a decrease in the temperatures, T_B and T_F.

Table 4.1, adopts a simplified approach, and details the 'best-fit' four parameters for fixed values of $E(B-V)$. Column 1 gives the fixed value of $E(B-V)$, columns 2, 3, 4, and 5 present the 'best-fit' parameters H_0, T_B, T_F, and b respectively. Columns 6 and 7 detail χ^2 and χ^2_ν for the model fits. For all cases the number of degrees of freedom is 302. The increase in H_0 for $E(B-V) = 0.15$ in Table 4.1 is due to the algorithm becoming trapped in a 'pot-hole' in the relatively flat valley near χ^2_{min}. From the results presented in Table 4.1, for $E(B-V)$ values between 0.00 and 0.14, we derive $H_0 = 38 \pm 5$ km s^{-1} Mpc^{-1}, confirming the results of the random–start technique for the five–parameter fits. The Hubble constant error estimate is smaller for the series' of five parameter fits because χ^2_{min} occurs for $E(B-V) > 0.14$. Hence, when we assess the uncertainty in the fitted parameters we are situated on the steep parabolic edges of the parameters χ^2 surfaces.

Finally, following the discussion of §4.5.3, $(\cos i)^{1/2} = 0.84 \pm 0.1$, and the uncertainty arising from not knowing the disc inclination, i, broadens our final Hubble constant estimate (i.e $H_0 = 38 \pm 5$ km s^{-1} Mpc^{-1}) to $H_0 = 38 \pm 7$ km s^{-1} Mpc^{-1}. This is consistent

with the fit-by-eye estimate of $H_0 = 42 \pm 9$ km s^{-1} Mpc^{-1} from §4.4, and offers a more robust measurement of the Hubble constant.

4.7 The Accuracy of the Hubble Constant Estimate

Our Hubble constant estimate of $H_0 = 38 \pm 7\,\mathrm{km\,s^{-1}\,Mpc^{-1}}$ is significantly lower than the independent 'distance ladder' estimates of $H_0 = 80 \pm 17\,\mathrm{km\,s^{-1}\,Mpc^{-1}}$ by Freedman et al. (1994), and $H_0 = 69 \pm 8\,\mathrm{km\,s^{-1}\,Mpc^{-1}}$ by Tanvir et al. (1995). However, the 18% accuracy of our Hubble constant estimate compares favourably with the 21% and 12% uncertainties of the Hubble constant estimates reported by Freedman and Tanvir respectively. For comparison, the direct methods which utilize the gravitational lenses and Sunyaev-Zel'dovich method give Hubble constant estimates, for example, of $H_0 = 42 \pm 6\,\mathrm{km\,s^{-1}\,Mpc^{-1}}$ (Schecter et al. 1997) and $H_0 = 47^{+23}_{-15}\,\mathrm{km\,s^{-1}\,Mpc^{-1}}$ (Hughes and Birkinshaw 1998). Any apparent discrepancy in the Hubble constant estimates from 'distance ladder' and direct methods will need investigation, which in turn requires statistically significant samples of the methods to be compared.

This result based on observations not specifically designed to measure H_0 can be improved upon. A continuous 2-3 month multi-wavelength, multi-telescope monitoring campaign on a sample of AGNs will make this method a serious competitor with the established methods of measuring H_0. In principle, the time delay measurements can be constrained to better than 5%. There are good prospects for measuring inclinations of individual AGNs with high accuracy. The starlight contamination can be estimated and corrected for as already described, allowing an accurate determination of the nuclear flux spectrum to better than 10%. Finally, a statistical average of individual H_0 measurements will reduce our final uncertainty, and we expect a future optimally designed experiment to determine the Hubble constant with $\leq 10\%$ accuracy.

4.8 Conclusions

To conclude, we identify the *variable* component of the de-reddened UV and optical continuum fluxes as a lower limit to the nuclear spectrum. For NGC 7469 we note that this agrees approximately with the $f_\nu \propto \lambda^{-1/3}$ spectrum predicted for a blackbody accretion disc with a $T \propto R^{-3/4}$ structure. At the same time the wavelength-dependence of the observed time delays, $\tau \propto \lambda^{4/3}$, is consistent with $T \propto R^{-3/4}$. The concurrence of these two independent lines of evidence strongly supports the notion of a standard blackbody accretion disc in NGC 7469, and strengthens the evidence (Shields (1978), Malkan & Sargent (1982), and Miyoshi et al. (1995)) for accretion discs in AGN. Using the *variable* component of the continuum fluxes we find $H_0\,(\cos i/0.7)^{1/2} = 38 \pm 7\,\mathrm{km\,s^{-1}\,Mpc^{-1}}$. Analysis of the observed variable spectrum and wavelength-dependent time delays along the lines outlined above yields redshift-independent luminosity distances to AGNs. This opens up a new route to H_0 and by extension to fainter objects at $z \sim 1$, q_0.

Chapter 5

The UV-optical Variable Spectral Component of AGN

5.1 Summary

We have seen how wavelength-dependent time delays test the standard paradigm of AGN, by measuring the temperature structure $T(R) \propto R^{-b}$ of the gaseous material surrounding the purported black hole, §4.3. Moreover, the slope of the variable nuclear spectrum f_ν constrains the index, b, of the temperature profile relation, since $f_\nu \propto \lambda^{2/b-3}$. Hence, by measuring the slope of the variable nuclear spectrum of the AGN we can estimate b, and predict time delays between any given continuum wave-bands.

This chapter utilizes published data from the majority of International AGN Watch monitoring campaigns on, primarily, comparatively low-luminosity Seyfert 1 galaxies. The chapter serves to aid the optimal design of a monitoring experiment to detect wavelength-dependent time delays, and thereby to investigate the range of temperature structures present in the UV-optical emitting regions of AGN (albeit primarily Seyfert 1 galaxies). Do similar AGNs have intrinsic temperature and flux distributions, $T \propto R^{-3/4}$ and $f_\nu \propto \lambda^{-1/3}$, indicative of classical accretion disc structures? In §5.2 we summarize previous works on determining the shape of the UV/optical AGN continuum. The sample of observations is presented in §5.3. We present the methodology of estimating the variable

component of AGN spectra in §5.4. Difference and RMS spectra are presented in §5.5. The best estimates of the slope of the de-reddened variable spectra, as determined by χ^2 fitting, and associated problems in the slope determination are discussed in §5.6. We estimate time delays between UV/optical continuum variations, and compare our results with those presented by Peterson et al. (1998) in §5.7. The conclusions of this work are presented in §5.8.

5.2 Introduction

The 'Big Blue Bump' (BBB) dominates the UV/optical spectra of AGN, and is a strong broad spectral feature that extends from $\sim$ 1000-4000Å, §1.6. The origin of the BBB is often attributed to either optically thin (free-free) emission (Ferland et al. (1990) and Barvainis (1993)) from an ionized partially transparent region that lies between the source and the BLR (possibly related to the 'warm absorber'), or optically thick emission that is perhaps from the purported accretion disc (e.g Shields (1978) and Malkan & Sargent (1982)).

A fundamental constraint of any model to explain the origin of the UV/optical emission is that the predicted shape or slope of the UV/optical continuum must agree with the available observations. Since the UV/optical spectrum has a multi–component structure this becomes a difficult question to answer, §1.6. Typically, one must allow for the nuisance of emission lines, including the contribution from thousands of blended Fe II lines and the Balmer continuum contamination (the Fe II blend of lines at $\sim$ 2000-3000 Å can contribute $\sim$ 20% of the total flux at about 1840 Å, see Wills et al. (1985)), a wavelength-dependent constant stellar component from the underlying host galaxy (e.g the stellar population of a normal Sab galaxy contributes $\sim$ 20% of the total flux at about 4600Å and $\sim$ 31% at about 6200 Å (see §3.2), and the extinction and reddening of continuum fluxes by dust

distributed somewhere along the observer's line of sight, §4.5.1.

A combination of large AGN samples, soon to be discussed, give an average spectral slope $\alpha \approx 0.3$, i.e. $f_\nu \propto \lambda^{1/3}$. At first sight this appears in conflict with the simple thin disc prediction, $f_\nu \propto \lambda^{-1/3}$ (§4.3.4). However, disc models can be rescued by adding an extra UV-IR component to the disc spectrum, for example, a cool thermal spectrum in the IR + a disc spectrum in the UV/optical (Sun & Malkan (1989)) fits the UV-IR spectral energy distribution. In contrast, the optically thin (free-free) models predict a spectral index that is in agreement with that observed, i.e. $\alpha \approx 0.3$. The accuracy of the above average slope determination, $\alpha \approx 0.3$ for $f_\nu \propto \lambda^\alpha$, applicability to different AGN types and validity across the separate UV and optical spectral regions, is an important issue given the large uncertainties involved in estimating the UV/optical continuum shape. Note, α is defined by $f_\nu \propto \lambda^\alpha$ for the remainder of this chapter.

Sun & Malkan (1989), and references therein, present black hole thin accretion disc model fits (that include the relativistic effects of Doppler boosting, gravitational focusing, and gravitational redshifts) to the UV-optical-IR spectral energy distribution of 60 quasars. Neugebauer et al. (1987) fitted the near IR-UV continua of 100 PG QSOs with a 2 component power-law model and found $\alpha = 0.2$, from about 1500Å to 9500Å ($f_\nu \propto \lambda^\alpha$). Francis et al. (1991) fitted the UV/optical continua of 688 QSOs and found $\alpha = 0.3$.

These studies utilized non-simultaneous wave-band data in their spectral slope determinations, and did not undertake a secure subtraction of the stellar component (presumably on account of the relative weakness of the stellar component in QSOs). The variable nature of AGN, e.g UV/optical flux variations of $\sim 50\%$ on time-scales of months, and uncertain contribution from a stellar component, e.g abnormal host galaxy spectral energy distributions due to induced star formation activity and a distinct red continuum component for Seyfert 1 galaxies, can introduce large uncertainties in the inferred continuum shape.

Furthermore, we note that the Francis et al. (1991) study did not apply reddening corrections to their QSO sample, because all of the sources are found at galactic latitudes greater than 50°. As O'Brien et al. (1988) point out de-reddening spectra with $E(B-V) = 0.03$, leads to a $\approx$ 25% increase in flux at 1500Å, hence accurate reddening corrections can be very important. Therefore, given the possible existence of localized dusty regions throughout the galaxy, we view Francis et al. (1991)'s average slope determination with additional caution.

O'Brien et al. (1988) determined the UV spectral slope $\alpha\,(\mathrm{UV}) = 0.67$ from 68 QSOs using IUE data. This slope may be artificially steepened by Fe II line + Balmer continuum contamination long-ward of 2000Å, and an uncertain stellar contribution. Kinney et al. (1991) measures the UV slope, $\alpha\,(\mathrm{UV}) = 1.3$ between 1200-2600Å for a sample of 15 Seyfert 2 galaxies. Again, this slope may be artificially steepened by Fe II + Balmer continuum contamination, and lack of reddening corrections applied to the data.

The major problem in determining the UV spectral slope lies in the absence of sufficient continuum bands that are free of line and Balmer continuum contamination, perhaps, the 'best' continuum band is that at about 1350Å for Seyfert 1 AGN. Although, the stellar component tends not to dominate at UV wavelengths, it remains important to subtract it (see §4.4).

Edelson & Malkan (1986) fitted the $0.1-100$ μm spectral energy distribution of 29 AGN finding $\alpha\,(0.1-100\ \mu\mathrm{m}) = 1.36$. Winkler et al. (1992) estimates the intrinsic variable flux distributions of 35 Seyfert galaxies, and supports Carleton et al. (1987)'s claim that the intrinsic flux distribution of all Seyfert galaxies are approximately the same, i.e. relatively flat in νf_ν from $100-1$ μm ($\alpha \sim 1$).

Finally, we note that studies that utilize broad-band photometric measurements to yield a spectral slope determination, e.g. Neugebauer et al. (1987) and Winkler et al.

(1992), are subject to bias from contamination by emission-line components. This may result in spurious slope determinations. In principle, the effect of this bias will be relatively straightforward to assess given high quality spectra.

5.3 The Sample of Observations

The International AGN Watch have implemented multi-wavelength monitoring campaigns on NGC 5548 (Clavel et al. (1991), Peterson et al. (1991), Peterson (1994), Romanishin et al. (1995), Korista et al. (1995), and Marshall et al. (1997)), NGC 3783 (Reichert et al. (1994), Stirpe et al. (1994) and Alloin et al. (1995)), NGC 4151 (Crenshaw et al. (1996), Warwick et al. (1996), Kaspi et al. (1996a), and Edelson et al. (1996)), Fairall 9 (Rodriguez-Pascual et al. (1997) and Santos-Lleó et al. (1997)), 3C 390.3 (Leighly et al. (1997), Dietrich et al. (1998), and O'Brien et al. (1998)), and NGC 7469 (see Collier et al. (1998) and references therein). The European LAG collaboration ('Lovers of Active Galaxies'), Robinson (1994), have carried out a number of AGN monitoring campaigns; which have included the following targets; NGC 3227, NGC 3516, NGC 4151, NGC 4593, Mkn 279, and Mkn 876.

This chapter utilizes the spectra and light curves from each of the aforementioned AGN Watch monitoring campaigns, except for 3C 390.3. All the data was obtained from the AGN Watch archive, based at http://www.astronomy.ohio-state.edu/ agnwatch/. The primary characteristics (presented in note form) of the datasets can be summarized in the following way, an extensive discussion of each object is given in the above references.

NGC 4151: This campaign included gamma ray to optical observations for $\sim$ 10 days, with typical UV and optical sampling of $\sim$ 70 minutes and $\sim$ 1 day respectively. NGC 4151 was near its historical peak brightness, and the normalized variability amplitude (NVA) (defined in Edelson et al. (1996)) was about 9% at 1275Å and 1% at 6925Å. The

continuum variations at UV and optical wavelengths are correlated to within about 1 day (see also Peterson et al. (1998)). The underlying host galaxy contributes about 25% of the flux at 5125Å, and the observed wavelength dependence of the normalized variability amplitude is in good agreement with a classical accretion disc structure (see Edelson et al. (1996)).

Fairall 9: This campaign included UV to optical observations for about 8 months, with comparable UV and optical sampling of $\sim$ 4 days. Fairall 9 is about 6 times more luminous than NGC 5548, and underwent UV variations of about a factor of 2 during a $\sim$ 70 day period. In contrast with the results of NGC 5548, the UV continuum shape is not a function of the continuum luminosity, see Rodriguez-Pascual et al. (1997) and Clavel et al. (1992). The variability amplitude $F_{\rm var}$ measures the intrinsic variability relative to the mean flux, corrected for measurement errors, and (Rodriguez-Pascual et al. (1997)) is about 37% at 1390Å and 11% at 5340Å. The wavelength dependence of the variability can be explained by the contaminating contributions of the host galaxy light and Fe II emission; at longer wavelengths the host galaxy contribution is largest and dilutes the variable component. Hence, a 'hardening' of the spectrum as the continuum brightens is not observed in this object.

NGC3783: This campaign included UV, optical, and near IR observations for about 8 months, with typical UV and optical sampling of $\sim$ 4 days. The galactic de-reddened average UV spectral index is $\alpha \sim 0.86$ with $E(B-V) = 0.12$ (Stark et al. (1992) and Burstein & Heiles (1982)) over the SWP bandpass, c.f see NGC 5548 below. However, this estimate is likely to be biased by Fe II + Balmer continuum emission. The continuum 'hardens' as the flux brightens (rms fluctuations $\Delta\alpha \approx 0.16$), in a similar fashion to that observed for NGC 5548. Reichert et al. (1994) states that if the Fe II emission + Balmer continuum contribution is similar to NGC 5548, a change in the spectral index α of ≤ 0.3

is plausible. The dilution of the nuclear continuum by stellar light is also likely to be important, however, it appears likely that much of the spectral variability is intrinsic (Alloin et al. (1995)).

NGC 5548 1989: This campaign included UV to optical observations, with UV and optical sampling of ~ 4 days. The variability amplitude, $F_{\rm var}$, is about 0.32 at 1350Å and 0.14 at 4870Å, and the average de-reddened spectral index for the SWP spectra is $\alpha \simeq 0.95$ with $E(B-V) = 0.05$ (Wamsteker et al. (1990)). However, the intrinsic continuum is thought to be flatter on account of the 10% contribution to the average flux at 1840Å from blended low-contrast Fe II lines, indeed, Wamsteker et al. (1990) measured a de-reddened UV-optical spectral index of $\alpha \simeq 0.39$, after removing the Fe II + Balmer continuum components. The spectral index α is found to vary throughout the monitoring campaign, with the full range of variations $\Delta\alpha = 1.1 \pm 0.2$. Wamsteker et al. (1990) suggests that it is possible that a small amount of this spectral index variation is intrinsic to the source (see Wamsteker et al. (1990)), after correcting for the wavelength-dependent contaminating stellar and Fe II + Balmer continuum emission components.

NGC 5548 1993: This campaign included HST and IUE UV observations, and optical observations, with typical UV and optical sampling of about 2 days for 74 days (HST FOS observations were obtained every day for the last 39 days). The 1350Å continuum varied by about a factor of 2 during the HST observations, and the UV/optical continuum was found to 'harden' as it brightens.

5.4 Estimating the Variable Component of an AGN Spectrum

We have already seen, §5.2, that disentangling the various contributions that constitute the AGN spectrum is fraught with difficulties. We adopt a simplified approach by asserting that the UV/optical continuum spectrum of an AGN is the combination of two

components: a variable nuclear component that emits most of the observed energy and has a constant spectral shape, and a non-variable component that includes the energy from the underlying stellar component and any other non-varying emission component. Other spectral components, e.g variable emission-lines and low contrast variable Fe II blends that appear as a pseudo-continuum, are not considered.

The assumption of constant UV/optical spectral shape is likely to be sufficient to first order, on time-scales of months. The AGN monitoring campaigns, §5.3, show that the fractional variability amplitude decreases with increasing wavelength, and for simultaneous variations at all wavelengths is suggestive that the continuum 'hardens' as the source brightens. However, it has also been shown, e.g. Wamsteker et al. (1990), that much of the wavelength dependence in fractional variability amplitude can be explained by the constant wavelength-dependent contribution from the underlying stellar population and/or the contribution from Fe II line + Balmer continuum emission. We suggest that any residual wavelength-dependence in the variability amplitude is a consequence of reverberation effects, with radiatively driven continuum variations responding quicker at shorter wavelengths, evolutionary effects that alter the distribution of the UV/optical emitting gas, e.g. global re-distribution of broad line gas (Wanders et al. (1995)), and changes in the mechanism that drives the continuum variations; For example, say, the accretion disc is suddenly irradiated by high energy radiation through sporadic flaring activity. The combination of different radial temperature profiles for irradiated and dissipative components could result in significant changes in the spectral slope, §4.3.

For Fairall 9 and NGC 4151 it appears there is no evidence for a change in UV and/or UV/optical slope with luminosity fluctuations, however, for NGC 5548 and NGC 3783 there is suggestive evidence for a positive correlation of spectral index with luminosity. Winkler et al. (1992) concludes that the shape of the variable optical component in a

sample of 35 Seyfert galaxies remains constant to within the measurement errors.

The variable component of AGN spectra can be estimated in the following way;

Difference Spectra: A faint state spectrum can be subtracted from a bright state spectrum to give a lower limit to the nuclear spectrum, provided that the two spectra were taken under similar observing conditions and instrumental configurations. This method cancels the constant wavelength-dependent additive starlight contribution. For low amplitude variations the difference spectra can be dominated by the measurement errors, and this can lead to spurious spectral slope determinations.

The Root-Mean-Square Spectrum: The rms spectrum, $\sigma(\lambda)$ characterises the variable component of a set of spectra, and is defined by

$$\sigma^2(\lambda) = \frac{1}{N-1}\sum_{i=1}^{N}(f_i(\lambda) - \bar{f}(\lambda))^2, \tag{5.1}$$

where the mean spectrum $\bar{f}(\lambda)$ is given by

$$\bar{f}(\lambda) = \frac{1}{N}\sum_{i=1}^{N} f_i(\lambda), \tag{5.2}$$

where $f_i(\lambda)$ are the observed fluxes at epochs t_i, and N is the total number of epochs.

It is apparent that the the rms spectrum estimates the variable, i.e. nuclear flux, component, since by subtracting $f_i(\lambda)$ from $\bar{f}(\lambda)$ the starlight contamination is effectively removed. Therefore, the shape of the rms spectrum reflects the shape of the variable component. Note, for other variability parameters, e.g the amplitude of the intrinsic variability relative to the mean flux corrected for the measurement errors ($F_{\rm var}$: §3.2.2), the slope measurement is biased by a stellar component. Moreover, by subtracting in quadrature the average measurement errors, see §3.2.2, from the rms spectrum one tends to bias the slope measurement.

An optimal scaling algorithm; equivalent to the method employed by Choloniewski (1981) and Winkler et al. (1992), can be used to estimate the variable spectral component.

These authors adopted a two component structure for the AGN spectrum; a constant component and a variable component that can vary in magnitude but preserves its spectral shape.

In this scenario the fluxes at UV, $f_i^{\rm UV}$, and optical, $f_i^{\rm OPT}$, wavelengths for epoch t_i may be linearly related by,

$$f_i^{\rm OPT} = A f_i^{\rm UV} + B, \tag{5.3}$$

where A and B are constants that describe the optical variable component that varies in the same way as the UV component and the mean component of the fluxes respectively. A sample of authors, Wamsteker et al. (1990), Winkler et al. (1992), Winkler et al. (1997) and Reichert et al. (1994), present evidence that a linear relationship between the fluxes of different UV and optical wave-bands is a good description of the data. In the case where the continuum 'hardens' as it brightens, the spectral shape changes and a curvature term in the above relationship is required to fit the data.

In context: The optimal scaling algorithm adopts a UV light curve at, say, 1350Å as the pattern of variability, because here the amplitude of variability tends to be largest and gives the cleanest estimate for the variability pattern. The 1350Å light curve is then normalized by, for example, subtracting the mean flux, $\bar{f}_{1350\mathring{A}}$, from each epoch in the light curve and dividing by the rms value, σ. The exact method of normalization determines the nature of the estimated variable component, e.g whether it reflects the rms spectral component, as in the above example, or the 'best' difference spectrum. The subsequent UV and optical light-curves from the monitoring campaigns are then scaled and vertically shifted to match the 1350Å light-curve, thus recovering $A(\lambda)$ and $B(\lambda)$. The resulting estimate of the variable component given by $A(\lambda)$ can then be compared with the aforementioned methods for measuring the variable component of the AGNs, i.e. the difference spectra and the rms spectra.

We estimate the variable component of our AGN sample by constructing difference spectra for each of the objects, and by using the optimal scaling algorithm described above with the published light curves from each monitoring campaign.

5.5 Results

Multiple estimates for the variable component of 5 AGNs, §5.3, are presented in the following sections. Note: All UV data is that of IUE observations, except for the 1993 campaign on NGC 5548 where HST UV observations have been employed.

5.5.1 Difference Spectra

Figures 5.1-5.6 present unreddened UV/optical maximum, minimum, and difference spectra (bright–faint state) for each AGN Watch monitored object (except for 3C390.3).

Table 5.1 details the separation in epoch between the maximum and minimum spectra for each object. Both the UV and optical maximum and minimum spectra (for all objects) were taken quasi-simultaneously (≤ 1 day), except for the 1989 campaign on NGC 5548 where the UV and optical minimum spectra were taken about 3 days apart. The individual difference spectra, Figs. 5.1-5.6, reflect the variable component of the object on the time-scales indicated in Table 5.1.

5.5.2 Scaling Algorithm Estimates for the Variable Component

Figures 5.7-5.12 present 'best' de-reddened estimates for the rms variable component of each AGN Watch monitored object (except 3C 390.3), and compares these results with the equivalent de-reddened difference spectra.

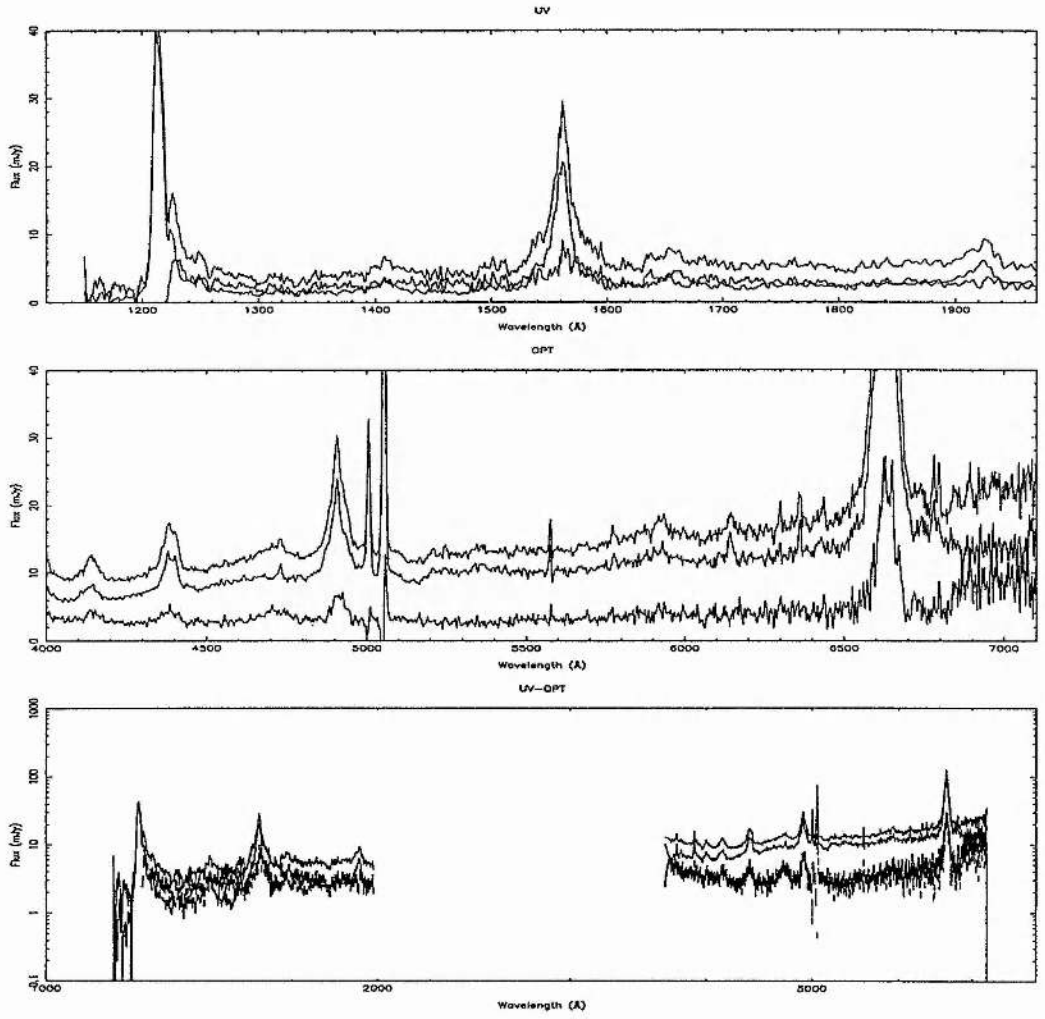

Figure 5.1: The UV/optical difference spectra from NGC 3783 AGN Watch 1991-2 monitoring campaign. The top panel presents the UV maximum, minimum, and difference spectra. The middle panel presents the optical maximum, minimum, and difference spectra. The bottom panel presents the composite UV/optical maximum, minimum, and difference spectra for the campaign. Note the bottom panel is on a logarithmic scale

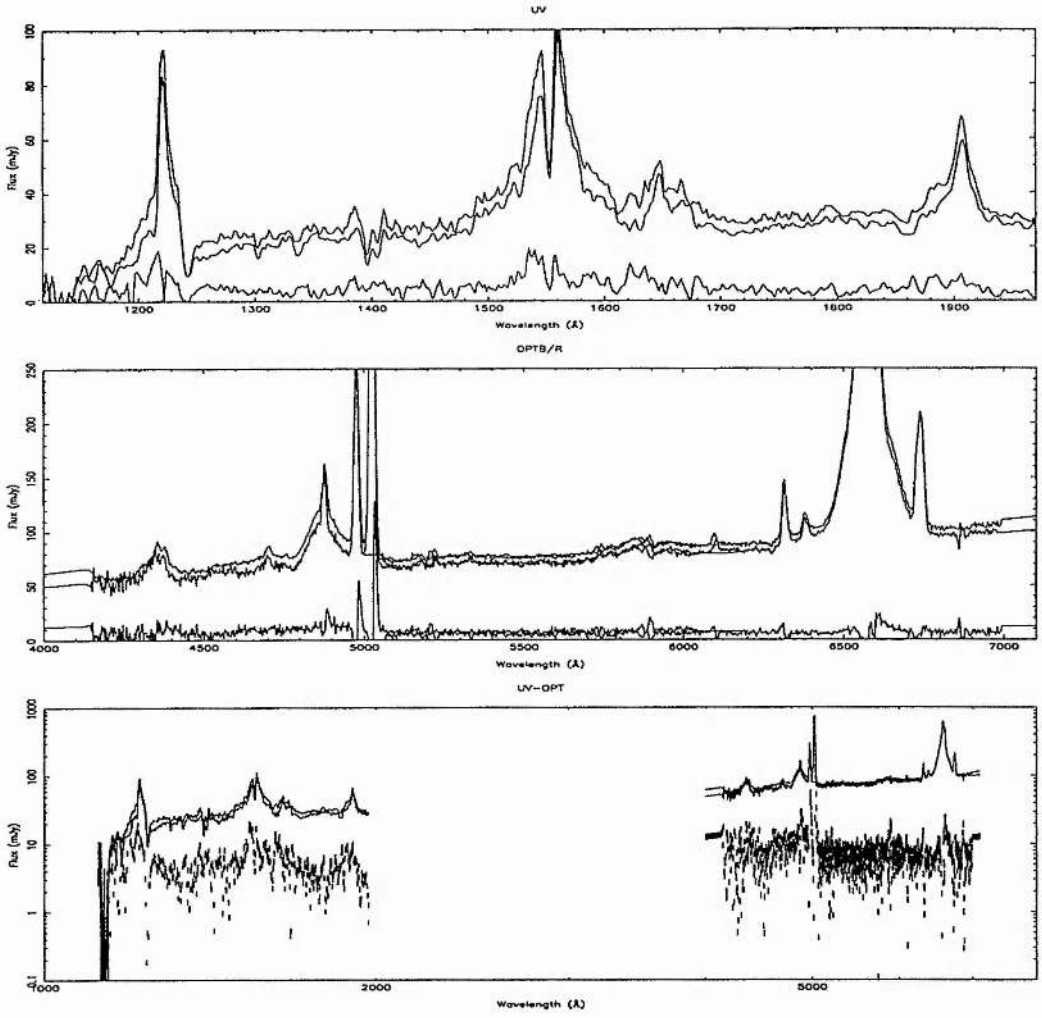

Figure 5.2: The UV/optical difference spectra from NGC 4151 AGN Watch 1993 monitoring campaign. The top panel presents the UV maximum, minimum, and difference spectra. The middle panel presents the optical maximum, minimum, and difference spectra. The bottom panel presents the composite UV/optical maximum, minimum, and difference spectra for the campaign. Note the bottom panel is on a logarithmic scale

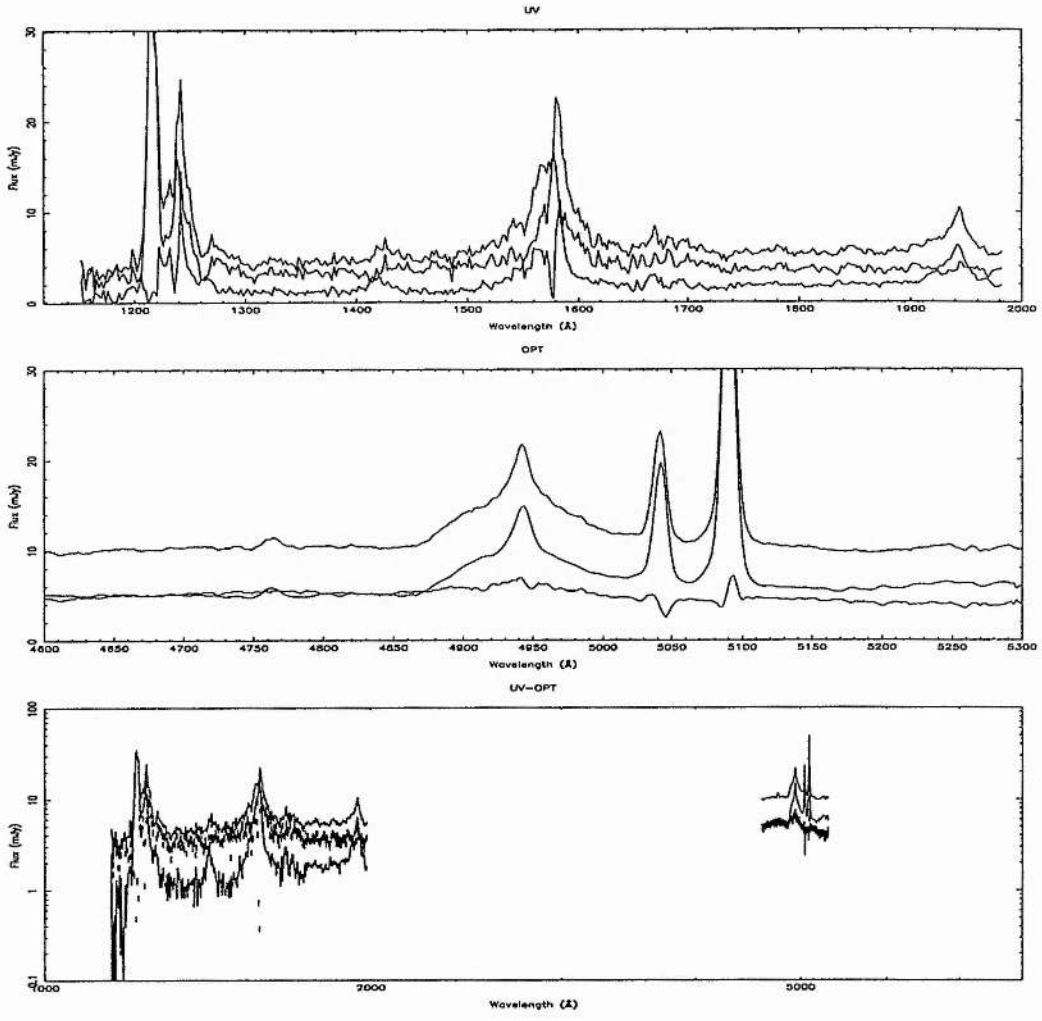

Figure 5.3: The UV/optical difference spectra from NGC 5548 AGN Watch 1989 monitoring campaign. The top panel presents the UV maximum, minimum, and difference spectra. The middle panel presents the optical maximum, minimum, and difference spectra. The bottom panel presents the composite UV/optical maximum, minimum, and difference spectra for the campaign. Note the bottom panel is on a logarithmic scale

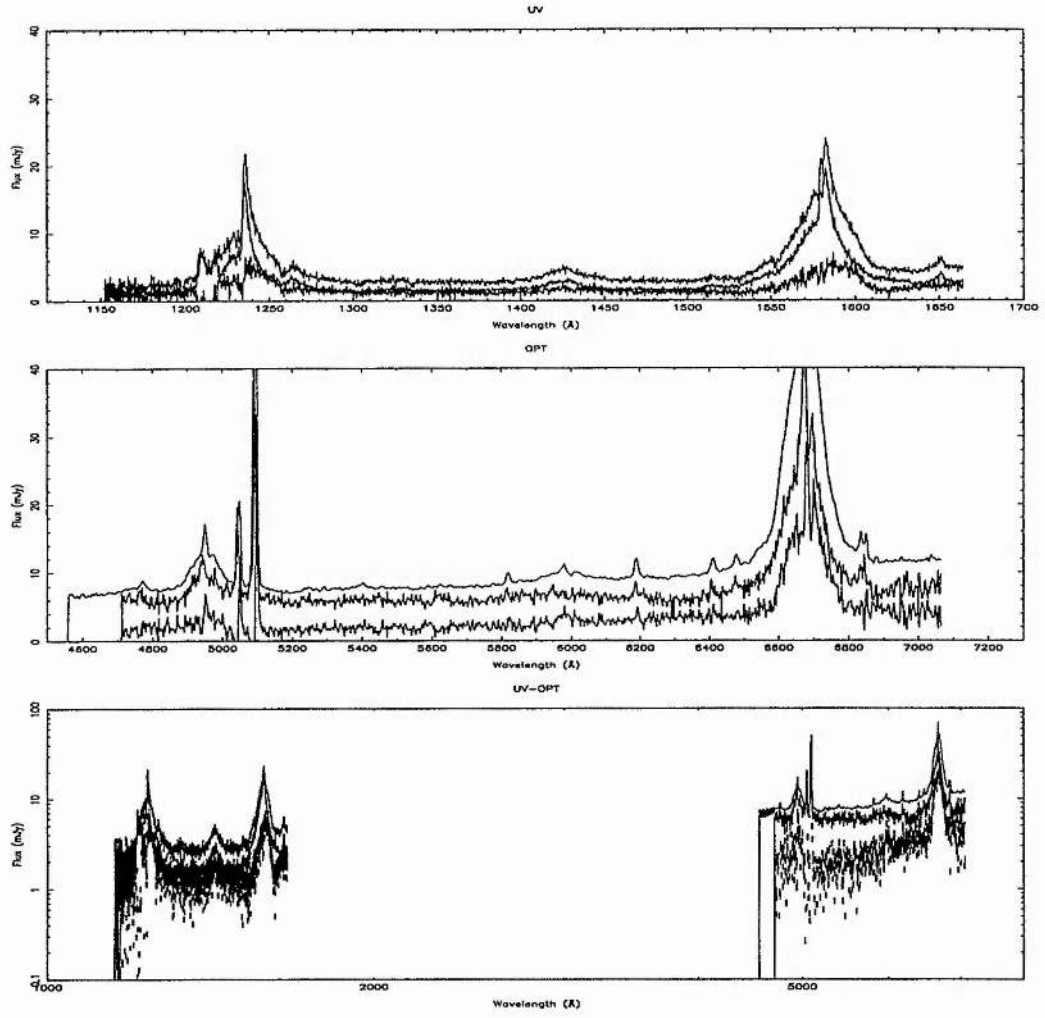

Figure 5.4: The UV/optical difference spectra from NGC 5548 AGN Watch 1993 monitoring campaign. The top panel presents the UV maximum, minimum, and difference spectra. The middle panel presents the optical maximum, minimum, and difference spectra. The bottom panel presents the composite UV/optical maximum, minimum, and difference spectra for the campaign. Note the bottom panel is on a logarithmic scale

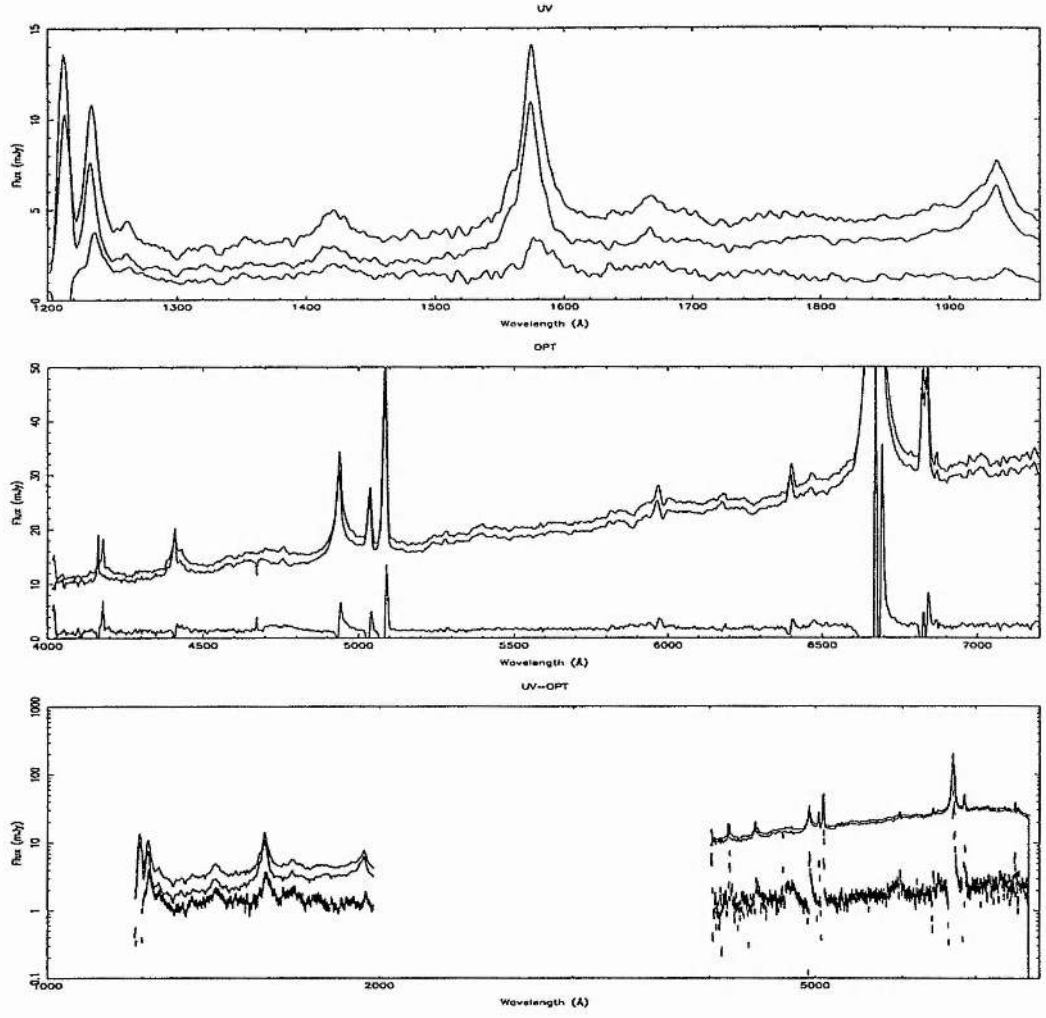

Figure 5.5: The UV/optical difference spectra from NGC 7469 AGN Watch 1996 monitoring campaign. The top panel presents the UV maximum, minimum, and difference spectra. The middle panel presents the optical maximum, minimum, and difference spectra. The bottom panel presents the composite UV/optical maximum, minimum, and difference spectra for the campaign. Note the bottom panel is on a logarithmic scale

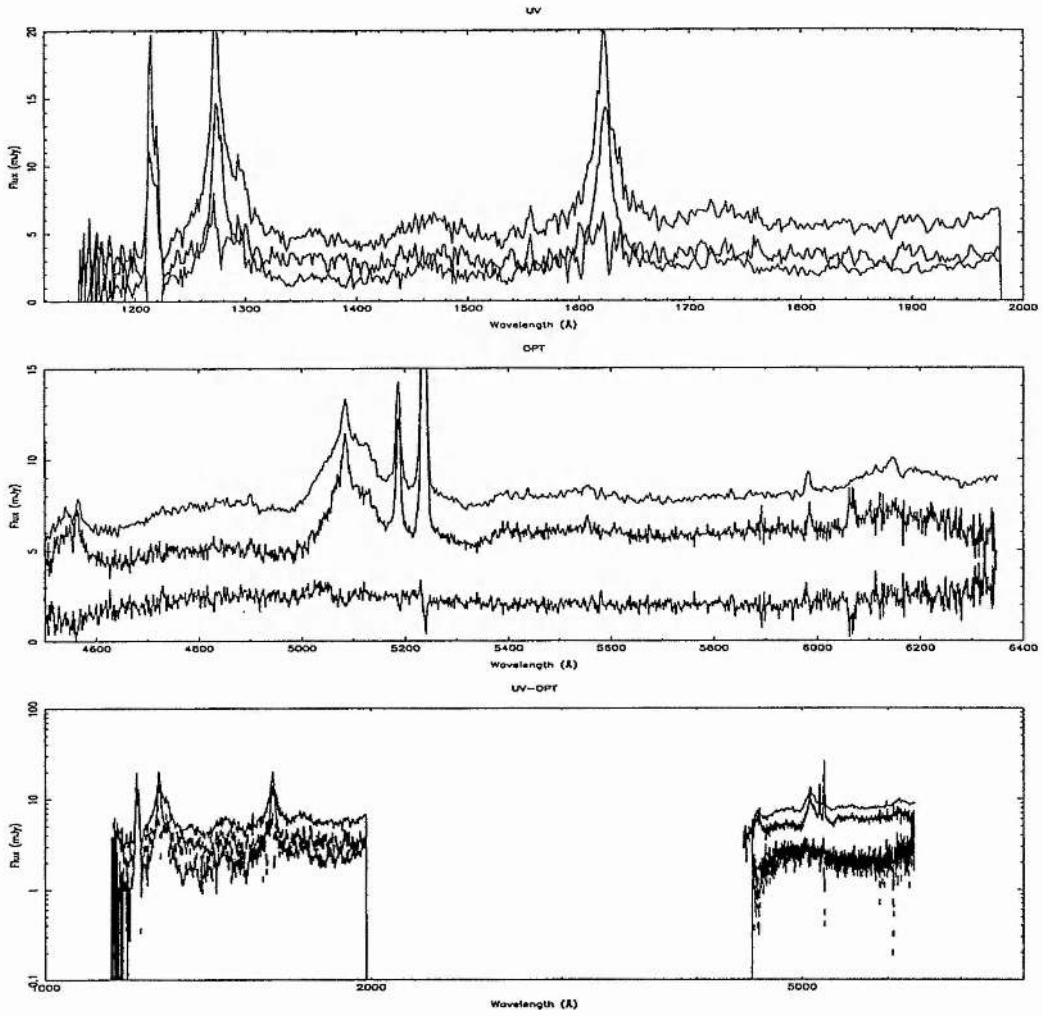

Figure 5.6: The UV/optical difference spectra from Fairall 9 AGN Watch 1994 monitoring campaign. The top panel presents the UV maximum, minimum, and difference spectra. The middle panel presents the optical maximum, minimum, and difference spectra. The bottom panel presents the composite UV/optical maximum, minimum, and difference spectra for the campaign. Note the bottom panel is on a logarithmic scale

Table 5.1: UV/optical Maximum and Minimum Epoch Separation

Target	$\Delta\tau_{UV}$ days	$\Delta\tau_{OPT}$ days
NGC 3783	43.6	43.8
NGC 7469	40.4	40.5
NGC 4151	7.2	7.0
NGC 5548_{93}	25.0	24.8
NGC 5548_{89}	123.4	128.
Fairall 9	187.5	188.8

5.5.3 The Slope of the Variable Spectral component in AGN Sample

The difference and rms spectra were constructed to include only flux values for each wavelength bin in continuum regions used in the literature, §5.3. The variable spectra were de-reddened with the standard interstellar reddening law of Seaton (1979), using nominal $E(B-V)$ values applicable to each object (detailed in Table 5.2.). Note: The nominal $E(B-V)$ values used are 'best' estimates derived from the literature, see the following discussion. Then, the model $f_\nu = C\lambda^\alpha$ was fitted to the spectra, with C a constant and α the spectral slope index, using an amoeba χ^2 minimization algorithm, §4.6. The results are presented in Figs. 5.7-5.12 and Table 5.2. Column 1 details the AGN, column 2 the nominal $E(B-V)$ value used in de-reddening the variable spectra, columns 3 and 4 give the slope α as measured from the difference and rms spectra respectively, and column 5 details the average and dispersion (defined by half of the full range in α measurements) of α using columns 3 and 4. Note: Observed fluxes and wavelengths are used throughout this chapter, with no correction for the redshift of the AGN. The derived slope is not significantly altered by correcting for the low-redshifts of our AGN sample.

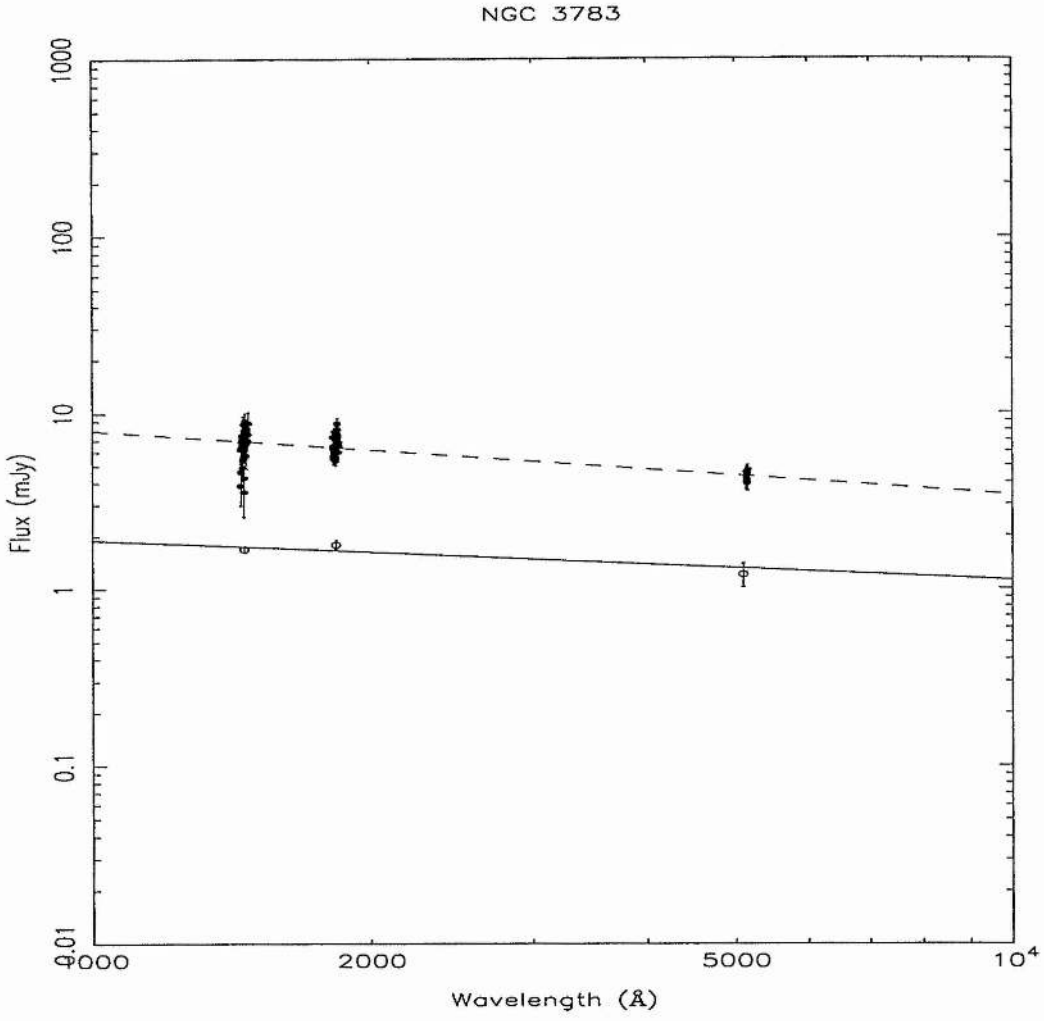

Figure 5.7: The difference and optimally estimated rms spectra (§5.5) of NGC 3783, de-reddened using $E(B-V) = 0.12$. The open symbols denote the rms spectrum, with the solid line detailing the 'best-fit' model, $f_\nu = C\lambda^{-0.23}$ with C a constant. The solid symbols denote the difference spectrum, with the dashed line detailing the 'best-fit' model, $f_\nu = C^*\lambda^{-0.37}$ with C^* a constant.

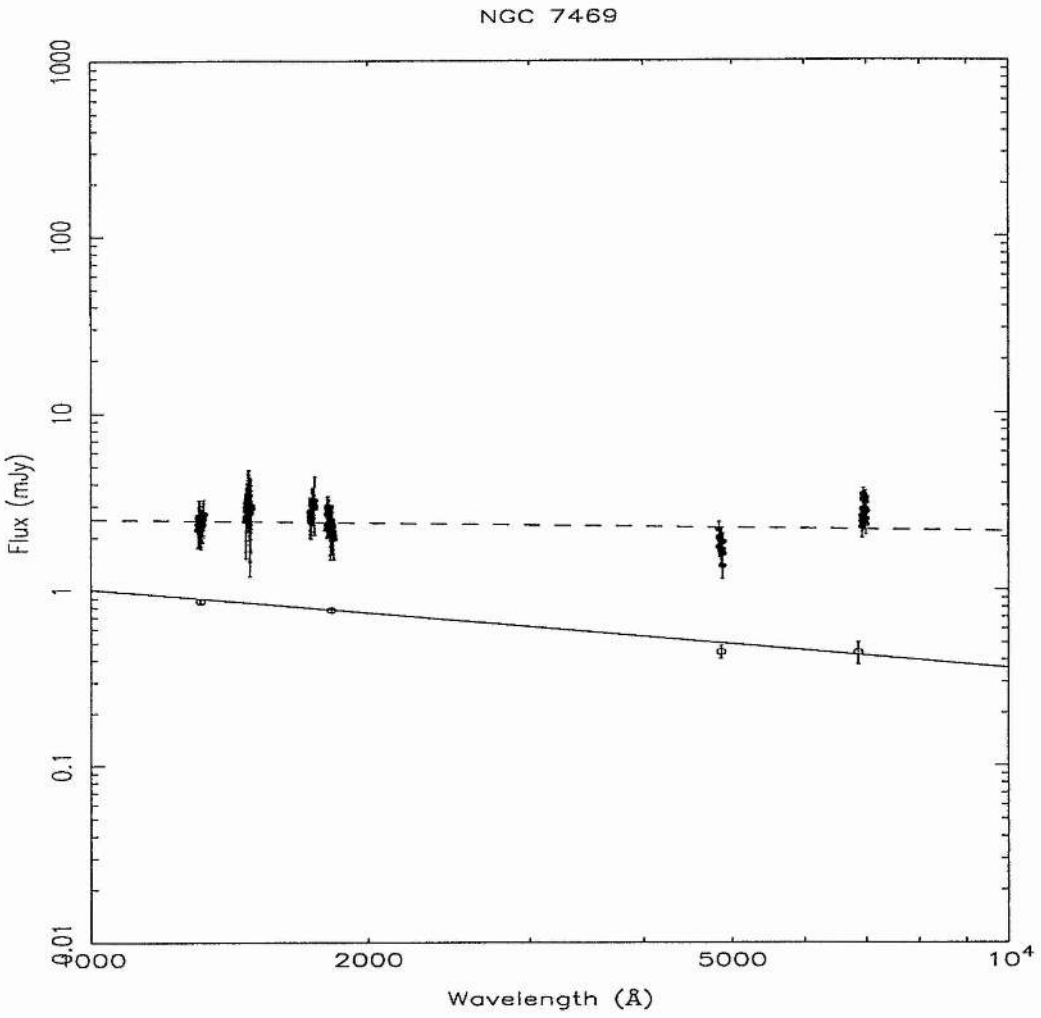

Figure 5.8: The difference and optimally estimated rms spectra (§5.5) of NGC 7469, de-reddened using $E(B-V) = 0.10$. The open symbols denote the rms spectrum, with the solid line detailing the 'best-fit' model, $f_\nu = C\lambda^{-0.45}$ with C a constant. The solid symbols denote the difference spectrum, with the dashed line detailing the 'best-fit' model, $f_\nu = C^*\lambda^{-0.07}$ with C^* a constant.

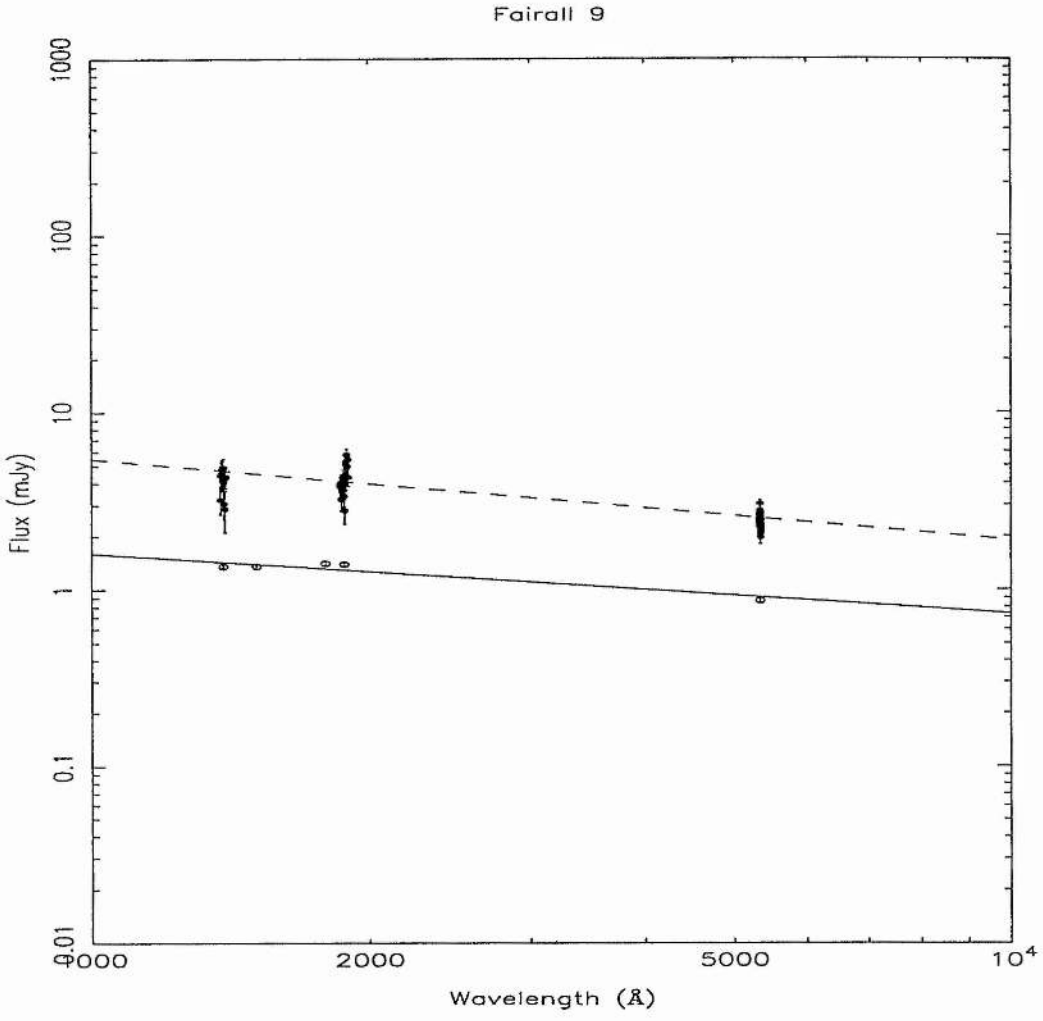

Figure 5.9: The difference and optimally estimated rms spectra (§5.5) of Fairall 9, de-reddened using $E(B-V) = 0.04$. The open symbols denote the rms spectrum, with the solid line detailing the 'best-fit' model, $f_\nu = C\lambda^{-0.34}$ with C a constant. The solid symbols denote the difference spectrum, with the dashed line detailing the 'best-fit' model, $f_\nu = C^*\lambda^{-0.46}$ with C^* a constant.

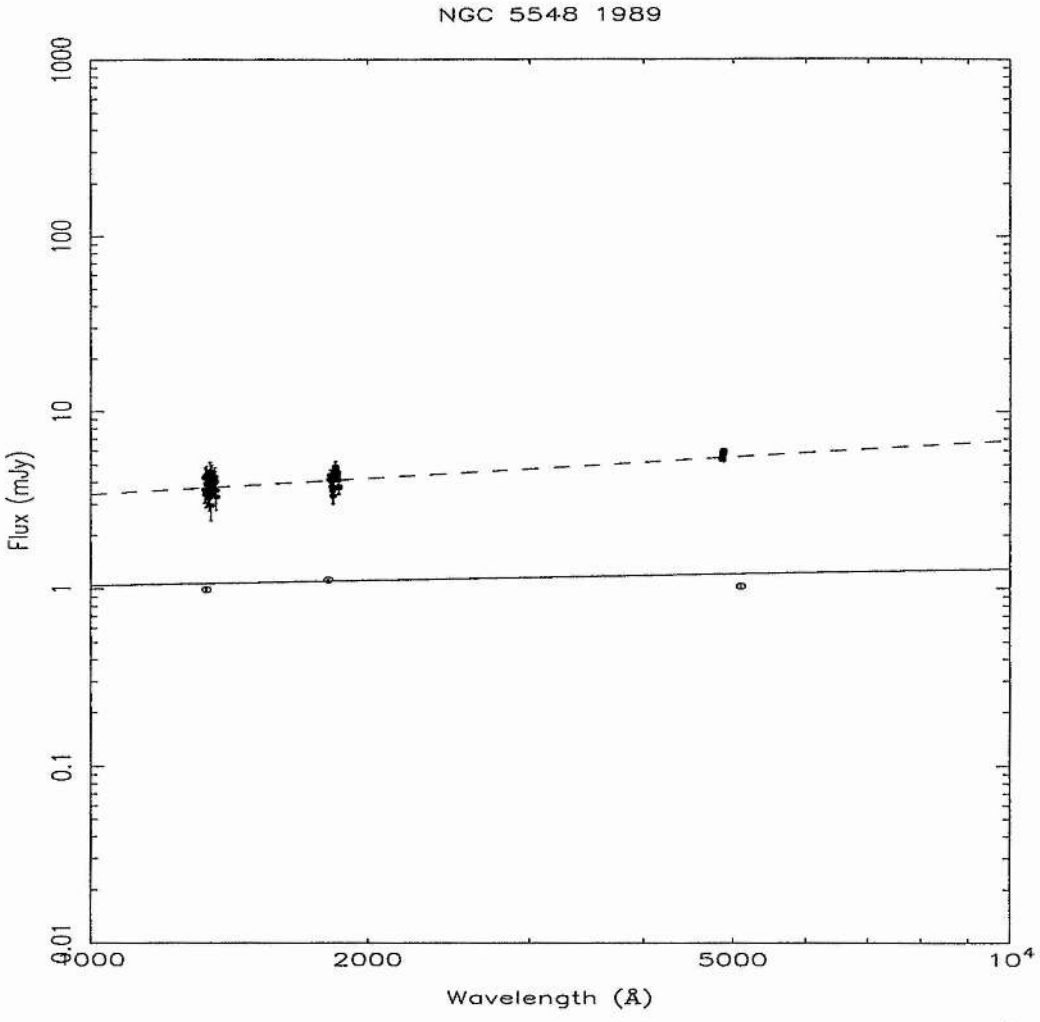

Figure 5.10: The difference and optimally estimated rms spectra (§5.5) of NGC 5548 from the 1989 monitoring campaign, de-reddened using $E(B-V) = 0.02$. The open symbols denote the rms spectrum, with the solid line detailing the 'best-fit' model, $f_\nu = C\lambda^{0.09}$ with C a constant. The solid symbols denote the difference spectrum, with the dashed line detailing the 'best-fit' model, $f_\nu = C^*\lambda^{0.30}$ with C^* a constant.

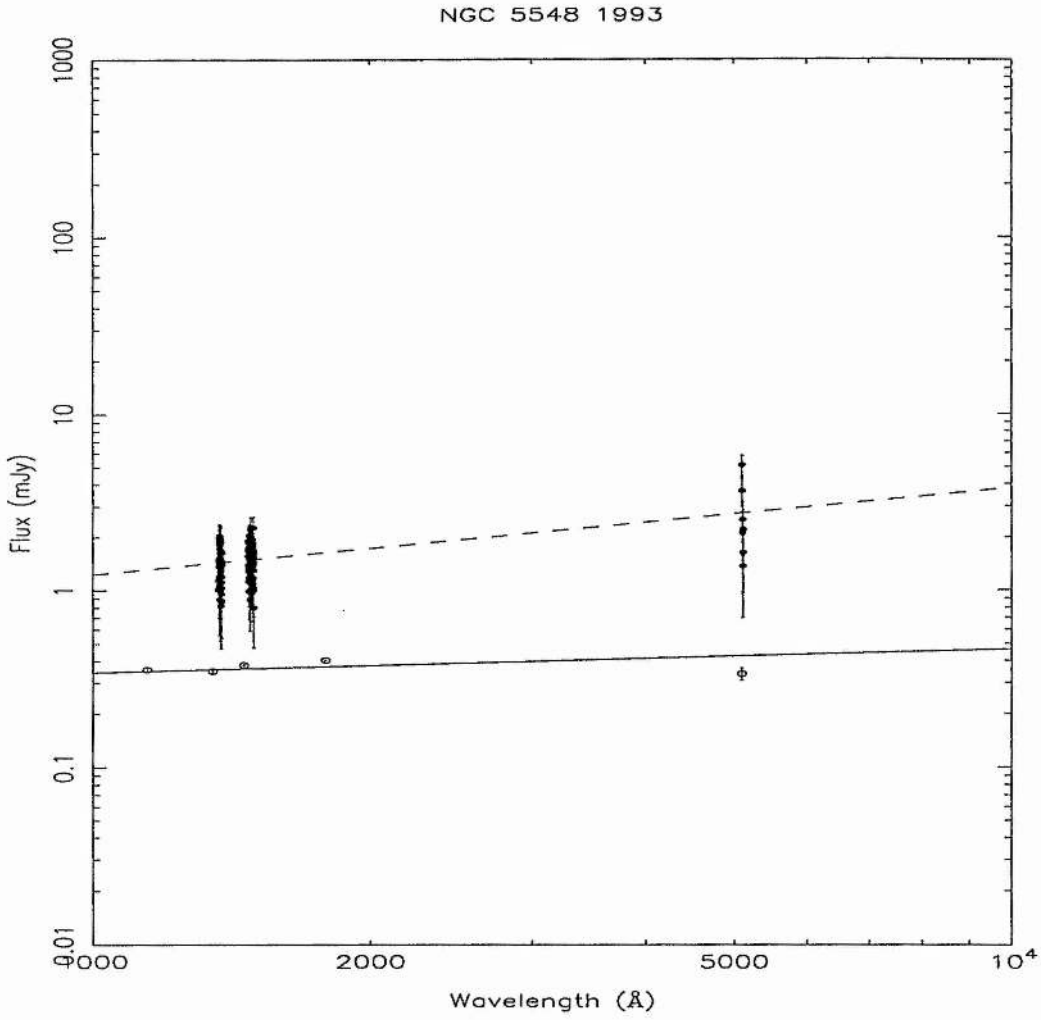

Figure 5.11: The difference and optimally estimated rms spectra (§5.5) of NGC 5548 from the 1993 monitoring campaign, de-reddened using $E(B-V) = 0.02$. The open symbols denote the rms spectrum, with the solid line detailing the 'best-fit' model, $f_\nu = C\lambda^{0.13}$ with C a constant. The solid symbols denote the difference spectrum, with the dashed line detailing the 'best-fit' model, $f_\nu = C^*\lambda^{0.49}$ with C^* a constant.

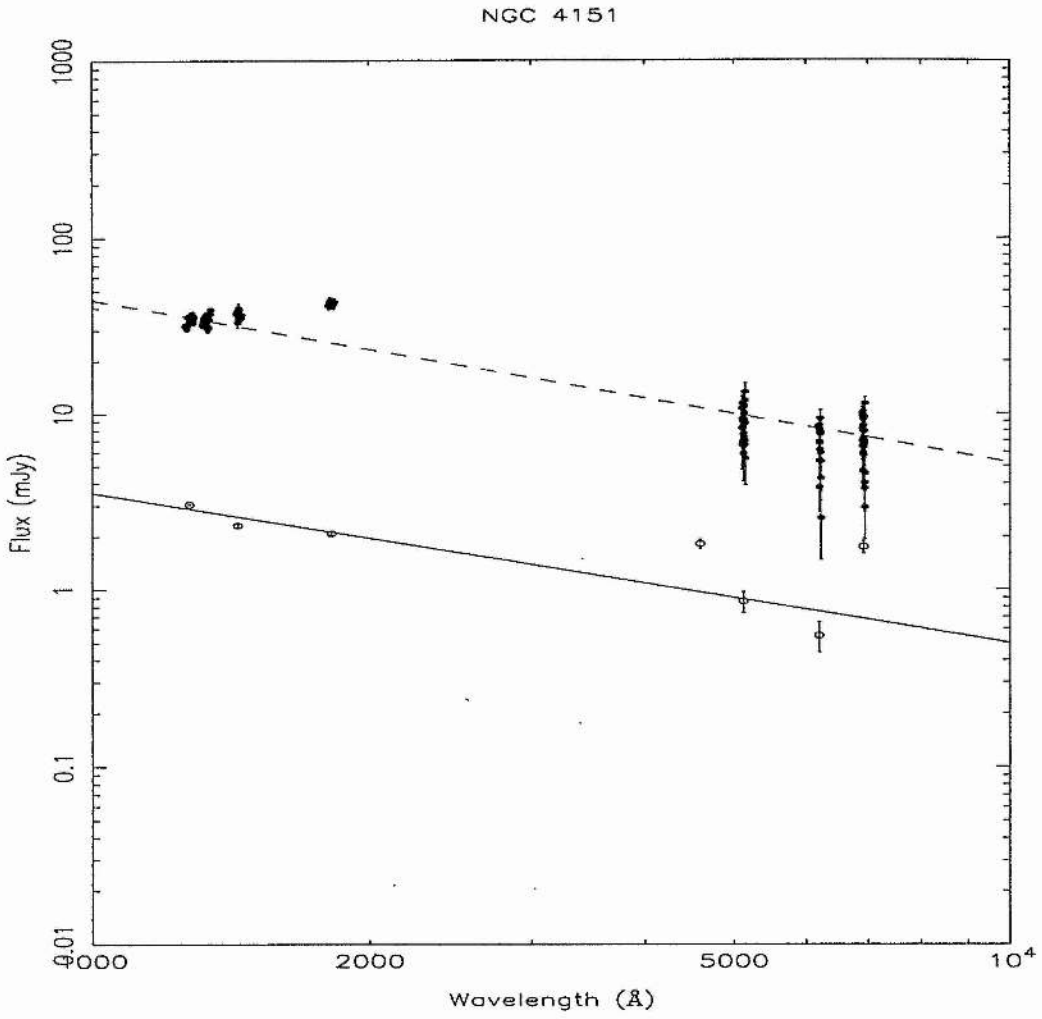

Figure 5.12: The difference and optimally estimated rms spectra (§5.5) of NGC 4151, de-reddened using $E(B-V) = 0.04$. The open symbols denote the rms spectrum, with the solid line detailing the 'best-fit' model, $f_\nu = C\lambda^{-0.85}$ with C a constant. The solid symbols denote the difference spectrum, with the dashed line detailing the 'best-fit' model, $f_\nu = C^*\lambda^{-0.93}$ with C^* a constant.

Table 5.2: The Slope of the Variable Spectra of AGN

Target	$E(B-V)$[1]	α		$<\alpha>$
		Difference	RMS	
	mag.			
NGC 3783	0.12	-0.37	-0.23	-0.30 ± 0.07
NGC 7469	0.10	-0.07	-0.45	-0.26 ± 0.19
NGC 4151	0.04	-0.93	-0.85	-0.89 ± 0.04
NGC 5548_{89}	0.02	0.49	0.13	0.31 ± 0.18
NGC 5548_{93}	0.02	0.30	0.09	0.20 ± 0.10
Fairall 9	0.04	-0.46	-0.34	-0.40 ± 0.06

[1] See §5.5.3, §4.5.1 and §1.6 for references to $E(B-V)$ values.

The rms spectra give systematically lower continuum flux measurements. The rms and difference spectra for each individual object sometimes differ in the number of continuum regions utilized, this primarily reflects the absence of light curves (in the AGN Watch database) for a given continuum region, and is likely to be partly responsible for the different slope indices recovered by the two estimates. In all cases, the formal fitting errors on α are smaller than the dispersion (i.e. half of the full range), σ, in α measurements from the two methods. We proceed to average the two α values and adopt this dispersion as a likely error estimate, see Table 5.2. The different α values recovered via the two methods highlight the sensitivity of the slope determination to the use of additional continuum regions and methods to estimate the variable spectral component.

We note that the measurement errors in the rms spectra for the NGC 5548 campaigns, Fig. 5.10 and Fig. 5.11, appear to be underestimated, as evidenced by the poorer model

fit to the data, and is most likely due to the optimistic measurement errors assigned to the NGC 5548 light curves. The erratic nature of the optical continuum for the NGC 4151 campaign, Fig. 5.12, is not fully understood, and should be viewed with caution.

It is apparent that the deduced slope of the variable spectra can be a function of the wavelength region used in its estimation, for example, for the case of NGC 7469 there is a distinct flattening of the slope in the optical region, which is indicative of a flattening in the temperature structure of the disc material, perhaps due to irradiation.

There is also evidence, see Fig. 5.7 and Fig. 5.11, that a UV slope determination would be biased towards flatter or more positive slopes (in $f_\nu \propto \lambda^\alpha$) than a UV/optical slope determination, perhaps due to Fe II line + Balmer continuum contamination in the UV. For example: Using the rms spectrum of NGC 3783, the slope determined by the two UV data-points (at 1460Å and 1835Å) is $\alpha = 0.25$, c.f the slope determined with the UV data-point at 1460 Å and the optical data-point at 5100 Å, $\alpha = -0.27$. Say, the Fe II line + Balmer continuum contamination at 1835Å is 20% of the total 1835Å flux, then by removing this contamination we will deduce a slope $\alpha = -0.74$ between the 2 UV data-points. This simple exercise underscores the dependence of the shape of the variable AGN continua on a given spectral range and the importance of continuum-contaminating components, e.g Fe line emission. Only, for NGC 7469 and NGC 4151 is there speculative evidence for a change in slope between the UV and optical regions. To assess whether there is a change in the UV and optical spectral shape, simultaneous UV and optical observations will be critical. We emphasize that the error in any slope measurement is a strong function of the wavelength range employed in its derivation.

We discussed various methods for estimating the reddening of AGN in §4.5.1, and numerous authors discuss the uncertainties in the derived reddening corrections, e.g Sun & Malkan (1989), Edelson & Malkan (1986), and Malkan (1984). For example; Malkan

(1984) presented evidence for a well-defined blue ridge in the UV/optical colours of 48 AGNs, and asserted the ridge colours were those of intrinsically unreddened quasars. Furthermore, the small scatter in the ridge colours determines an empirical upper limit on the continuum reddening of $E(B-V) \sim 0.05 - 0.10$ magnitudes, and suggests that QSOs have intrinsically low internal reddening. This was strongly supported by the work of Wilkes et al. (1987), who used X-ray observations to measure $N_{\rm H}$ column densities of 33 quasars and showed that $N_{\rm H}$ in excess of 21cm Galactic hydrogen column densities are not required at $> 90\%$ confidence, hence there is negligible internal reddening of the QSO sample.

The general consensus favours a Galactic origin for the primary source of reddening, see above. We adopt an 'ad-hoc' approach to assessing the uncertainties in the nominal reddening corrections detailed in Table 5.2, by asserting the error in our applied $E(B-V)$ reddening corrections is ± 0.05 magnitudes. This ensures that our reddening corrections are consistent with a large sample of the current literature that derive reddening corrections based on a variety of methods.

The uncertainty in α induced by the uncertainty in the adopted $E(B-V)$ values was estimated by de-reddening the variable spectra by a range of $E(B-V)$ values, defined by the adopted 0.05 magnitude uncertainty in the nominal $E(B-V)$ values, and computing the corresponding range in spectral slopes. The results are presented in Table 5.3. Column 1 details the AGN, column 2 denotes the range in $E(B-V)$ values used, and column 3 gives the average spectral index α. The uncertainty on the average value, column 3, is determined by summing in quadrature the uncertainties due to the range of $E(B-V)$ values and the dispersion in α due to the different variable spectra estimation methods. For all objects, except the NGC 5548 campaigns, the dominant source of error in the α estimates is due to the uncertainty in the reddening corrections.

Table 5.3: Further estimates of Variable Spectral Component of AGN

Target	$E(B-V)$	α
	mags	
NGC 3783	0.07–0.17	-0.30 ± 0.19
NGC 7469	0.05–0.15	-0.27 ± 0.27
NGC 4151	0.00–0.09	-0.91 ± 0.16
NGC 5548_{93}	0.00–0.07	0.26 ± 0.22
NGC 5548_{89}	0.00–0.07	0.14 ± 0.16
Fairall 9	0.00–0.09	-0.43 ± 0.18

For NGC 3783, Reichert et al. (1994) measured an average UV spectral index $\alpha \sim 0.86$. We estimate $\alpha \approx 0.25$. The discrepancy between our estimates is most likely a result of host galaxy contamination in the Reichert et al. (1994) measurement. The methods we employ to estimate the variable component of the spectra accurately remove the underlying host galaxy component.

For NGC 5548, Wamsteker et al. (1990) measured a de-reddened UV/optical spectral index of $\alpha \approx 0.39$, after removing the Fe II line + Balmer continuum contamination. We estimate $\alpha \approx 0.14$. Part of the discrepancy is most likely due to host galaxy contamination in the former measurement.

The α estimates for NGC 7469, NGC 3783, and Fairall 9 are consistent to within the quoted uncertainties. NGC 5548 is the only AGN in our sample that suggests a positive ($f_\nu \propto \lambda^\alpha$) slope, and is inconsistent with slope estimates of the aforementioned AGN. In view of the erratic nature of the rms spectrum for NGC 4151, its slope measurement must be viewed with caution. An unweighted average α was calculated from the entire AGN sample, $\alpha_{\rm sample} = -0.25 \pm 0.17$, and is consistent with the simple thin disc prediction,

$f_\nu \propto \lambda^{-1/3}$.

The average slope we measure, $\alpha_{\rm sample} = -0.25 \pm 0.17$, appears inconsistent with that measured by other large samples (see §5.2), $\alpha \sim 0.2$. However, it is likely that the uncertainty in the latter average slope determination is at least ± 0.5 (personal estimate),which would make the two estimates seemingly consistent, and precludes any definitive statement concerning the different UV/optical spectral slopes for different AGN samples.

Typically, the earlier studies of §5.2 displayed one or more of the following attributes; lack of appropriate reddening corrections, no or inadequate allowance for the host galaxy component, use of non-simultaneous multiwaveband data, and/or the use of broad band filter observations. These attributes can be contrasted with those of our sample, namely the use of quasi-simultaneous (to within ≤ 1 day) multi-wavelength continuum data, an accurate subtraction of the host galaxy component, and suitable consideration of appropriate reddening corrections. Hence, we view our average spectral slope determination as an improvement over earlier similar measurements.

5.5.4 Prediction of UV/optical time delays in AGN Watch sample

Recapitulating the discussion of §4.3: By measuring the spectral slope, α, we can determine the temperature profile index b of the AGNs, $b = 2/(\alpha + 3)$. Furthermore, γ describing the wavelength dependence of any time delays, $\tau \propto \lambda^\gamma$ is given by, $\gamma = 1/b$.

The measured values for α, b and γ of our AGN sample are presented in Table 5.4. The unweighted average b and γ for the AGN sample are $b = 0.73 \pm 0.05$ and $\gamma = 1.37 \pm^{0.10}_{0.09}$. We note the thin disc predictions are $b = 0.75$ and $\gamma = 4/3$, and are consistent with the aforementioned equivalent average values of our AGN sample.

The expected magnitude of the UV/optical time delays for the AGNs can be calculated

Table 5.4: The Spectral Slope, Temperature index, and Wavelength-dependence of Time Delays

Target	α	b	γ
NGC 3783	-0.30 ± 0.19	$0.74^{+0.06}_{-0.05}$	1.35±0.10
NGC 7469	-0.27 ± 0.27	$0.73^{+0.08}_{-0.06}$	$1.37^{+0.12}_{-0.14}$
NGC 4151	-0.91 ± 0.16	$0.96^{+0.08}_{-0.07}$	1.04±0.08
NGC 5548_{93}	0.26 ± 0.22	$0.61^{+0.05}_{-0.04}$	$1.64^{+0.11}_{-0.12}$
NGC 5548_{89}	0.14 ± 0.16	0.64±0.03	$1.56^{+0.08}_{-0.07}$
Fairall 9	-0.43 ± 0.18	$0.78^{+0.06}_{-0.05}$	1.28±0.09

using equations 4.19, §4.3. Recall,

$$\Delta f_\nu = f_\nu^{\rm B} - f_\nu^{\rm F} = \frac{4\pi \cos i}{D^2} hc^3 \lambda^{-3} < \tau >^2 \frac{1}{b} \frac{(I_2(b)(1-\varepsilon))^3}{(I_3(b)(1-\varepsilon^{3/2}))^2}. \tag{5.4}$$

For definitions of the various quantities see §4.3.

By adopting a value for the Hubble constant $H_0 = 50\ {\rm km\,s^{-1}\,Mpc^{-1}}$, we can use the redshift z of the AGN to calculate the distance D. The ratio of the faint to bright state fluxes ($f_\nu^{\rm F}$ and $f_\nu^{\rm B}$ respectively) at a given wavelength defines ε, then by adopting $i = 45°$, and using an UV variable flux measurement, say at $\sim$ 1350Å (taken from the difference spectra) and the slope of the variable spectra we can predict the time delay τ at any given wavelength. The results are presented in Table 5.5. Column 1 details the AGN, columns 2 and 3 give ε and $\Delta f_\nu(\lambda)$, column 4 details the predicted relative time delay between the continuum variations at 1315Å and 7000Å, column 5 presents similar predicted time delays (between slightly different wavelength regions) from Peterson et al. (1998) (see forthcoming text), column 6 details equivalent (i.e between identical wavelength regions used in column 5) estimates for the relative time delays to those of column 5, and column

Table 5.5: Prediction of Time delays in AGN

Target	ε	$\Delta f_\nu(\lambda)$	$\Delta\tau_{1315-7000\mathring{A}}$	$\Delta\tau_{\rm BMP}$	$\Delta\tau$	$\Delta\tau^*_{1315-7000\mathring{A}}$
		mJy (Å)	days	days	days	days
NGC 3783	0.4	6.1 (1445)	0.6±0.2	1.1	0.4	0.5±0.3
NGC 7469	0.6	2.2 (1306)	$0.8^{+0.5}_{-0.3}$	—	—	0.7±0.5
NGC 4151	0.7	8.7 (1260)	$0.1^{+0.04}_{-0.03}$	1.1	0.1	0.08±0.05
NGC 5548_{93}	0.6	1.1 (1370)	$1.4^{+0.6}_{-0.4}$	1.4	0.8	1.1±0.7
NGC 5548_{89}	0.3	3.6 (1330)	$1.4^{+0.6}_{-0.4}$	1.4	0.8	1.2±0.6
Fairall 9	0.4	3.2 (1380)	$1.6^{+0.6}_{-0.4}$	4.0	1.0	1.4±0.7

7 gives similar predicted time delays to those of column 4 but includes the additional uncertainties in ε, D, f_ν, and $(\cos i)^{1/2}$ (see text below).

For the case where, for example, the disc temperature structure is solely determined by viscous dissipative forces it can be shown $\tau \propto (M\dot{M})^{1/3}\lambda^{4/3}$. Peterson et al. (1998) used a simple theoretical scaling method to estimate the UV/optical continuum lags for other objects. These authors assumed that the mass accretion rate was proportional to the UV luminosity, and that the virial mass of the sources could be estimated from the widths of the broad emission lines and the emission-line lag, see Collier et al. (1998). By estimating these quantities for individual sources and scaling the results relative to NGC 7469 they compute the expected UV/optical time lag, see their Table 9 and our Table 5.5.

For all objects we predict a smaller UV/optical time lag than those of Peterson et al. (1998). Given the simplicity and large uncertainties in the theoretical scaling method this is not all together surprising. We remark that by estimating the virial mass from mean spectra, one can over-estimate the mass by $\sim$ 30–40%, thus leading to a larger predicted time delay, §3.4.2.

For each AGN, our predicted UV/optical time delays are based on the monitoring campaign. That is the predicted delays are those expected during the actual campaign. Obviously, the time delay magnitude is a function of the adopted inclination and Hubble constant. Furthermore, the value of ε (eqn. 5.6 & Table 5.5) is biased by the stellar contribution. This contribution is least at UV wavelengths, and for the case of NGC 7469 was shown to be negligible at $\sim$ 1300Å (Welsh et al. (1998)). In the absence of an estimate for the stellar light contribution at the adopted UV wavelength for the other galaxies, we assume that the stellar light contribution must be less than the observed faint state flux, i.e. in the range $(0, < f_\nu^{\rm F})$. This implies that ε must be less than observed, as detailed in column 2 of Table 5.5, and can be between 0 and the observed value.

The error estimates on column 4, Table 5.5, are those induced by the uncertainty in the spectral slope α alone. To estimate the uncertainty in the relative time delays induced by the uncertainty in ε, we predicted relative time delays for the permitted range in ε, i.e. $0 \rightarrow \varepsilon$, and added the derived uncertainty in quadrature to the uncertainties in $\Delta\tau$ induced by the 20%, 10%, 12%, and $\sim$ 40% estimated uncertainties in D, Δf_ν, $(\cos i)^{1/2}$, and α respectively. This procedure gives the predicted relative time delays and error estimates for column 7 in Table 5.5.

As the luminosity state of the source varies, so do the predicted time delays as the effective size of the emission region grows. This will result in the difference spectrum flux, Δf_ν, increasing for similar continuum variation amplitudes, and lead to a corresponding change in the predicted time delays. For a factor P increase in Δf_ν, the relative time lag $\Delta\tau$ will increase by $\sqrt{P}$. For example, if Fairall 9 was observed 6 times brighter than in the 1994 campaign, $\Delta\tau_{1315-7000\mathring{A}} \sim 3.9$ days. Hence, higher luminosity sources will tend to have larger predicted time delays.

5.6 Conclusions

An analysis of AGN Watch monitoring data on 5 objects permits the following observations and conclusions.

1) It is critical to remove the effects of dust extinction and host galaxy contamination from the AGN spectra, before measuring the UV/optical slope. The contamination due to Fe II line + Balmer continuum must also be considered, and is likely to bias any UV slope determination. We note the methods of §5.5 for estimating the variable component accurately remove the host galaxy contamination provided the spectra were taken under similar observing conditions and with similar instrumental configurations. These methods afford improvement over other methods based on using normal galaxy template spectra, which only approximate the 'unknown' stellar distribution of the AGN.

2) Perhaps the primary uncertainty in an accurate determination of the UV/optical spectral index α ($f_\nu \propto \lambda^\alpha$) is the uncertain amount of extinction present. Furthermore, the measured α is strongly dependent on the wavelength regions used in its determination.

3) The UV spectral slope can differ significantly from the optical slope, by ~ 0.5.

4) There is good evidence that similar AGNs, i.e. Seyfert 1 nuclei, have an intrinsic variable nuclear flux distribution, $\alpha = -0.25 \pm 0.17$ ($f_\nu \propto \lambda^\alpha$). This intrinsic value of α indirectly implies the existence of classical accretion disc structures in Seyfert 1 galaxies, with $f_\nu \propto \lambda^{-1/3}$. The slope determinations for NGC 3783, NGC 7469, and Fairall 9 are consistent to within typical measurement uncertainties.

5) The existence of an intrinsic spectral slope for Seyfert 1 galaxies implies a common radial temperature profile relation, $T \propto R^{-b}$ with $b = 0.73 \pm 0.05$. This in turn allows us to predict a common wavelength-dependence for the time delays thought to be present in these systems, $\tau \propto \lambda^\gamma$ with $\gamma = 1.37^{+0.10}_{-0.09}$.

6) We predict continuum time delays of $\sim$ 0.5–2 light days between the flux variations at

1315Å and 7000Å, for similar Seyfert 1 galaxies.

Note: It has come to the attention of the author that presented results (i.e variable spectra estimates) pertaining to NGC 4151 are inaccurate. This inaccuracy does not effect the main conclusions of this chapter, and will be corrected when presented in journal format.

Chapter 6

Epilogue

6.1 Summary of Main Conclusions

Firstly, this thesis presented the results of an intensive two-month campaign of ground-based spectrophotometric monitoring of the Seyfert 1 galaxy NGC 7469, with a temporal resolution of $\leq$ 1 day. Secondly, it was shown how wavelength-dependent time delays test the standard paradigm of AGN, by tracing the temperature structure $T(R)$ of the gaseous material surrounding the purported black hole. Finally, a new direct method for measuring redshift-independent luminosity distances to AGN was presented. This method opens up a new route to H_0 and by extension to fainter objects at $z \sim 1$, q_0.

The main results of the thesis were summarized at the end of each chapter, but are re-stated below.

1. The Hα and Hβ emission lines (in NGC 7469) respond to 1315Å continuum variations with a time delay of $\sim$ 5-6 days. We consider this to be identification of variable Balmer line gas at a distance of $\sim$ 5-6 light days from the central source. This implies a compact Broad Line emitting Region in NGC 7469.

2. By combining the emission line lags and the widths of the variable component of the emission lines, we estimate the mass of the central source is $M \sim 10^{6-7} M_{\odot}$.

3. Significant wavelength-dependent time delays are detected in the continuum of NGC 7469. Variations at optical wavelengths lag behind those at 1315Å. Cross-correlation of the light curves shows the delay increases from $\sim$ 1 day at 4800Å to $\sim$ 2 days at 7500Å. We interpret this as evidence for a stratified continuum reprocessing region close to the central source, possibly that of an accretion disc. With this interpretation the delays are consistent with the predicted $\tau \propto (M\dot{M})^{1/3}\lambda^{4/3}$ relationship for a classical accretion disc (using the assumptions outlined in chapter 4) with temperature profile $T \propto R^{-3/4}$.

4. We find the agreement of the observed time delays and estimated nuclear spectral energy distribution with the respective $\tau \propto \lambda^{4/3}$ and $f_\nu \propto \lambda^{-1/3}$ predictions for a black-body accretion disc with $T \propto R^{-3/4}$ strong evidence for the existence of an accretion disc structure in NGC 7469.

5. We propose a new direct method for estimating redshift-independent luminosity distances to AGNs, and hence H_0. A first application of our method yields $H_0(\cos i/0.7)^{1/2} = 38 \pm 7\ \mathrm{km\,s^{-1}\,Mpc^{-1}}$. A major uncertainty in our method is the unknown nature and origin of the driving continuum variations, §4.5.5. Additional simultaneous multi-wavelength monitoring campaigns are required to address this fundamental issue.

For an Einstein-de Sitter Universe the Hubble constant estimate of $H_0 > 38\ \mathrm{km\,s^{-1}\,Mpc^{-1}}$ gives an age of the Universe t_0 of $< 17.2 \times 10^9$ years, c.f for $H_0 > 70\,\mathrm{km\,s^{-1}\,Mpc^{-1}}$, $t_0 < 9.3 \times 10^9$ years. Therefore, our Hubble constant estimate, at first sight, appears to be consistent with the age of the Universe as determined by other methods, §4.1.

6. We suggest that the intrinsic flux distribution of Seyfert 1 nuclei is described by $f_\nu \propto \lambda^{-0.25\pm0.17}$, and is consistent with the classical accretion disc prediction, $f_\nu \propto \lambda^{-1/3}$. This evidence suggests the existence of similar accretion disc structures in Seyfert 1 nuclei.

6.2 Future Outlook

There are numerous avenues of research that are suggested by this thesis. They are summarized as follows:

1. The Detection of Accretion-Disc Structures in AGN, and determination of H_0. By mapping the temperature profile $T(R)$ of the gaseous material surrounding the purported black hole, we will test the standard paradigm of AGN, and detect the signature of accretion disc structures in a variety of AGN. Simple minded simulation tests that generate a series of fake light curves with normalized fractional flux variations and a given time delay, indicate a 2 month campaign on a 1m telescope is sufficient to measure $H_0\sqrt{\cos i}$ with about 10% accuracy.

We have already initiated a number of optical multicolour broad-band monitoring campaigns designed to fulfil these aims; including two 6-week observing runs in South Africa, with the latter campaign supplemented by simultaneous observations from McDonald Observatory, Texas, USA, and the Wise Observatory, Israel. The results of these efforts will be known within 1-2 years. Ideally, simultaneous multi-wavelength observations, e.g. X-ray, UV, optical and IR, are required to investigate the nature of continuum variations at different wavelengths.

2. Determination of q_0-the deceleration parameter of the Universe. This goal will require sustained monitoring of higher redshift Seyferts and Quasars over a period of many months (and some luck). This will be the first comprehensive study of higher redshift Seyfert/Quasar variability on time-scales of about a week with temporal sampling of $\sim$ 1-2 observations per week, given expected UV/optical time delays of about a week, c.f 1-2 days for lower luminosity AGN. We note this may in fact be more readily achievable than the former goal of measuring H_0 through sustained continuous monitoring of local AGNs, that require higher temporal resolutions.

A feasibility study to ensure correct object selection will be undertaken. Considerations include the brightness of the object, type of AGN (careful selection of different AGN types will test unification scenarios of AGN), and field location/environment. Suitable targets will initially be selected at redshifts of about 1, where the curvature of space-time becomes important and the magnitude of the objects ($m \sim 18 - 20$ is easily accessible to medium-sized, i.e. 2-4m, telescopes. A moderately intensive observing season of multi-wavelength , preferably X-ray-IR, observations will complement the aforementioned monitoring efforts and measure the change in the Universe's expansion rate with cosmic epoch.

The procedure to measure q_0 will correct the observable quantities to the rest frame of the AGN, e.g take account of time dilation and apparent reddening of fluxes caused by the cosmological expansion of the Universe, and proceed to fit observed fluxes to predicted fluxes with a linear regression technique to recover the cosmological parameters, H_0 and q_0.

3. Irradiated Accretion Disc Models. Detailed irradiated accretion disc models will be further developed and fitted to the observational data. This could include running a series of complex irradiated disc atmosphere codes that treat the vertical structure of the disc self-consistently. The aim is to develop a detailed understanding of how the physical parameters of the system, e.g mass, accretion rate, and source luminosity, reproduce the data.

The work will considerably expand the work of Chapter 4, to include; A detailed exploration of the parameter space, and its implications for the temperature structure $T(R)$ of the accretion disc, wavelength-dependent continuum time delays, predicted spectral energy distributions, and disc structure. Further, by making reasonable assumptions about the nature of the continuum variations, measurement errors and data sampling characteristics, more complete simulation tests will be used to explicitly show the accuracy with which

$T(R)$, H_0, and q_0 can be measured from a given dataset. The results of this work will constrain the accretion disc models consistent with the available observations, give insight into the evolution of AGN, and present the observability of the wavelength-dependent time delays in more detail.

The Spectral Energy Distribution (SED) of AGN

There remains the need for an accurate, homogeneous investigation into the intrinsic, i.e. nuclear spectrum, of a variety of AGN. This study could make use of the two-dimensional multi-fibre spectrographs to obtain simultaneous multiwaveband observations of a large sample of AGN, and could be disguised as a long-term variability campaign with moderate temporal resolution. By careful examination and subsequent allowance for a host of continuum-altering effects, see §5.2, an accurate estimate for the intrinsic SED of AGN can be attained. This would enhance our understanding of the continuum emitting regions of AGNs, give valuable insight into the different physical processes at work in different AGNs, and provide information concerning the unification of AGN.

Virial Mass Estimates of a Sample of AGN

In principle, this project is fairly straightforward. Complete a systematic study of the available variability datasets to estimate the virial mass of the central source, using the method detailed in §3.4.2. This is, however, likely to be done imminently by a number of authors.

REFERENCES

Alexander T. in Astronomical Time Series, p. 163, Dortdrecht: Kluwer, 1997

Alloin D. et al., 1995, Astr. Astrophys., 293, 293

Antonucci R., 1982, Publs. astr. Soc. Pacif., 94, 561

Antonucci R., 1984, Astrophys. J., 278, 499

Antonucci R., 1985, Astrophys. J., 297, 621

Antonucci R., 1993, Ann. Rev. Astr. Astrophys., 31, 473

Arnaud K. A. et al., 1985, Mon. Not. R. astr. Soc., 217, 105

Bahcall J. N. et al., 1972, Astrophys. J., 171, 467

Baldwin J., 1977, Astrophys. J., 214, ???

Baldwin J., 1995, Astrophys. J., 455, 119

Baribaud T. et al., 1992, Astr. Astrophys., 256, 375

Barth A. J. et al., 1998, Astrophys. J., 496, 133

Barthel P. et al., 1989, Astrophys. J., 336, 606

Barvainis R., 1987, Astrophys. J., 320, 537

Barvainis R., 1993, Astrophys. J., 412, 513

Blandford R. D., McKee C. F., 1982, Astrophys. J., 255, 419

Blandford R. D. Saas-Fee Advanced Course 20, Active Galactic Nuclei, p. 161, Springer-Verlag, 1990

Bonatto C. J., Pastoriza M. G., 1990, Astrophys. J., 353, 445

Boyle B. et al., 1998, Mon. Not. R. astr. Soc., 296, 1

Branduardi-Raymont G. et al., 1985, Mon. Not. R. astr. Soc., 216, 1043

Burstein D., Heiles C., 1982, Astr. J., 87, 1165

Carleton N. P. et al., 1987, Astrophys. J., 318, 595

Cassidy I., Raine D. J., 1997, Astr. Astrophys., 322, 400

Choloniewski J., 1981, Acta.Astron., 31, 293

Clavel J. et al., 1989, Astrophys. J., 337, 236

Clavel J. et al., 1991, Astrophys. J., 366, 64

Clavel J. et al., 1992, Astrophys. J., 393, 113

Collier S. et al., 1998, Astrophys. J., 500, 162

Collin-Souffrin S. et al., 1982, Astr. Astrophys., 106, 362

Collin-Souffrin S. et al., 1988, Mon. Not. R. astr. Soc., 232, 539

Collin-Souffrin. Variability of Stars and Galaxies : Proc. of a conference, Leige, Institut d' Astrophysique, 1980

Collin-Souffrin S., 1991, Astr. Astrophys., 249, 344

Corbett E. A. et al., 1996, Mon. Not. R. astr. Soc., 281, 737

Crenshaw D. W. et al., 1996, Astrophys. J., 470, 322

Davidson K., Netzer H., 1979, Rev. Mod. Phys., 51, 715

de Vaucouleurs G., 1993, Astrophys. J., 415, 10

Dibai E. A., 1981, Soviet Astron., 28, 245

Dietrich M. et al., 1993, Astrophys. J., 408, 416

Dietrich M. et al., 1998, Astrophys. J. Suppl., 115, 185

Done C., Krolik J., 1996, Astrophys. J., 463, 144

Edelson R., Krolik J., 1988, Astrophys. J., 333, 646

Edelson R., Malkan M., 1986, Astrophys. J., 308, 59

Edelson R. et al., 1996, Astrophys. J., 470, 364

Elvis M. et al., 1989, Astr. J., 97, 777

Elvis M. et al., 1994, Astrophys. J. Suppl., 95, 1

Eracleous M., Halpern J. P., 1994, Astrophys. J. Suppl., 90, 1

Faber S. et al., 1989, Astrophys. J. Suppl., 69, 763

Ferland G., Mushotzky R. F., 1982, Astrophys. J., 262, 564

Ferland G. et al., 1979, Astrophys. J., 232, 382

Ferland G. et al., 1990, Astrophys. J., 363, L21

Ferland G. et al., 1992, Astrophys. J., 387, 95

Ferland G., 1985, Astrophys. J., 289, 105

Ferland G., 1991, OSU Internal Report (91-01)

Ferland G., 1993, University of Kentucky Department of Physics and Astronomy Internal Report

Ford H. C. et al., 1994, Astrophys. J., 435, L27

Francis P. J. et al., 1991, Astrophys. J., 373, 465

Freedman W. et al., 1994, Nature, 371, 757

Freedman W. et al. The Extragalactic Distance Scale, CUP, 1997

Gaskell C M., Peterson B. M., 1987, Astrophys. J. Suppl., 65, 1

Gaskell C. M., Sparke L., 1986, Astrophys. J., 305, 175

Genzel R. et al., 1995, Astrophys. J., 444, 129

George I. M., Fabian A. C., 1991, Mon. Not. R. astr. Soc., 249, 352

Glass I., 1979, Mon. Not. R. astr. Soc., 186, 29

Glass I., 1992, Mon. Not. R. astr. Soc., 256, 23

Goad M., Koratkar A., 1998, Astrophys. J., 495, 718

Goad M., Wanders I., 1996, Astrophys. J., 469, 113

Goad M. et al., 1993, Mon. Not. R. astr. Soc., 263, 149

Goad M. et al., 1994, Mon. Not. R. astr. Soc., 268, 845

Goad M. et al., 1995, Mon. Not. R. astr. Soc., 275, 1125

Goad M., 1995, in Ph.D Thesis, , 1

Gondhalekar P. M. et al., 1994, Mon. Not. R. astr. Soc., 268, 973

Green P. et al., 1992, Mon. Not. R. astr. Soc., 254, 30

Guilbert P. W., Rees M. J., 1988, Mon. Not. R. astr. Soc., 233, 475

Haardt F., Maraschi L., 1993, Astrophys. J., 413, 507

Heckman T. M., 1980, Astr. Astrophys., 87, 152

Hes R. et al., 1993, Nature, 362, 326

Ho L. in 32nd COSPAR meeting, the AGN-galaxy connection (advances in Space Science), 1998

Horne K. et al., 1991, Astrophys. J., 367, L5

Horne K. in Reverberation Mapping of the Broad-Line Region in Active Galactic Nuclei, p. 23, ASP, 1994

Hubeny I. et al., 1997, Astrophys. J. Letts., 484, L37

Kartje J. F., 1995, Astrophys. J., 452, 565

Kaspi S. et al., 1995, Wise Obs. Tech. Rep. 6

Kaspi S. et al., 1996a, Astrophys. J., 470, 336

Kaspi S. et al., 1996b, Astrophys. J. Letts., 471, 75

Kinney A. et al., 1985, Astrophys. J., 291, 128

Kinney A. et al., 1990, Astrophys. J., 357, 338

Kinney A. et al., 1991, Astrophys. J., 377, 100

Koratkar A., Gaskell C. M., 1991, Astrophys. J., 370, L61

Koratkar A., 1991, Astrophys. J. Suppl., 75, 719

Korista K. et al., 1995, Astrophys. J. Suppl., 97, 285

Korista K. et al., 1998, astro-ph/9805338, , 1

Kriss G. et al., 1998, Astrophys. J., in prep.

Krolik J. et al., 1991, Astrophys. J., 371, 541

Krolik J. in Reverberation Mapping of the Broad-Line Region in Active Galactic Nuclei, p. 53, ASP, 1994

Kundic T. et al., 1997, Astrophys. J., 482, 75

Kwan J., Krolik J., 1981, Astrophys. J., 250, 478

Laor A., Netzer H., 1989, Mon. Not. R. astr. Soc., 238, 897

Laor A., 1998, Astrophys. J. Letts., in press

Lawrence A., Elvis M., 1982, Astrophys. J., 256, 410

Lawrence A., Papadakis I., 1993, Astrophys. J., 414, 85

Leighly K. et al., 1997, Astrophys. J., 483, 767

Lightman A. P., White T. R., 1988, Astrophys. J., 335, 57

Lockman F. J., Savage B. D., 1995, Astrophys. J. Suppl., 97, 1

Lynden-Bell D. et al., 1969, Nature, 223, 690

Mackay C. D. et al., 1986, Ann. Rev. Astr. Astrophys., 24, 255

Malkan M., Filippenko A., 1983, Astrophys. J., 275, 477

Malkan M. A., Sargent W. L., 1982, Astrophys. J., 254, 22

Malkan M. in Proc. Garching Conf. on UV and X-ray Emission from AGN, p. 121, Garching (ESO), 1984

Maoz D., Netzer H., 1989, Mon. Not. R. astr. Soc., 236, 21

Maoz D. et al., 1990, Astrophys. J., 351, 75

Maoz D. et al., 1991, Astrophys. J., 367, 493

Maoz D. et al., 1993, Astrophys. J., 404, 576

Marshall H. L. et al., 1997, Astrophys. J., 479, 222

Mathis J. S., 1990, Ann. Rev. Astr. Astrophys., 28, 37

Matthew T. A., Sandage A. R., 1963, Astrophys. J., 138, 30

McHardy I. M. et al., 1990, Mon. Not. R. astr. Soc., 242, 215

Miyoshi M. et al., 1995, Nature, 373, 127

Mushotzky R. F. et al., 1980, Astrophys. J., 235, 377

Mushotzky R. F. et al., 1993, Ann. Rev. Astr. Astrophys., 31, 717

Nandra K. et al., 1991, Mon. Not. R. astr. Soc., 248, 760

Nandra K. et al., 1998, Astrophys. J., in press

Netzer H., Ferland G. L., 1984, Publs. astr. Soc. Pacif., 96, 593

Netzer H., Maoz D., 1990, Astrophys. J. Letts., 365, L5

Netzer H., Peterson B. M. in Astronomical Time Series, p. 230, Dortdrecht: Kluwer, 1997

Netzer H., 1980, Astrophys. J., 236, 406

Netzer H. Saas-Fee Advanced Course 20, Active Galactic Nuclei, p. 57, Springer-Verlag, 1990

Neugebauer G. et al., 1987, Astrophys. J. Suppl., 63, 615

Neugerbauer G. et al., 1979, Astrophys. J., 230, 79

O'Brien P. et al., 1988, Mon. Not. R. astr. Soc., 233, 801

O'Brien P. et al., 1994, Mon. Not. R. astr. Soc., 268, 485

O'Brien P. et al., 1998, Astrophys. J. Suppl., in press

Osterbrock D. Astrophysics of Gaseous Nebulae and Active Galactic Nuclei, p. 1, University Science Books, 1989

Osterbrock D. E., 1991, Phys.Rev., 54, 579

Penston M. V., Pérez E., 1984, Mon. Not. R. astr. Soc., 211, 33

Penston M. V. et al., 1971, Publs. astr. Soc. Pacif., 83, 783

Penston M., 1990, Mon. Not. R. astr. Soc., 244, 357

Pérez E. et al., 1992, Mon. Not. R. astr. Soc., 255, 502

Perola G. et al., 1986, Astrophys. J., 306, 508

Peterson B. M., Collins G. W., 1983, Astrophys. J., 270, 71

Peterson B. M. et al., 1985, Astrophys. J., 298, 283

Peterson B. M. et al., 1988, Publs. astr. Soc. Pacif., 110, 660

Peterson B. M. et al., 1991, Astrophys. J., 368, 119

Peterson B. M. et al., 1992, Astrophys. J., 392, 470

Peterson B. M. et al., 1993, Astrophys. J., 402, 469

Peterson B. M. et al., 1994, Astrophys. J., 425, 622

Peterson B. M. et al., 1995, Publs. astr. Soc. Pacif., 107, 579

Peterson B. M. et al., 1998, Publs. astr. Soc. Pacif., 110, 660

Peterson B. M., 1993, Publs. astr. Soc. Pacif., 105, 247

Peterson B. M. in Reverberation Mapping of the Broad-Line Region in Active Galactic Nuclei, p. 1, ASP, 1994

Peterson B. M. An Introduction to Active Galactic Nuclei, p. 237, CUP, 1997

Pijpers F. P. in Reverberation Mapping of the Broad-Line Region in Active Galactic Nuclei, p. 69, ASP, 1994

Pounds K. A. et al., 1990, Nature, 344, 132

Pounds K. A., 1990, Mon. Not. R. astr. Soc., 242, 1

Press W., Flannery B., Teukolsky S., Vetterling W. Numerical Recipes, Cambidge University Press, Cambridge, 1992

Puetter R. C., 1987, Mon. Not. R. astr. Soc., 260, 77

Rees M. J., 1984, Ann. Rev. Astr. Astrophys., 22, 471

Rees M., 1989, Mon. Not. R. astr. Soc., 239, 1

Refsdael S., 1964, Mon. Not. R. astr. Soc., 128, 295

Reichert G. et al., 1994, Astrophys. J., 425, 582

Robinson A., Pérez E., 1990, Mon. Not. R. astr. Soc., 244, 138

Robinson A. in Reverberation Mapping of the Broad-Line Region in Active Galactic Nuclei, p. 147, ASP, 1994

Robson I. in Active Galactic Nuclei, p. 1, Wiley Praxis, 1995

Rodriguez-Pascual P. M. et al., 1997, Astrophys. J. Suppl., 110, 9

Rokaki E. et al., 1992, Astr. Astrophys., 261, 41

Rokaki E. et al., 1993, Astr. Astrophys., 272, 8

Romanishin W. et al., 1995, Astrophys. J., 455, 516

Rowan-Robinson M. M., 1988, Space Sci. Rev., 48, 1

Salamanca I. et al., 1995, Astr. Astrophys. Suppl., 111, 283

Salpeter E. E., 1964, Astrophys. J., 140, 796

Sanbuichi K. et al., 1993, P.A.S.J., 45, 443

Sandage A. et al., 1996, Astrophys. J., 460, L15

Santos-Lleó M. et al., 1997, Astrophys. J. Suppl., 112, 271

Schmidt M., 1963, Nature, 197, 1040

Seaton M. J., 1979, Mon. Not. R. astr. Soc., 187, 75

Seyfert C., 1943, Astrophys. J., 97, 28

Shakura N. I., Sunyaev R. A., 1973, Astr. Astrophys., 254, 22

Shields G. A., 1978, Nature, 272, 706

Sincell M., Krolik J., 1997, Astrophys. J., 476, 605

Sparke L. S., 1993, Astrophys. J., 404, 570

Stark A. A. et al., 1992, Astrophys. J. Suppl., 79, 77

Stirpe G. et al., 1994, Astrophys. J., 425, 609

Sun W.-H., Malkan M., 1989, Astrophys. J., 346, 68

Sunyaev R., Zel'dovich Y. B., 1980, Ann. Rev. Astr. Astrophys., 18, 537

Tanaka Y. et al., 1995, Nature, 375, 659

Tanvir N. et al., 1995, Nature, 377, 27

Taylor J. A., 1996, Astrophys. J., 470, 269

Terlevich R. et al., 1994, Mon. Not. R. astr. Soc., 255, 713

Terrell J., 1967, Am.J.Phys., 45, 869

Tonry J., Schneider D., 1988, Astr. J., 96, 807

Tully R. B., Fisher J. R., 1977, Astr. Astrophys., 54, 661

Turner T. J., Pounds K. A., 1989, Mon. Not. R. astr. Soc., 240, 833

Ulrich M.-H., Horne K., 1996, Mon. Not. R. astr. Soc., 283, 748

Ulrich M.-H. et al., 1984, Mon. Not. R. astr. Soc., 206, 221

Ulrich M.-H. et al., 1991, Astrophys. J., 382, 483

Ulrich M.-H. et al., 1997, Ann. Rev. Astr. Astrophys., 35, 445

Unger S. et al., 1987, Mon. Not. R. astr. Soc., 228, 671

Urry C. M., Padovani P., 1995, Publs. astr. Soc. Pacif., 107, 803

van den Bergh S., 1992, Publs. astr. Soc. Pacif., 104, 861

van Groningen E., Wanders I., 1992, Publs. astr. Soc. Pacif., 104, 700

Wade R., Horne K., 1988, Astrophys. J., 324, 441

Wamsteker W. et al., 1990, Astrophys. J., 354, 446

Wanders I., Horne K., 1994, Astr. Astrophys., 289, 76

Wanders I. et al., 1992, Astr. Astrophys., 266, 72

Wanders I. et al., 1995, Astrophys. J., 453, L87

Wanders I. et al., 1997, Astrophys. J. Suppl., 113, 69

Wanders I., 1995, Astr. Astrophys., 296, 332

Ward M. J. et al., 1978, Astrophys. J., 223, 788

Warwick R. S. et al., 1996, Astrophys. J., 470, 349

Welsh W., Horne K., 1991, Astrophys. J., 379, 586

Welsh W. et al., 1998, Astrophys. J., in press

Westin B. A., 1985, Astr. Astrophys., 151, 137

White R. J., Peterson B. M., 1994, Publs. astr. Soc. Pacif., 106, 879

Wilkes B. J. et al., 1987, Astrophys. J., 323, 243

Wills B. et al., 1985, Astrophys. J., 288, 94

Wilson A., Colbert E. J., 1995, Astrophys. J., 438, 62

Wilson A. S. et al., 1991, Astrophys. J., 381, 79

Wilson A. S. in Emission Lines in Active Galaxies: New Methods and Techniques IAU Colloquium 159, p. 264, ASP, 1996

Winge C. et al., 1995, Astrophys. J., 445, 680

Winget D. E., 1987, Astrophys. J., 315, 77

Winkler H. et al., 1992, Mon. Not. R. astr. Soc., 257, 659

Winkler H. et al., 1997, Mon. Not. R. astr. Soc., 292, 273

Young S. et al., 1998, Mon. Not. R. astr. Soc., 294, 478

Zel'dovich Ya. B., Novikov I. D., 1964, Sov.Phys.Dokl, 158, 811